Modelling the morphodynamics of tidal channels

Gianluca Vignoli

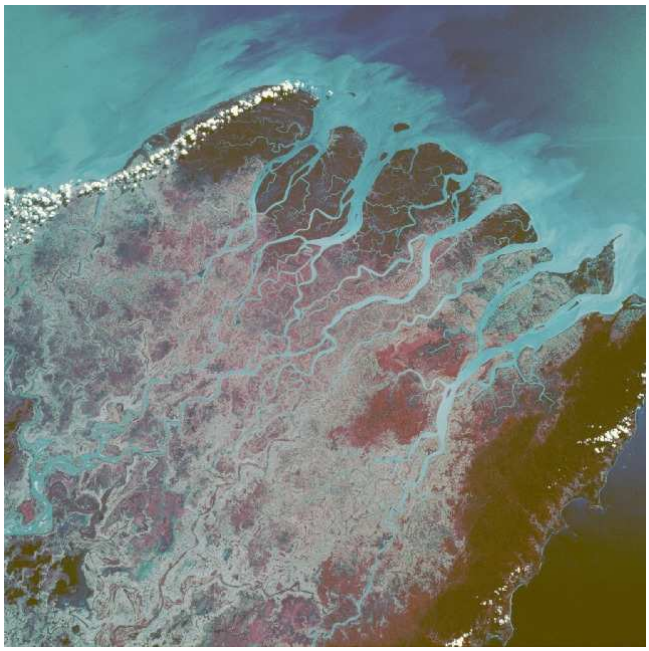

UNIVERSITÀ DEGLI STUDI DI TRENTO

2004

Doctoral thesis in **Environmental Engineering** (XV cycle)
Faculty of Engineering, **University of Trento**
Year: **2004**
Supervisor: **Prof. Marco Tubino**
Cotutor: **Guido Zolezzi**

Università degli Studi di Trento
Trento, Italy
2004

What is now proved was once only imagin’d

William Blake - The Marriage of Heaven and Hell (1790-3)

Acknowledgements

The author wishes to thank Marco Tubino and Guido Zolezzi for their friendship and for the introduction in the complex world of scientific research.

The author is thankful to Marco Toffolon for his collaboration in the analysis of some topics of this thesis.

This work has been developed within the tidal research group of the Department of Civil and Environmental Engineering of Trento, which is composed by Marco Tubino, Marco Toffolon, Ilaria Todeschini and myself. Some results have been presented in preliminary form at international and national conferences: 3rd RCEM 2003-Barcelona, Spain; XXX IAHR 2003-Thessaloniki, Greece; RiverFlow 2002-Louvain-La-Neuve, Belgium; Idra2000, Genova and 28 Convegno Nazionale di Idraulica e Costruzioni Idrauliche-2003, Potenza.

Contents

List of Figures

List of Tables

List of symbols

Symbol			Eq.
a		dimensionless reference level for the concentration field	4.26c
a, b, d		coordinate of the trajectory foot	5.12a, 5.12b and 5.12c
a_0	$[L]$	tide amplitude	2.1
$\mathbf{A}$		matrix	5.19 and 5.21
A_n		normalized Fourier component	2.34
α		tide asymmetry	3.6
α		angle between the shear stress and the bed load vector	4.23a
α		ratio between local and turbulent effects	7.2
B	$[L]$	channel width	2.2
B^*	$[L]$	channel half width	4.1a
B_∞	$[L]$	asymptotic channels width	2.2
B_0	$[L]$	channel width at the mouth	2.2
β		aspect ratio	4.2a
c_0	$\left[LT^{-1}\right]$	frictionless celerity	2.15
c_x, c_y, c_z		Courant numbers	5.41
C		volumetric sediment concentration	4.3d
C_e		equilibrium sediment concentration near the bed	4.26a
C_f		friction factor	4.28
C_{f0}		reference friction factor	4.2c
C_h		dimensionless Chezy coefficient	2.4
C_0		analytical contribution to the concentration	5.34
$\overline{C_0}$		depth averaged concentration	7.9
C_1		numerical contribution to the suspension	5.32

Symbol			Eq.
C_1		perturbation of the concentration	7.12
CFL		Courant-Friedrichs-Levi number	2.8
γ		convergence parameter	2.20
γ		$\gamma = \beta\sqrt{C_{f0}}$	4.3a
D		dimensionless flow depth	4.1b
D_0	$[L]$	mean depth at the mouth	2.1
D_0^*	$[L]$	reference flow depth	4.1b
D_s		dimensionless grain size	4.2b
D_s^*	$[L]$	grain size	4.2b
δ		ratio between advection and settling effects	7.7
δ		weighting function	5.42
e_s		equivalent roughness	4.26c
$\mathbf{E}$		vector	5.25
ε		dimensionless tide amplitude	2.1
f		vertical concentration profile	5.35
F_0		Froude number	4.3a
ϕ		angle of repose of bed material	4.25
ϕ_0		vertical structure of the concentration	7.9
Φ_n^H		phase lag for the free surface elevation	2.9
Φ_n^U		phase lag for the flow velocity	2.10
g	$\left[LT^{-2}\right]$	gravity accelerations	2.3a
$\mathbf{G}$		vector	5.23 and 5.24
G_1, G_2		Rouse numbers	5.36a and 5.36b
η	$[L]$	bed elevation	3.1
η		dimensionless bed elevation	4.1b
h	$[L]$	free surface elevation	2.3a
h		dimensionless free surface elevation	4.1b
h_n	$[L]$	Fourier component of the free surface elevation	2.9
$\widehat{k}$		unit vector in the vertical direction	4.10
k_s	$\left[L^{\frac{1}{3}}T^{-1}\right]$	Gaukler-Strickler coefficient	
K_v		von Karman constant	
L_b	$[L]$	convergence length	2.2
L_b^*	$[L]$	dimensional wavelength	7.17
L_e	$[L]$	length of the estuary	2.12

Symbol			Eq.
L_g	$[L]$	frictionless wavelength	2.16
λ		dimensionless wave length	7.2
Λ	$\left[LT^{-1}\right]$	eigenvalues	2.7
i, j, k		numerical indexes	
i_f		mean bed slope	4.3a
j		flow dissipation	2.3a
n		direction normal to the bed load vector	4.24
$\widehat{n}$		unit vector normal to the bed	4.11
$\widehat{n_s}$		unit vector normal to the free surface	4.18
N		vertical structure for the eddy viscosity	4.8
ν_T		dimensionless eddy viscosity	4.3a
p		sediment porosity	3.1
P		vertical structure for the eddy diffusivity	4.9
p_1, p_2		forcing terms	7.16
Ψ_T		dimensionless eddy diffusivity	4.3d
Q	$\left[L^3T^{-1}\right]$	flow discharge	2.3a
Q_0		dimensionless parameter	4.12
Q_{bx}, Q_{by}		dimensionless bed load vector	4.29a
q_s	$\left[L^2T^{-1}\right]$	solid discharge	3.1
q_{s1}		perturbation of the suspended load	7.18
θ		dimensionless Shields stress	4.22, 3.3
θ'		effective Shields stress	4.27
θ_0		reference Shields stress	4.2c
θ_{cr}		critical value of Shields stress for vanishing bed slope	4.25
$\overline{\theta_{cr}}$		critical value of Shields stress	4.25
r		empirical coefficient	4.24
r'		empirical coefficient	4.25
r_t, r_x, r_y		coefficients for the coordinate transformation	5.4a, 5.4b and 5.4c
R_h	$[L]$	hydraulic radius	2.4
R_p		particle Reynolds number	4.2d
s		direction the bed load vector	4.25
t	$[T]$	time	2.3a
t		dimensionless time	4.1d
T		transport parameter	4.26b

Symbol			Eq.
T_0	$[T]$	tide period	2.11
T_0^*	$[T]$	reference time scale	4.1d
T_{bed}	$[T]$	time scale for bed evolution	3.5
T_b	$[T]$	time scale for bed evolution due to bed load	6.2
T_s	$[T]$	time scale for bed evolution due to suspended load	6.1
τ		dimensionless shear stress	5.1
τ^*	$\left[ML^{-1}T^{-2}\right]$	shear stress	4.7
u,v,w		dimensionless velocity	4.1c
u_*		dimensionless shear velocity	4.7
u_n	$\left[LT^{-1}\right]$	Fourier component of the flow velocity	2.10
U	$\left[LT^{-1}\right]$	flow velocity	2.4
$\mathbf{U}$		vector of the dimensionless x-component of the flow velocity	5.18
$\widetilde{U}$	$\left[LT^{-1}\right]$	local maximum velocity	2.32
U_0	$\left[LT^{-1}\right]$	velocity scale	2.21
U_0^*	$\left[LT^{-1}\right]$	reference velocity	4.1c
U_g	$\left[LT^{-1}\right]$	frictionless velocity scale	2.17
$\mathbf{V}$		vector of the dimensionless y-component of the flow velocity	5.18
ω	$\left[T^{-1}\right]$	tidal frequency	2.9
ω		ratio between advective and turbulent effects	7.2
Ω	$\left[L^2\right]$	cross sectional area	2.3a
$\widetilde{w}$		contravariant component of the vertical velocity	5.5
W_s		dimensionless particle settling velocity	4.30
x	$[L]$	longitudinal coordinate pointing landwards	2.2
x,y		plain dimensionless coordinate	4.1a
ξ		dimensionless vertical boundary fitted coordinate	4.4
χ		ratio between friction and inertia	2.19
z		vertical dimensionless coordinate	4.1b
z_0		dimensional reference level for the velocity profile	5.14
Z_0		Rouse number	7.2

Symbol		Eq.
ζ	logarithmic boundary fitted vertical coordinate	5.2

1 Introduction

An estuary is a water body located close to the sea, whose main distinctive feature is the occurrence of the tide. Following Perillo (1995) “an estuary is a semi-enclosed coastal body of water that extends to the effective limit of tidal influence, within which sea water entering from one or more free connections with the open sea, or any other saline coastal body of water, is significantly diluted with fresh water derived from land drainage, and can sustain euryhaline (i.e. able to tolerate a wide range of salinity) biological species from either part or the whole of their life cycle.”

Tides take place on a time scale of the order of magnitude of a day, which is relatively short with respect to the typical time scale of the morphodynamic behaviour of a tidal system. As an example typical patterns of tidal oscillation in the Venice lagoon are reported in figure 1.1. Two main phases occur: the flood phase, when the flow is directed from sea to land, and the ebb phase, when the flow goes in the opposite direction.

Many types of natural environments can be classified as tidal systems. Their shape and dynamics depend on many factors, like the amplitude of tidal oscillations, the presence of subsidence, the mean sea level rise, the typology of sediment. Figures 1.2 and 1.3 show two typical examples of tidal systems, a lagoon (the Venice lagoon) and a tide dominated estuary (the Western Scheldt).

A glance to these pictures suggests that tidal systems can be extremely different from one another. The classifications proposed recently by Seminara et al. (2001a) and by Perillo (1995) are mainly based on morphological criteria and on the amplitude of the tidal range, and consider most of the morphological features observed around the world in tidal systems, like lagoons, tide dominated estuaries, delta estuaries and tidal rivers.

In simple descriptive terms *tide dominated estuaries* are those in which tidal currents play the dominant role, while density driven circulations are nearly absent because strong tidal effects are able to destroy vertical stratification. Tide dominated estuaries are usually funnel-shaped and characterised by the presence of sand waves, intertidal flats and salt marshes (see figure 1.3). The periodic tidal currents can store large volumes of water in the estuary at high tides, which are followed by drainage at low tides. The total volume of water exchanged during the tidal cycle is known as the tidal prism. In tide-dominated estuaries the tidal prism is at least an order of magnitude greater than the volume of water discharged by the river daily (Harris et al., 1993).

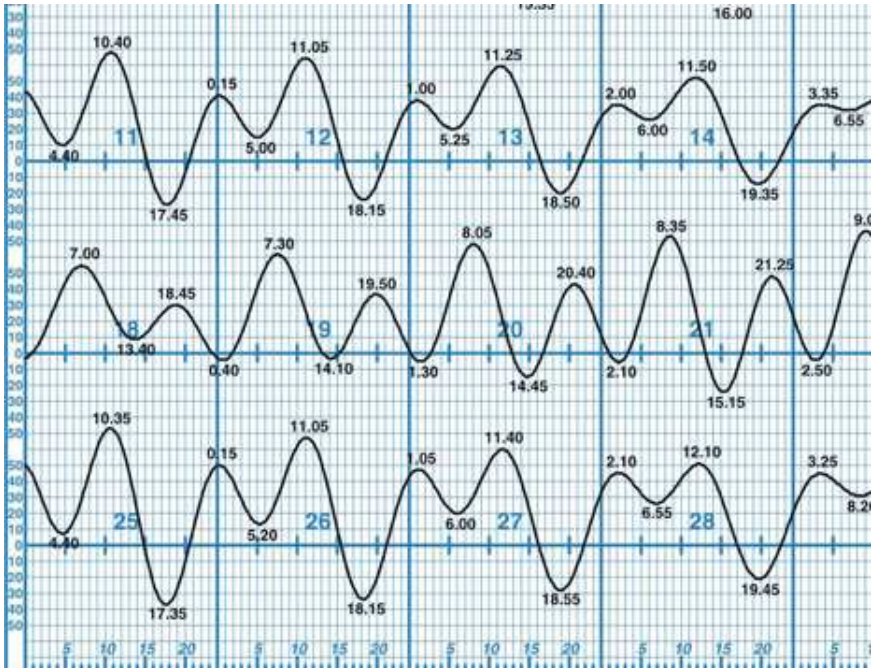

Figure 1.1: Tide oscillations in Venice lagoon.
(Comune di Venezia <http://www.comune.venezia.it/maree/astro.asp>)

Coastal lagoons are inland water bodies connected to the sea by one or more restricted inlets from which a complex network of tidal channels may originate.

Delta estuaries are shoreline protuberances, formed where river supplied sediments have accumulated in standing bodies of water faster than it can be redistributed by basinal processes such waves, currents, tides or submarine failures (Write, 1985).

Tidal rivers are those systems that are affected by tidal actions but salt intrusion may be limited to the mouth or it is totally absent. Normally these estuaries are associated to large river discharge.

Despite this high variability, for the purpose of the present work it is important to focus on the recurring elements of natural tidal systems.

Besides the forcing effect due to tide oscillations, another relevant and common characteristic of such systems is that sediments are typically very fine; an example is given in figure 1.4 where the grain size distribution of the Western Scheldt is reported.

Sediments can be transported as wash load, suspended and bed load. The first mechanism involves only the finest fraction (clay particles): the vertical concentrations profiles of wash load are fairly homogeneous. Suspension occurs as the result of two counteracting mechanisms, namely the ability of turbulence to raise sediment grains and their tendency to settle due to gravity. Grains smaller than 0.15mm can be entrained into suspension as soon as they begin to move, while larger

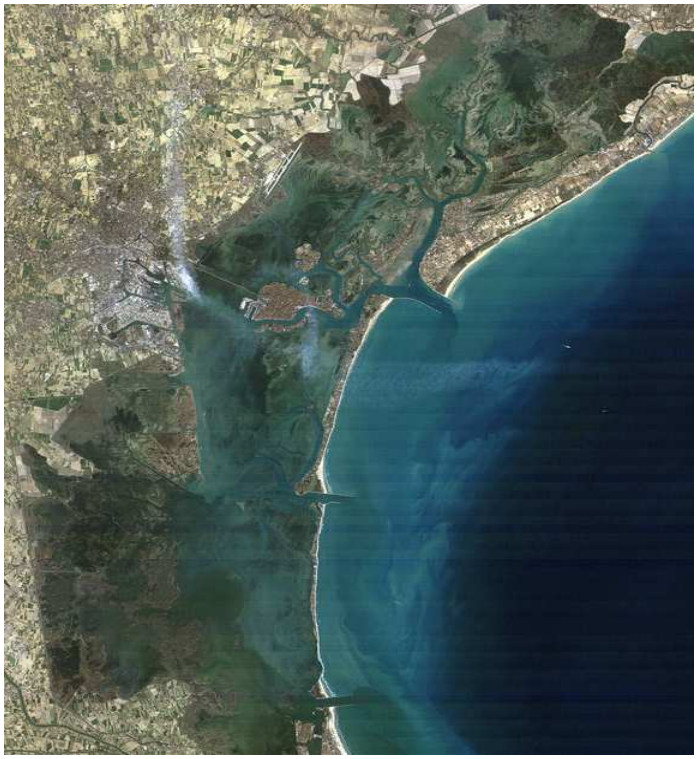

Figure 1.2: The Venice lagoon. (Consorzio Venezia nuova <http://www.salve.it>)

Figure 1.3: The Western Scheldt. (Image downloaded from the internet)

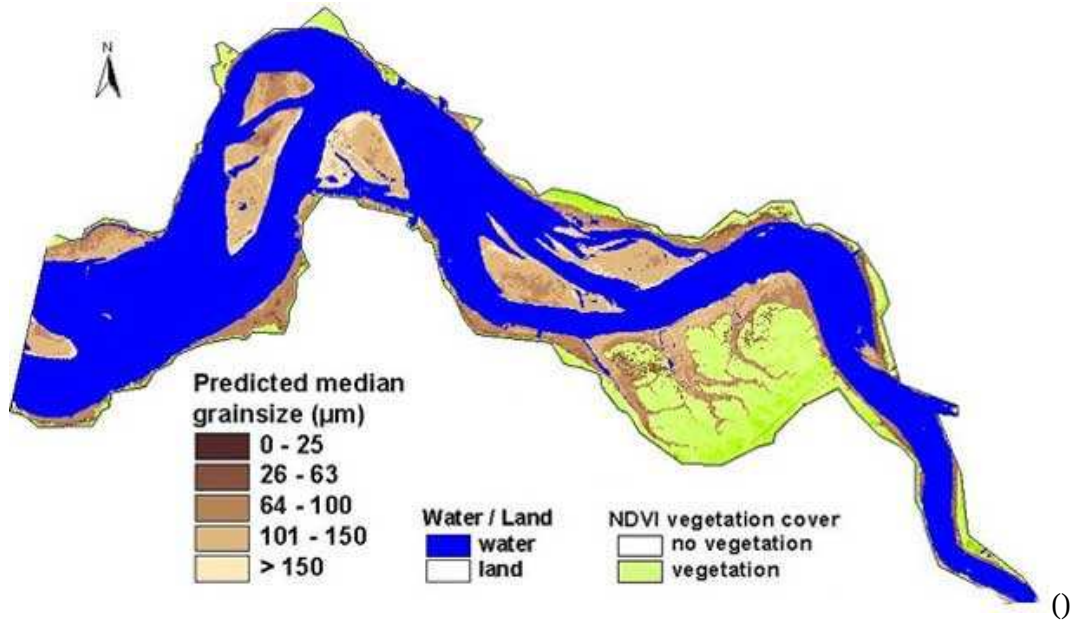

Figure 1.4: Sediment grain size distribution in the Western Scheldt. (Image downloaded from the internet)

grains move dominantly as bed-load at low values of flow velocity and then go into suspension when velocity attains higher values during the tidal cycle.

The dynamics of a tidal channel is a complex phenomenon that reveals the presence of several spatial and temporal scales. The spatial scales in tidal systems may range between the embayment length and the flow depth and can be defined according to the classification introduced by de Vriend et al. (2000):

micro-scale (or small-scale): the level of the smallest morphological phenomena associated with water and sediment motion (ripple and dune formation);

meso-scale: the level of the main morphological features (depositional bars, channels and shoals);

macro-scale: the level at which the meso-scale features interact;

mega-scale: the level at which the principal elements of the entire system interact (i.e. the estuary considered as a whole water body).

It is worth noticing that observed bed-forms in tidal systems may range from centimeter-size, *current ripples*, through decimeter-meter-size, *dunes*, and meter-size, $bar - forms$ (see Dalrymple and Rhodes, 1995).

The time scale of bed evolution T_b is in general independent of the tidal period T_0 and is mainly related to flow and sediment characteristics. Depending upon the spatial scale under investigation, the suitable time scale of bed development may range from 10^2 to 10^6 tidal periods ($\approx month - century$). The lower limit corresponds to the behaviour of meso-scale bedforms (bars) in small channels, while the upper limit corresponds to mega-scale phenomena. Moreover the time scale associated to the formation of ripples and dunes is comparable to the tidal period.

Another common element, which is relevant for the present work, is that many tidal systems are frictionally dominated, which means that the role of inertia is much smaller compared to that played by friction.

The classification of Perillo (1995) points out that the morphological characteristics are influenced by the interaction of channels with shoals and intertidal zones, like tidal flats and salt marshes. An intertidal flat is a deposit emerging during low tide and submerged during high tide, while salt marshes are environments in the intertidal zone where a muddy substrate can support a varied and normally dense stand of halophytic plants (Reineck, 1972; Allen and Pye, 1992).

The morphodynamics of tidal systems is still not completely understood, though many contributions have been recently proposed to investigate their behaviour (Friedrichs and Aubrey, 1994; Lanzoni and Seminara, 1998; Schuttelaars and de Swart, 1999; Schuttelaars and de Swart, 2000; Lanzoni and Seminara, 2002). Due to the fact that fluvial systems have been more deeply investigated in the past decades, many authors have tried an extension of river theories to tidal contexts (Seminara and Tubino, 2001; Solari et al., 2002).

The relevance of understanding the morphological behaviour of tidal channels lies in the fact that such systems may have a strong impact on human activities, like in the case of the city of Bruges, formerly an important commercial harbour, which lost its commercial role during the 15^{th} century when the tidal channel which joined the city to the sea was filled with sediments. Also note that several important harbours in Europe are located on tide-dominated estuaries (Antwerp, Hamburg, Bordeaux, London).

The present study investigates the morphological behaviour of tidal channels, like tide-dominated estuaries and channels in coastal lagoons, through different models that reflect the morphodynamics at the relevant spatial and temporal scales.

We first focus the attention on the mega-scale morphodynamic behaviour of tidal channels. The main aim is to determine an equilibrium configuration of the bed profile as a function of geometrical parameters (channel depth, width, degree of convergence, etc.) and hydrodynamic parameters (tidal excursion, friction factor). Note that the existence of equilibrium configurations in morphodynamical systems is a delicate concept, that has been widely discussed in the literature (e.g. Seminara, 1998).

Then we move our attention to the meso-scale morphodynamic behaviour of tidal channels,

with the specific aim of investigating the development process of bar-forms, which are prominent morphological features within most estuaries. Due to their large size relative to channel width, these bedforms have an important role on the dynamics of an estuary and strongly affect its use for human activity. The study of the formation of depositional bars is a key ingredient for the comprehension of the morphodynamics of both river and tidal systems, as pointed out by many authors (e.g. de Vriend et al., 2000, Tubino and Seminara, 1990), since the behaviour of such systems is mainly determined by the non-linear interaction of free- and forced-bars, the forcing effects being essentially related to the presence of channel curvature and width variations. Understanding the mechanism of formation and migration of bars and their response to forcing effects is then the preliminar requirement for the development of models able to predict the evolution of tidal channels.

The problem of the development of bedforms in fine sediment systems (like tidal channels) has been studied in the past by many authors, namely in the case of small scale bedforms (i.e. dunes) both in fluvial and tidal contexts; for example, Southard and Boguchwal (1990) provide an extensive set of observations in laboratory flumes, while Dalrymple et al. (1978) and Rubin and McCulloch (1980) propose a classification based on field observations. Dune size, shape, orientation and migration speed have been studied by several authors (Allen, 1968, 1982; Nordin, 1971; Yalin, 1964, 1977, 1987; Rubin and Hunter, 1987; Rubin and Ikeda, 1990; van Den Berg, 1987). Dunes are very often superimposed over large scale bedforms and induce significant dissipative effects on the flow.

On the contrary, the mechanism of bars formation in fine sediment systems is not widely understood as for dunes. Referring to the fluvial case, indeed, their development process has been investigated only recently in sandy rivers (Tubino et al., 1999; Watanabe and Tubino, 1992). While the main results are discussed in detail in Chapter 6, it is sufficient to recall here that when sediment transport mainly occurs as suspended load, several distinctive features arise with respect to gravel bed rivers. In the latter case, which has been widely investigated in the last thirty years (see for example Colombini et al., 1987), free bars exhibit a wavelength nearly equal to $6-7$ times the width of the channel. In the case of the Adige river near Trento, Italy (the closest example to the place where the present study has been carried out), whose averaged width is $80\,m$, a bar length of nearly $500\,m$ is predicted. When suspended load is dominant, theoretical predictions of free bar wavelength may increase up to $50-60$ channel widths. This implies that in lower river reaches, where fine sediments are observed, and the width may be of the order of few hundreds of meters (e.g. the lower reach of Po river, the largest river in Italy), the predicted wavelength of free bars would range up to $25-30\,km$! This poses a severe limitation to field observations. A recent analysis of Federici and Seminara (2003a) indeed shows that, for the development of a regular train of migrating free bars, the channel should be straight for a length of the order

of several bar wavelengths. Hence, in order to observe at least some free bar wavelengths, in the case of gravel bed rivers the channel must keep approximately straight for few kilometres, as may occur in artificially straightened channels and also in natural rivers; on the contrary fine sediment channels should keep straight for tens of kilometres, a condition which can be hardly met in natural rivers. We also note that while many contributions are now available to understand the formation of “point” forced bars in curved fluvial channels under bed load dominated conditions (for example Ikeda et al., 1981, Tubino and Seminara, 1990, Seminara et al., 2001b), only few of them consider the effect of suspended sediment transport and its crucial implications in the planimetric development of meandering channels.

Tidal bar-forms display a shape similar to that of fluvial bars, with oblique and longitudinally oriented depositional fronts. Several field observations, like those on the Salmon River estuary, the Bay of Fundy (Dalrymple and Rhodes, 1995) and along the tidal creeks of South Carolina (Barwis, 1978), suggest that the bar length ranges around 6 times the channel width, a similar scaling of the river case. Dalrymple and Rhodes (1995) assert that flow reversal does not alter the process of bar formation (like in the case of dunes) and propose a distinction between "repetitive bar-forms", which are very similar to fluvial bars, and "elongate tidal bars", which display more complex structures and are observed, for example, along the Thames (Robinson, 1960) and in the Bay of Fundy (Knight, 1980; Dalrymple et al., 1990).

As stated in the review of Dalrymple and Rhodes (1995) the dynamics of estuarine bar-forms is still more poorly understood than their fluvial counterparts. It is worth noticing that in an estuary only a part of the tidal cycle contributes to the morphodynamic behaviour of the channel, because close to the flow reversal the shear stress falls below the threshold value for sediments transport. The hydrodynamics of fluvial systems is characterised by negligible values of local flow accelerations, as occur in tidal channels when the flow velocity attains its maximum value. In these conditions, corresponding to the peak of sediment transport, local values of flow acceleration are negligible. When the flow velocity is close to zero, settling dominates over turbulence. Differences with respect to the river case dramatically increase at the flow reversal, since flow accelerations are strong: in these cases the vertical distribution of longitudinal velocity often exhibits a peculiar structure, displaying opposite directions at the free surface, where inertia effects are larger, and near the bed, where inertia vanishes (see figure 1.5). In the last two decades mathematical approaches, mostly based on perturbative methods, have been successfully applied to the study of the dynamics of free and forced-bar in fluvial systems and the planimetric evolution of river channels. Such approaches have been recently extended to tidal systems by Seminara and Tubino (2001), Solari et al. (2002) and Toffolon (2002).

The above theories mostly refer to the case of frictionally dominated tidal channels with constant width and follow a so-called "local" approach, whereby a reach length of the order of few

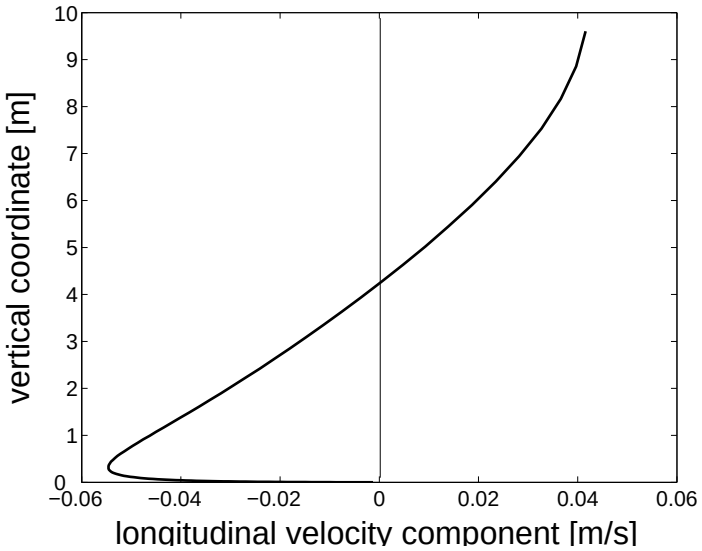

Figure 1.5: Vertical velocity profile during the flow reversal.

channel widths is considered. This implies that the tide can be reproduced as a sequence of locally uniform flows, with a nearly constant flow depth and a sinusoidally varying longitudinal velocity. Since the morphodynamic behaviour is mainly determined by the flood and the ebb phase, which have been assumed to be symmetrical, the developing bed-forms (free alternate bars in the case of Seminara and Tubino, 2001) display a vanishing tidal averaged celerity. According to such theoretical results, the wavelength of bars selected by the instability process does not differ much with respect to the fluvial case under dominant suspended load, while the main distinctive feature is the steady character of bed forms.

The major limitation of the above analysis is the assumption of a locally uniform basic flow which changes sinusoidally. In tidal channels the flood and the ebb phases are typically not symmetric: the asymmetry of the flow is mainly due to the non-linear character of the flow field and in particular of the friction term, as pointed out in Chapter 2. The oscillations of flow depth, with larger values during the flood phase and smaller values during the ebb phase, implies that frictional effects are higher during the ebb phase, because they depend on some power of the flow depth with a negative exponent. Moreover, in the fluvial case the longitudinal scale of the channel is much larger than the channel width, while the longitudinal dimension of tidal channels might be comparable with their averaged width. Hence, in the latter case, finite length effects may play an important role in controlling the scale and the topographic expression of tidal bars. This implies that the "local" and the "global" approach cannot be decoupled. Examples of coupled models can be found in Schuttelaars and de Swart (1999), Hibma et al. (2001) and Hibma et al. (2003). The last two contributions propose an application of the well known morphological model Delft 3D,

Figure 1.6: Channels in the Venice lagoon. (Courtesy of Walter Bertoldi, 2003)

whose results seem quite different from the theoretical predictions of Seminara and Tubino (2001).

The complexity of the above picture is further enhanced by the tendency of fine sediment bars to emerge from the free surface forming islands. A similar behaviour is observed also in gravel bed rivers at relatively high values of the width to depth ratio. A possible explanation for such phenomenon can be related to the reduced stabilising effect of gravity when suspended load is dominant. In fact, suspended load is not directly influenced by gravitational effects, as pointed out by Talmon et al. (1995), since suspended sediments don't move "over" the bed but "within" the water column, while bed load is affected by gravity which moves sediments downslope from the top of bars to the pools. In gravel bed rivers this provides a stabilising contribution which inhibits the growth of bars and prevents the formation of islands.

The high complexity inherent in the dynamics of tidal systems can be considered one of the main reasons why results of the existing mathematical models still do not agree on many subtopics. Sound predictions of the morphodynamic evolution of tidal channels require a deep understanding of the physics involved and a careful model setup.

Namely, at least a suitable predictive model of the morphodynamic behaviour of tidal channels shall incorporate the following crucial aspects: the strongly non-linear character of the physical processes and the presence of suspended load. The equations for the flow field and the bottom evolution are non-linear, while most of the theoretical results presently available have been obtained through linearized models. Hence, in the present work suitable numerical models are introduced

to solve the complete set of equations without linearizations. Furthermore, when suspended load is included, results for bottom topography crucially depend on the ability of the model to reproduce adequately the adaptation of the concentration profiles to variable flow conditions, which implies, at least within the context of a meso-scale analysis, the adoption of a three dimensional formulation whereby vertical concentration profiles can be estimated.

Hence, two different models have been developed in the present work, a 1D model and a 3D model. The former is introduced to investigate the propagation of the tidal wave in convergent and non-convergent estuaries and to study large scale morphodynamic processes. The three dimensional model is then used to characterise the role of suspended sediment load on the formation of estuarine and river free bars. More specifically the model is applied within the context of a "local" approach to study the stability of bar-forms. Hence, the procedure adopted herein allows one to investigate not only the initial process of bar formation (when the amplitude of bed-form is small and a linearized approach is also applicable) but also its finite amplitude behaviour, which cannot be studied within a linear framework.

For the sake of simplicity and of wider generality the numerical models are not applied to real estuaries, though the ranges of values of the relevant parameters have been selected in order to simulate real cases. The models are applied to rectangular channels, both with convergent and non convergent geometry, and subjected to a simple semi-diurnal M_2 tide, without over-tides.

It is useful to recall that the gravitational effect due to the moon is purely sinusoidal, therefore in the open sea the free surface oscillation is very close to a sinusoidal function (commonly referred to as the M_2 tide). Over-tides are measured as the difference with respect to such pure sinusoidal behaviour and appear as the higher frequency components of the tidal oscillation. They originate from non-linear effects due to water flow, that characterise every real case.

The present work is organised as follows. In Chapter 2 the main distinctive features of tide propagation in convergent estuaries are summarised; in Chapter 3 the large scale morphodynamical processes in convergent estuaries are investigated through 1D numerical model. Chapter 4 is devoted to the formulation of the three-dimensional model for the study of meso-scale development of tidal channels; the detailed description of the numerical model follows in Chapter 5. In Chapter 6 the process of free bars formation in sandy rivers and tidal channels is investigated. Finally, in Chapter 7 a comparison is presented between the results obtained using different models for the suspended sediment load along with some concluding remarks on the predictive ability of approximate models.

2 On tide propagation in convergent and non-convergent channels

In this chapter we focus on the main hydrodynamic properties of tidal channels, namely those associated with tide propagation in tide dominated estuaries. We will show that a fully non-linear hydrodynamic model is required to capture the most relevant elements of their behaviour. Tide dominated estuaries usually have a funnel shape (figure 2.1) characterised by the presence of sand waves, intertidal flats and salt marshes. The morphodynamic behaviour of such systems depends strongly by upstream propagation of the tide. The celerity at which tide moves along the estuary is governed by the shallow water equations and is therefore an increasing function of water depth. As a result of this depth dependence, tides are deformed during their propagation: flood velocities are greater than ebb velocities and the flood-phase is generally shorter than the ebb-phase. The upstream decrease of the cross sectional area (depth and width of the channel) forces the tide to increase its amplitude during upstream propagation; however, frictional dissipation tends to counteract this effect, decreasing the amplitude of tidal wave. "Hypersyncronous" estuaries are those where the effect of channel convergence is dominant and the wave is amplified; around the world many examples of such systems can be found, like the Scheldt (Netherlands - see figure 1.3).

Besides the geometrical characteristics of tidal channels, the hydrodynamics of estuaries is strongly affected by many other elements, like the presence of short waves incoming from the sea or due to the wind. Moreover in some cases the river discharge at the landward end of the channel plays an important role and may induce stratification phenomena and density driven circulations. Here we restrict the analysis to a widespread class of tidal inlets, namely the well-mixed estuarine channels. This kind of morphological large-scale elements includes those estuaries and lagoon channels where the tidal forcing is so strong that stratification does not occur. The absence of the salt wedge allows one to consider a constant water density and to describe the flow field using the usual equations of single-phase fluid.

Understanding the hydrodynamics of tidal channels is relevant for many environmental issues. In particular, for the evaluation of the consequences of both natural and anthropogenic modifi-

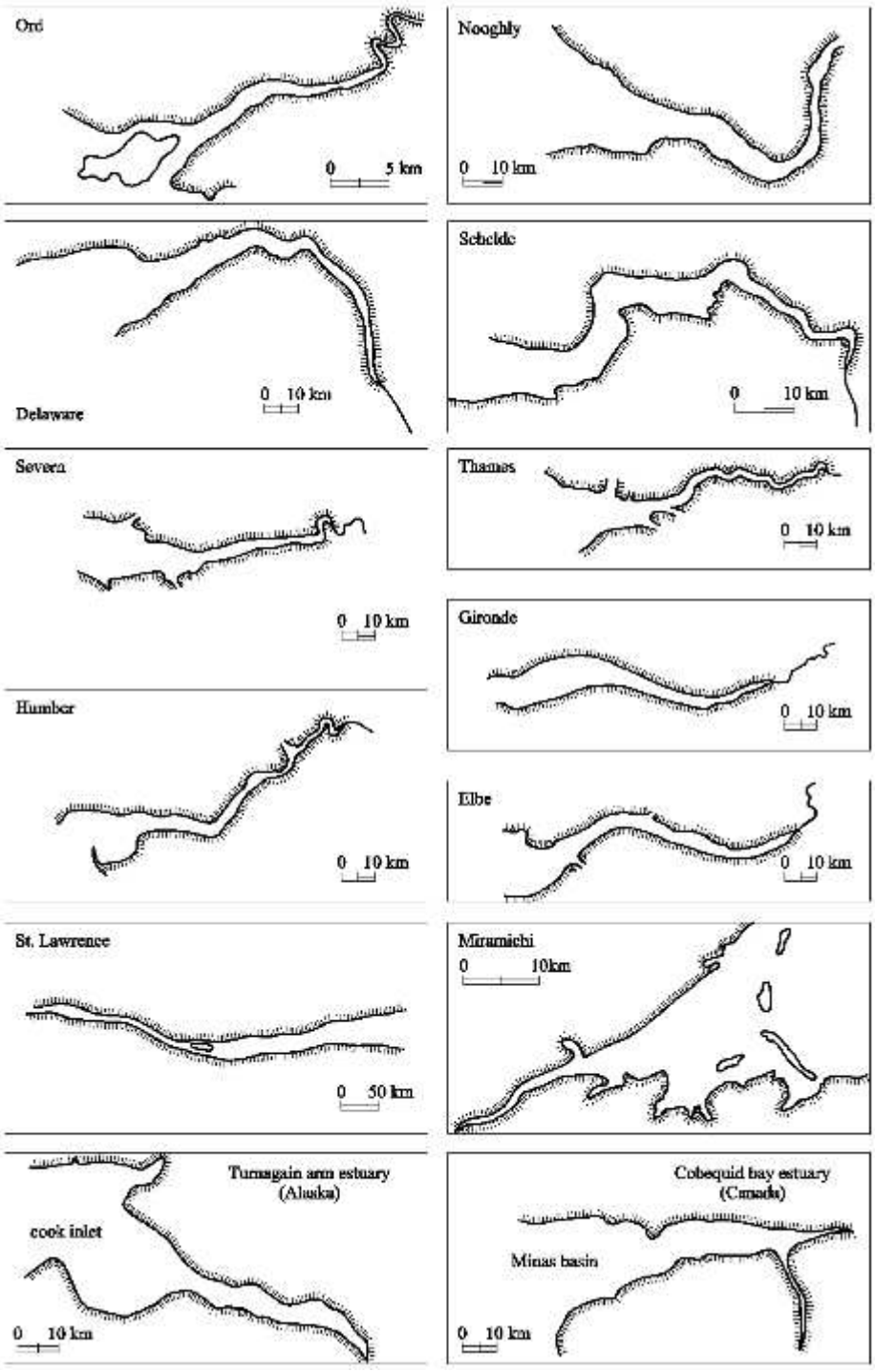

Figure 2.1: Funnel shaped estuaries, from Seminara et al. (2001a)

cations, it is essential to describe the role of several basic factors (length of the estuary, friction, channel convergence, bed altimetry, river discharge) on the properties of the tidal wave (see also Toffolon, 2002).

The problem of the propagation of the tidal wave in convergent channels has been tackled by several authors in recent years (e.g. Friedrichs and Aubrey, 1994; Friedrichs et al., 1998; Lanzoni and Seminara, 1998), following the contribution of Jay (1991), who has first revisited the problem of tide amplification due to channel convergence, originally investigated by Green (1837). Though these theories provide valuable results for the comprehension of the basic mechanisms, they mostly rely on the assumption that some parameters can be considered small so that the mathematical description of the system can be simplified through linear or weakly non-linear analysis.

In the present work we try to remove the above restriction and to investigate large amplitude effects on tidal wave propagation, tackling the fully non-linear problem through a suitable numerical model.

We recall that among the few fully non-linear models that have been recently applied to these issues (Hibma et al., 2001, 2003) most of them have been devoted mainly to characterise the morphodynamic behaviour of tidal channels rather than the process of tide propagation.

Tidal waves are driven by water oscillations imposed at the channel mouth, which is connected with the outer sea. Almost all the non-linear terms appearing in the governing equations for the flow field are proportional to the ratio

$$\varepsilon = \frac{a_0}{D_0} \tag{2.1}$$

between the tidal amplitude a_0 and the average water depth D_0, where the subscript $_0$ denotes the values at the channels mouth. The above mentioned analytical solutions assume the ratio ε to be small enough for its effect to be negligible, at least at the leading order of approximation. We may notice that ε ranges between 0 and 1 and in many real estuaries it can reach relatively large values, as shown in table 2.1.

Notice that tidal wave generates over-tides along its propagation. For the sake of simplicity, in the present work we neglect the effect of external over-tides and force the system with a purely sinusoidal semi-diurnal M_2 tide at the mouth of the estuary. Over-tides, like the quarter-diurnal M_4, occur at the mouth of estuaries when the offshore shelf is relatively wide and flat; moreover the presence of a wider wave spectrum at the channel inlet may affect the overall hydrodynamics of the system, while increasing the number of degrees of freedom in the analysis. Accounting for the effects of over-tides is beyond the aim of the present analysis.

Estuary	$a_0[m]$	$D_0[m]$	ε
Outer Bay of Fundy	2.1	60.0	0.04
Bristol Channel	2.6	45.0	0.06
Hudson	0.69	9.2	0.08
Irrawaddy	1.0	12.4	0.08
Rotterdam Waterway	1.0	11.5	0.09
Columbia	1.0	10.0	0.10
Potomac	0.65	6.0	0.11
Delaware	0.64	5.8	0.11
Soirap	1.3	7.9	0.16
Fraser	1.5	9.0	0.17
Khor	1.3	6.7	0.19
Elbe	2.0	10.0	0.20
Severn	3.0	15.0	0.20
Tees	1.5	7.5	0.20
Gironde	2.3	10.0	0.23
Thames	2.0	8.5	0.24
Scheldt	1.9	8.0	0.24
Hoogly	2.1	5.9	0.36
St. Lawrence	2.5	7.0	0.36
Fleet	0.6	1.5	0.40
Ord	2.5	4.0	0.63
Conwy	2.4	3.0	0.80
Tamar	2.6	2.9	0.90

Table 2.1: Values of the amplitude ratio ε for various estuaries, evaluated using the data reported by Lanzoni and Seminara (1998).

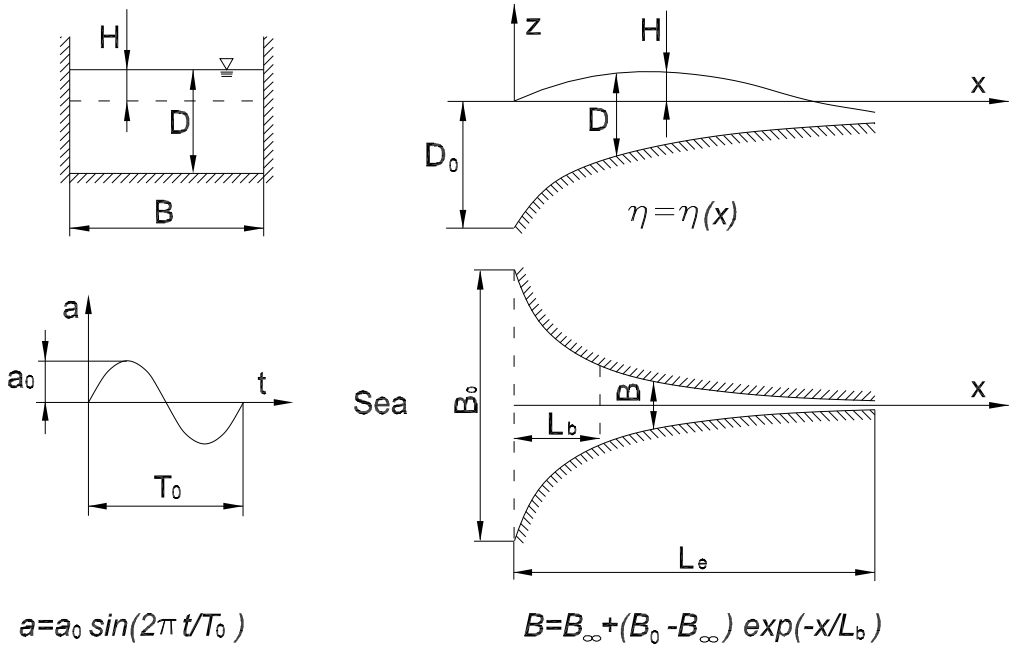

Figure 2.2: Sketch of the estuary and basic notation.

2.1 Formulation of the 1D problem

We consider a tidal channel with varying width and depth and we investigate the propagation of the tidal wave through a one-dimensional cross-sectionally averaged model, with the longitudinal coordinate x directed landward, starting from the mouth of the estuary. The seaward boundary condition is given, in terms of the free surface, by the sea level, which is assumed to be determined by the tidal oscillation without any influence of the internal response of the estuary. We also assume that a rectangular cross-section is suitable to describe, as a first approximation, the behaviour of a real section of the channel. The problem is treated in dimensional form, because, as it will be pointed out in the next sections, suitable scales are difficult to be found a priori.

The above assumptions may be rather strong, since they imply that the model is unable to account for topographically driven effects on the flow field as well as to include the role of shallow areas adjacent to the main channel. A more refined approach would imply the matching of the one-dimensional (global) model with a "local" model based on a characteristic length scale of the order of channel width, where the above effects can be accounted for (see Chapter 4). The sketch of the geometry of the idealised tidal channel adopted in the present analysis is given in figure 2.2. The typical funnel shape is assumed and represented employing an exponentially decreasing function of the longitudinal coordinate x, as assumed by many authors in the past (Friedrichs and Aubrey,

1994; Lanzoni and Seminara, 1998), according to the relationship:

$$B = B_\infty + (B_0 - B_\infty)\exp\left(-\frac{x}{L_b}\right) \tag{2.2}$$

where L_b is the convergence length and the asymptotic width B_∞ is included to set a minimum width landward, also in the case of strong convergence and long estuary. The standard one-dimensional shallow water equations are used, which read:

$$\frac{\partial Q}{\partial t} + \frac{\partial}{\partial x}\left(\frac{Q^2}{\Omega}\right) + g\Omega\frac{\partial h}{\partial x} + g\Omega j = 0, \tag{2.3a}$$

$$\frac{\partial \Omega}{\partial t} + \frac{\partial Q}{\partial x} = 0, \tag{2.3b}$$

where t is time, x the longitudinal coordinate, Q is the water discharge, Ω is the area of the cross section, h is the free surface elevation, g is gravity; furthermore, the water depth $D = H - \eta$ is defined in terms of bottom elevation η as shown in figure 2.2; the frictional term is evaluated in the following form:

$$j = \frac{Q|Q|}{g\Omega^2 C_h^2 R_h} \tag{2.4}$$

having denoted with C_h the dimensionless Chézy coefficient and with R_h the hydraulic radius:

$$R_h = \frac{BD}{B+2D}.$$

As for the longitudinal bottom profile, it is commonly observed that in tidal channels the flow depth decreases landward. Prandle (1991) founds that the behaviour of the width and depth of real estuaries can be described in terms of power laws. Bottom profiles may be chosen analytically (e.g. linear, exponential) or evaluated through morphological models as pointed out in Chapter 3. In the present chapter, as first step of the analysis, we assume the bed to be horizontal, in order to reduce the number of independent variables.

The most suitable form for the numerical solution of the flow equations is (2.3), because it is a semi-conservative form. In order to point out the role played by different terms it is convenient to rewrite the system in non-conservative form. Moreover channel convergence can be written as follows:

$$\frac{1}{B}\frac{dB}{dx} = -\frac{1}{L_b}\frac{B - B_\infty}{B} \cong -\frac{1}{L_b}, \tag{2.5}$$

which is valid when the asymptotic width B_∞ is much smaller than the actual width $B(x)$. In this case the dependence of the solution on the actual width of the channel can be ruled out, as it can be readily seen from equations (2.3a-2.3b), rewritten in non-conservative form in terms of the

cross-sectionally averaged velocity $U = Q/\Omega$:

$$\frac{\partial U}{\partial t} + U\frac{\partial U}{\partial x} + g\frac{\partial h}{\partial x} + gj = 0, \tag{2.6a}$$

$$\frac{\partial D}{\partial t} + D\frac{\partial U}{\partial x} + U\frac{\partial D}{\partial x} - \frac{UD}{L_b} = 0, \tag{2.6b}$$

Please note that the non linear terms in (2.6a) are the advective term $U\frac{\partial U}{\partial x}$ and the frictional term gj, while the last term in (2.6b) is related to channel convergence.

2.2 Numerical solution

The system (2.3) is solved numerically in order to retain all the non-linear terms. As pointed out before the more suitable form for the numerical solution is (2.3), because it preserve the conservation of mass and momentum. It can be shown that the system is hyperbolic, with eigenvalues equal to:

$$\Lambda_{1,2} = U \pm \sqrt{g\frac{\Omega}{B}} \tag{2.7}$$

The eigenvalues (2.7) of the system (2.3) are always distinct and generally have opposite sign in tidal system. Two boundary conditions are required by the system (2.3), one corresponding to each eigenvalue. This implies that boundary conditions must be imposed at each sides: the mouth of the channel and its landward end.

Equations (2.3a-2.3b) are discretized through finite differences, with spatial step Δx and time step Δt, and are solved numerically using the explicit MacCormack (1969) method. The method consists of two steps: prediction and correction. The former is made using a forward difference while the latter with backward finite difference. This numerical method has a second order accuracy both in space and in time. The stability condition requires the Courant-Friedrichs-Levi number (CFL) not to exceed the unity:

$$CFL = \frac{\Lambda_{max}}{\Delta x}\Delta t \leq 1 \tag{2.8}$$

where $\Lambda_{max} = max(|\Lambda_1||\Lambda_2|)$ is the leading eigenvalue. Since the tidal wave tends to break during its propagation due to non-linear terms, namely those associated with the effect of friction and convergence, a suitable artificial viscosity is introduced through a TVD filter (Total Variation Diminishing) in order to remove the spurious oscillations around discontinuities, that are typical of second-order central schemes (see, for instance, Garcia-Navarro et al., 1992).

Results can be given in term of Fourier modes, because in each section of the estuary the solution for the flow field is a periodic function, with a period equal to that of the tidal oscillation

imposed at the seaward boundary. Hence, results for the free surface elevation and for the flow velocity can be given the form of a standard Fourier representation:

$$h(x,t) = h_0 + \sum_{n=1}^{\infty} h_n(x)\, sin\left(n\omega t + \Phi_n^H\right), \tag{2.9}$$

$$U(x,t) = u_0 + \sum_{n=1}^{\infty} u_n(x)\, sin\left(n\omega t + \Phi_n^U\right), \tag{2.10}$$

where $\omega = 2\pi/T_0$ is the tidal frequency, T_0 is the tidal period, h_n and u_n are the $n-th$ components of free surface elevation and velocity, respectively, and Φ_n is the phase lag of the $n-th$ harmonic. In equations (2.9 and 2.10) $n = 1$ corresponds to the semi-diurnal M_2-tide, $n = 2$ to M_4-tide and so on.

2.3 Boundary conditions

The Mac-Cormack scheme consists of to steps: prediction (forward difference) and correction (backward difference), implying the need of four boundary condition, which are the free surface elevation and the value of flow discharge at each boundary. Two of these conditions are physically based, corresponding to the two distinct eigenvalues (2.7).

The seaward boundary condition is straightforward: we impose that the free surface level is given by the semi-diurnal M_2 tide, whose period and peak amplitude at the mouth are denoted by T_0 and a_0, respectively:

$$h(x=0,t) = a_0 sin\left(\frac{2\pi}{T_0}t\right). \tag{2.11}$$

At the landward boundary we impose a suitable relationship between the free surface level and water discharge. It is difficult to impose such condition, because many estuaries strongly interact and superpose to the final reaches of rivers. Frequently the presence of a peculiar geometrical configuration induces a reflection of the tidal wave. Two limit cases can be recognised:

1. the reflecting barrier: this situation corresponds to the assumption of vanishing discharge at the landward end of the computational domain

$$Q(x = L_e, t) = 0, \tag{2.12}$$

   and determines the complete reflection of the tidal wave.

2. the transparent condition: this condition refers to a situation such that no obstacles are present at the landward end and the tidal wave exits from the computational domain without being deformed or reflected. In this case the model reproduces the typical behaviour of a

long estuary, for which the effect of the landward boundary condition is not relevant. The transparent condition is given considering the outgoing characteristic curve, corresponding to the positive eigenvalue λ_1, that reads:

$$\frac{dh(x=L_e,t)}{dt} = \frac{\partial h}{\partial t} + \lambda_1 \frac{\partial h}{\partial x} \tag{2.13a}$$

$$\frac{dQ(x=L_e,t)}{dt} = \frac{\partial Q}{\partial t} + \lambda_1 \frac{\partial Q}{\partial x} \tag{2.13b}$$

Recalling that to ensure stability requirement the Courant-Friedrichs-Levi number $C = \lambda_1 \Delta t/\Delta x$ must not exceed the unity and approximating the characteristic curve by a linear function the conditions (2.13) in discrete form become:

$$h_N^{k+1} = h_{N-1}^k C + (1-C)\, h_N^k \tag{2.14a}$$

$$Q_N^{k+1} = Q_{N-1}^k C + (1-C)\, Q_N^k \tag{2.14b}$$

where the subscript $_N$ represents the index of the last section and the superscripts k and $k+1$ represent respectively the present and the following time step.
Notice that, as pointed out by Friedrichs and Aubrey (1994), the landward boundary condition is less important in the case of strongly convergent channels.

In addition to the physically based boundary conditions the numerical scheme requires other two conditions, called "fictitious", which have been imposed using the forcing term, if it is possible as in the case of the transparent conditions, or otherwise by solving the system of the flow field.

2.4 External parameters

The hydrodynamics of tidal channels is controlled by three main effects: channel convergence and the relative balance of inertia and friction. The relative weight of such effects can be quantify through the introduction of suitable dimensionless parameters.

We define the above parameters in terms of external quantities, namely all the geometrical and morphodynamical quantities: the amplitude of tidal excursion at the mouth a_0, the reference values of channel width B_0 and depth D_0, the characteristic length of width variation along the estuary L_b and the friction factor C_h. Furthermore, the length of the estuary itself, which embodies the influence of the landward boundary condition, often plays a crucial role in the definition of the flow field.

We consider the reference velocity as an internal quantity, since its value is only determined once the other parameters are given, and it is the result of the hydrodynamical problem. Conse-

quently, all the parameters defined in the following only imply an evaluation of a velocity reference value in terms of external quantities.

A first relevant external parameter is the dimensionless tidal amplitude ε, defined in (2.1).

When frictional effects are negligible, the linearized theories (see section 2.5 for further details) are suitable tools for the understanding of the flow field; the linear solution in an infinitely long channel with constant width is a wave function whose celerity is:

$$c_0 = \sqrt{gD_0}. \tag{2.15}$$

Hence, a frictionless wavelength can be defined as

$$L_g = \sqrt{gD_0}T_0, \tag{2.16}$$

which can be taken as a reference length scale. Furthermore, when the role played by the frictional term is negligible, a frictionless velocity U_g can be defined in terms of external parameters in the following way:

$$U_g = \varepsilon\sqrt{gD_0} = \frac{a_0 L_g}{D_0 T_0}. \tag{2.17}$$

The relative role of friction can be quantified, like in Lanzoni and Seminara (1998), in terms of the ratio between frictional terms R and inertial terms S in momentum equation:

$$\frac{R}{S} = \frac{U_0 T_0}{C_h^2 D_0}. \tag{2.18}$$

Notice, however, that the above ratio is defined in term of *a priori* unknown velocity scale U_0. In order to define the ratio R/S in terms of external variables we use U_g (defined in 2.17) instead of U_0 to write

$$\chi = \frac{a_0 L_g}{C_h^2 D_0^2} = \varepsilon\frac{L_g}{C_h^2 D_0}. \tag{2.19}$$

The parameter χ represents the ratio between friction and inertia. Since χ is linearly proportional to ε, it follows that high values of ε can be related in almost all cases to frictionally dominated estuaries. Notice that in real estuaries χ may range between $4-5$ and 100. The smaller values correspond to very deep estuaries, like the Bay of Fundy (flow depth $\sim 60m$) or the Bristol Channel (flow depth $\sim 45m$), which are relatively rare to be found around the world. The χ values of most of the natural estuaries is indeed much higher.

To account for the effect of width variation along the estuary, a dimensionless convergence ratio can be defined in the form:

$$\gamma = \frac{L_g}{L_b}, \tag{2.20}$$

where L_b is the convergence length defined in (2.2).

The reference velocity U_0 can be defined in a straightforward way only for some specific cases. In the case of validity of linear theories, when both ε and channel convergence γ are small, the scale of velocity U_0 coincides with U_g, furthermore, in strongly convergent estuaries a suitable velocity scale can by readily obtained in the following form (Toffolon, 2002)

$$U_0 = \frac{2\pi}{\gamma - 4} U_g, \tag{2.21}$$

where the limit $\gamma = 4$ has been tacked into account as the lowest, according to Jay (1991) and Lanzoni and Seminara (1998). In the case of strongly dissipative and weakly convergent channels the role played by inertia is negligible, friction is balanced by the gravitational term and the following velocity scale is found:

$$U_0 = \left(\frac{2\pi}{\chi}\right)^{\frac{1}{3}} U_g \tag{2.22}$$

Recently Toffolon (2002) has proposed a more general, albeit simplified, formulation to evaluate a reference value of velocity at the mouth of the estuary, in terms of external parameters. Such formulations can be applied to both strongly or weakly convergent estuaries as well as to friction dominated or frictionless channels. It is based on the analysis of the relative weight of the various terms in the momentum and continuity equations (2.6a - 2.6b): through dimensional considerations, it leads to the following relationship for the velocity scale U_0, defined as the algebraic mean of peak values of flood and ebb velocity at the mouth of the estuary:

$$U_0 = \frac{1}{\widehat{\chi}} \left(\Delta - \frac{1}{\Delta} \frac{\widehat{\gamma}}{\widehat{\chi}} \right) U_g, \tag{2.23}$$

where

$$\Delta = \left[1 + \sqrt{1 + \left(\frac{\widehat{\gamma}}{\widehat{\chi}} \right)^3} \right]^{\frac{1}{3}}, \quad \widehat{\chi} = \left(\frac{\chi}{\pi} \right)^{1/3}, \quad \widehat{\gamma} = \frac{\gamma - 4}{3\pi}. \tag{2.24}$$

Equation (2.23) includes and improves the relationships proposed to cover the asymptotic case of strongly-convergent and weakly-dissipative estuaries and its dual case. Equation (2.23) indeed reduces to (2.21) in the case of strongly convergent channels, corresponding to high values of γ, for strongly dissipative estuaries (high values of χ) the (2.22) is obtained. Also notice that (2.23) refers to constant depth channels and is valid provided the frictionless limit $U_0 < U_g$ is satisfied. The approximate velocity scale (2.23) is plotted, as a function of the parameters χ and γ, in figure 2.3, where also a comparison is made with the velocity evaluated numerically at the mouth of the

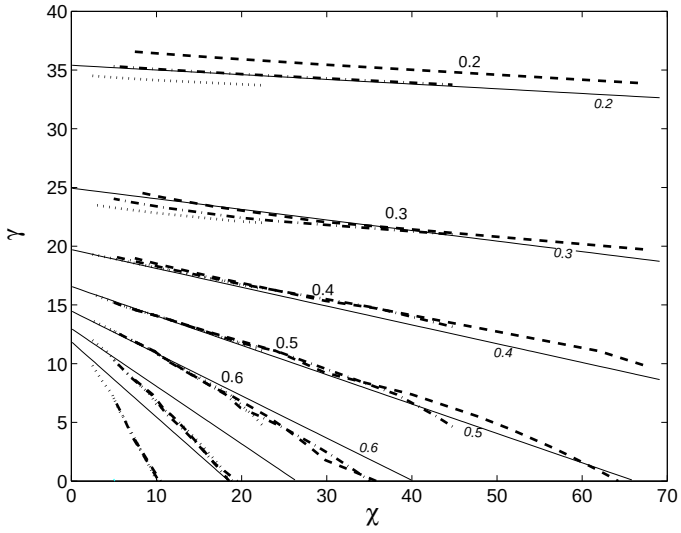

Figure 2.3: Contour plot of the ratio U_0/U_g evaluated using the (2.23) (continuous lines) and the algebraic mean of peak values of flood and ebb velocity at the mouth evaluated using the numerical model (dotted lines). The different dotted lines are obtained through different values of ε in order to obtain a wider range for χ. $L_b = \infty \div 10km$, $D_0 = 10m$, $k_s = 30 \div 90m^{1/3}s^{-1}$ ($k_s = \sqrt{g}C_h R_h^{-1/6}$), transparent boundary condition landward, $L_e = 300km$, $a_0 = 0.01 - 0.1 - 0.5 - 1 - 2 - 3m$.

estuary, as the algebraic mean of the peak values of flood and ebb phase at the mouth:

$$\frac{1}{2}\left(\left|U\left(x=0\right)_{flood}\right|_{max} + \left|U\left(x=0\right)_{ebb}\right|_{max}\right).$$

2.5 Tide propagation

The characteristics of the tidal wave, namely the amplitude, the shape, the celerity and the phase lag between free surface elevation and flow velocity, change along the estuary. Their variation depends on the external conditions of the estuary, quantified by the parameters γ and χ, defined in the previous section.

As a fist step let us consider a tide with a very small amplitude a_0, such that a linearized set of equations can be used to describe adequately the system. Considering a channel with constant width and horizontal bed profile it is possible to made the problem (2.6a-2.6b) dimensionless using

the following scales, where the superscript $^+$ denote the dimensionless quantities:

$$t = T_0 t^+,$$

$$x = L_g x^+,$$

$$U = U_g U^+,$$

$$D = D_0 D^+,$$

$$H = a_0 H^+.$$

System (2.6a-2.6b) can be rewritten in the following form in the case of vanishing channel convergence:

$$\frac{\partial U^+}{\partial t^+} + \varepsilon U^+ \frac{\partial U^+}{\partial x^+} + \frac{\partial H^+}{\partial x^+} + \varepsilon \frac{U^{+2}}{g C_h^2 D^+} = 0 \tag{2.25}$$

$$\frac{\partial D^+}{\partial t^+} + \varepsilon D^+ \frac{\partial U^+}{\partial x^+} + \varepsilon U^+ \frac{\partial D^+}{\partial x^+} = 0 \tag{2.26}$$

recalling that $D = D_0 + H$ and therefore $D^+ = 1 + \varepsilon H^+$, if ε is small the non linear terms in equation (2.25) are negligible and the system can be rewritten in the following form:

$$\frac{\partial U^+}{\partial t^+} + \frac{\partial H^+}{\partial x^+} = 0 \tag{2.27}$$

$$\frac{\partial H^+}{\partial t^+} + \frac{\partial U^+}{\partial x^+} = 0 \tag{2.28}$$

which leads to the classic wave equation

$$\frac{\partial H^+}{\partial t^{+2}} - \frac{\partial H^+}{\partial x^{+2}} = 0 \tag{2.29}$$

for the water level; a similar wave equations may be written also for the flow velocity. The solution of the (2.29) strongly depends on the boundary conditions. Assuming a purely M_2 tidal forcing at the channel mouth, it is possible to recover the simple wave behaviour

$$H^+ = \sin\left[2\pi\left(x^+ - t^+\right)\right] \qquad U^+ = \sin\left[2\pi\left(x^+ - t^+\right)\right] \tag{2.30}$$

assuming an open landward boundary (infinitely long channel), while the solution becomes a standing wave

$$H^+ = \frac{\cos\left(2\pi\left(L_e^+ - x^+\right)\right)}{\cos\left(2\pi L_e^+\right)} \sin\left(2\pi t^+\right) \qquad U^+ = \frac{\sin\left(2\pi\left(L_e^+ - x^+\right)\right)}{\cos\left(2\pi L_e^+\right)} \cos\left(2\pi t^+\right) \tag{2.31}$$

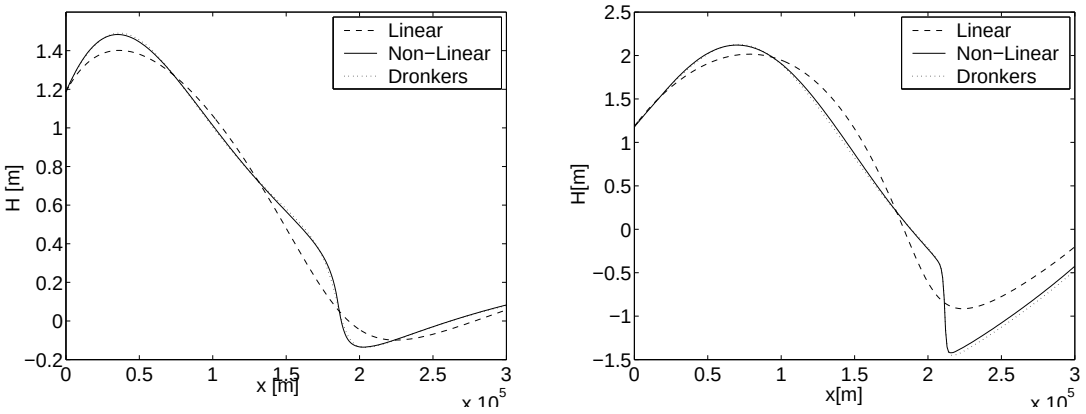

Figure 2.4: Free surface profiles along a sample estuary with length $L_e = 300km$ for non convergent ($\gamma = 0$, left) and convergent channel ($\gamma = 7.4$, right). $\varepsilon = 0.2$, $k_s = 45m^{1/3}s^{-1}$ ($k_s = \sqrt{g}C_h R_h^{-1/6}$), $D_0 = 10m$, transparent boundary condition.

when a reflective landward barrier ($U(x^+ = L_e^+) = 0$) is considered. Please note that water level and velocity are, respectively, in phase in the former case and out of phase of $\pm\frac{\pi}{2}$ in the latter, when resonant conditions are attained for $L_e = \frac{2m-1}{4}L_g$, with m natural number. For these channel length (e.g. $L_e = \frac{L_g}{4}, L_e = \frac{3L_g}{4}, ...$) the tidal forcing term is in phase with the internal response of the system. The (2.31) is then no more valid, because the denominator is vanishing.

When the tide amplitude is greater the non-linear terms play a non negligible role. Two most relevant effects can be highlighted, that don't appear in (2.30) and (2.31). First of all the tidal amplitude is damped due to frictional effects. Moreover during its propagation the tidal wave doesn't keep a regularly sinusoidal as higher order harmonic components are generated. The latter effect is related to the shallow water character of the system (2.6a-2.6b): the wave celerity is an increasing function of the flow depth. In convergent estuaries tidal waves strongly modify their shape, amplify and tend to form shock waves, which propagate quite rapidly in the landward direction. As a result the wave profile is deformed as indicated in figure 2.4. Results of numerical simulations suggest that the frictional non-linear term plays an important role, greater than that of the advective term. In order to point out the role of the frictional term a comparison between the results obtained using different closures for the dissipation term is shown in figure 2.4, where longitudinal profiles of the free surface are plotted, both for non-convergent (left) and convergent ($\gamma = 7.4$, right) estuaries. The linear solution is obtained using a linearized formulation for the frictional term j, which can be written, using the first order term of the Lorenz (1922) transformation, in the following form:

$$j = \frac{8}{3\pi}\widetilde{U}\frac{U}{k_s^2 R_h^{4/3}}, \tag{2.32}$$

where $k_s = \sqrt{g} C_h R_h^{-\frac{1}{6}}$ and $\widetilde{U}$ is a characteristic maximum value of local velocity, evaluated at each cross section, as the algebraic mean of the peak values of flood and ebb phase:

$$\widetilde{U}(x) = \frac{\left|U(x)_{flood}\right|_{max} + \left|U(x)_{ebb}\right|_{max}}{2}$$

It is worth noticing that the solution obtained using (2.32) does not generate shocks. On the contrary, higher order formulations for the frictional term, like that proposed by Dronkers (1964), lead to some results comparable to those obtained using the complete non-linear formulation. When U is a periodic function with zero mean, Dronkers relationship can be expressed using Chebyshev polynomials as follows:

$$j = \frac{16}{15\pi} \frac{\widetilde{U}^2}{k_s^2 R_h^{4/3}} \left[\frac{U}{\widetilde{U}} + 2 \left(\frac{U}{\widetilde{U}} \right)^3 \right]. \tag{2.33}$$

A quantitative comparison of tidal wave characteristics, for different choices of model parameters, can be given in terms of the amplitude of the leading Fourier components of the time series of free surface elevation in each cross section. Moreover the Fourier representation allows to investigate the generation of over-tides (e.g. higher order components), which arise from non-linear effects in the governing equations during tide propagation, though the forcing tide is purely M_2 sinusoidal. Over-tides are well represented in figures 2.5 and 2.6 where the amplitudes of the Fourier components are scaled by the amplitude of the semi-diurnal harmonic h_1:

$$A_n = \frac{h_n}{h_1}. \tag{2.34}$$

Results of figure 2.5 are obtained through different closures for the frictional term and for different values of the convergence length. Also the tendency of the tidal wave to break during its propagation is related to non-linear effects driven by the shallow water character of the governing equations, by the frictional term and by channel convergence. At the mouth of the channel ($x = 0$) over-tides are not present, because the boundary condition is a purely sinusoidal oscillation, while moving inside the estuaries several higher order harmonic component are present.

The role of the higher order harmonics may be significant especially if the friction term is represented in non-linear form, as shown comparing figures 2.5 and 2.6 (right). When a linear closure is adopted for the frictional term figure 2.5 (left) the spectrum is characterised by few harmonic components and the occurrence of mode 2 is mainly related to inertial effects. When a non-linear closure is adopted, the amplitude of higher order harmonics is larger and may induce the wave to break. This is shown in figure 2.5 (right) and 2.6 (right) where the Dronkers approximation

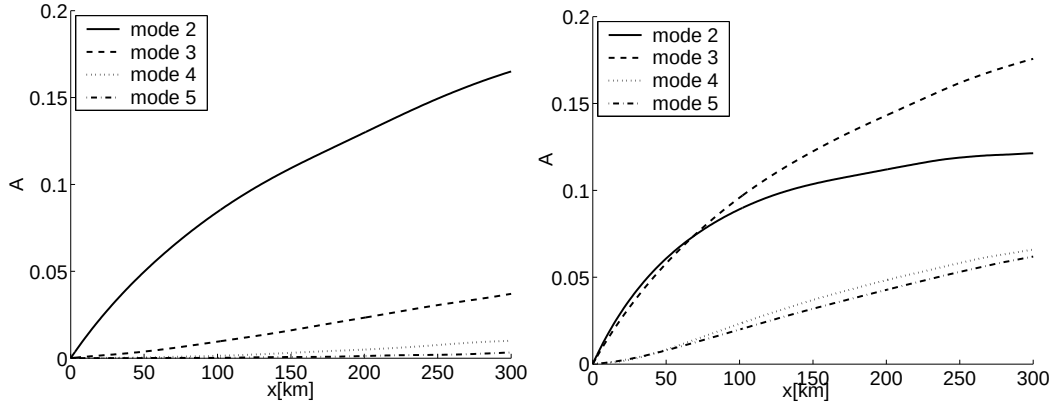

Figure 2.5: Amplitude of the leading order Fourier components of the time series of free surface elevation in each cross section evaluated using (2.32) (left) and (2.33) (right) in a non-convergent channel $\gamma = 0$. The amplitudes are scaled using the value h_1 of mode 1. $\varepsilon = 0.1$, $D_0 = 10m$, $k_s = 45m^{1/3}s^{-1}$ ($k_s = \sqrt{g}C_h R_h^{-1/6}$), and transparent boundary condition.

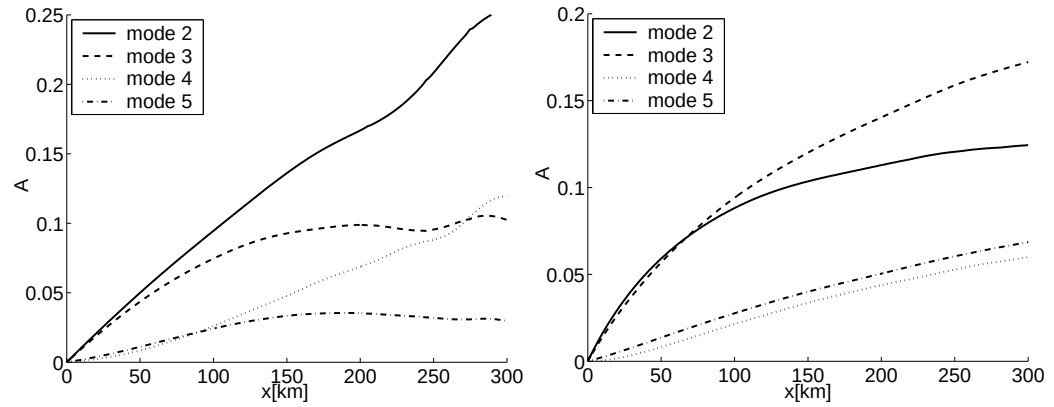

Figure 2.6: Amplitude of the leading order Fourier components of the time series of free surface elevation in each cross section for a convergent $\gamma = 7.4$ (left) and non-convergent $\gamma = 0$ channels (right). The amplitudes are scaled using the value h_1 of mode 1. $\varepsilon = 0.1$, $D_0 = 10m$, $k_s = 45m^{1/3}s^{-1}$ ($k_s = \sqrt{g}C_h R_h^{-1/6}$), fully non-linear closure and transparent boundary condition.

(2.33) and the fully nonlinear formulation (2.4) for j have been adopted, respectively.

Moreover a non-linear term in the continuity equation can arises from channel convergence; if L_b is small enough the term $\frac{UD}{L_b}$ in (2.6b) may lead to the amplification of the even modes of the spectrum, as shown in figure 2.6 (left). Figure 2.6 allow a comparison between the behavior of the free surface in convergent (left) and non-convergent (right) estuaries.

2.6 Non-linear effects on the average water level

Non-linear effects characterising tide propagation, do not influence only the shape of tidal waves, but also the tidally-averaged free surface level, which does not coincide with the mean sea level everywhere along the estuary, even in the case of negligible river discharge. Typically the averaged water level tends to rise landward; this non-linear effect may be point out considering the momentum equation (2.6a), integrating over a tidal cycle obtaining:

$$U(t+T_0) - U(t) + \int_t^{t+T_0} U\frac{\partial U}{\partial x} d\sigma + g\frac{\partial}{\partial x}\int_t^{t+T_0} h d\sigma + g\int_t^{t+T_0} j d\sigma = 0$$

which can be simplified as follow

$$\frac{\partial}{\partial x}\langle h\rangle \cong \langle j\rangle \tag{2.35}$$

since the advective term $U\frac{\partial U}{\partial x}$ is almost negligible everywhere (square brackets denote the average over the tidal cycle). The relationship (2.35) describes the variation of the mean slope of the free surface elevation along the estuary. The tidally averaged frictional term can be written as:

$$\langle j\rangle = \frac{1}{T_0}\int_t^{t+T_0} \frac{Q(\sigma)|Q(\sigma)|}{gB^2C_h^2D^3(\sigma)} d\sigma \tag{2.36}$$

where the hydraulic radius has been approximated by the flow depth. Using the simplest description for the tidal wave, valid in the frictionless case,

$$Q \propto cos(t), \qquad D \propto 1 + \varepsilon cos(t-\phi)$$

where the discharge is assumed to be sinusoidal due to mass conservation requirement, we obtain that the right hand side of (2.35) vanishes when the phase lag $\phi = \pm\pi/2$; moreover, the right hand side is positive in the range $\phi \in (-\pi/2, \pi/2)$, for any value of ε. It is important to note that, within the framework of this simplified approach, the mean slope of the free surface is related to the variation of the flow depth, which introduces a non-linearity through the frictional term.

A comparison between the value $< j >$ obtained from (2.36) and the mean slope of the leading order component of the Fourier representation of the free surface, obtained using the fully non-

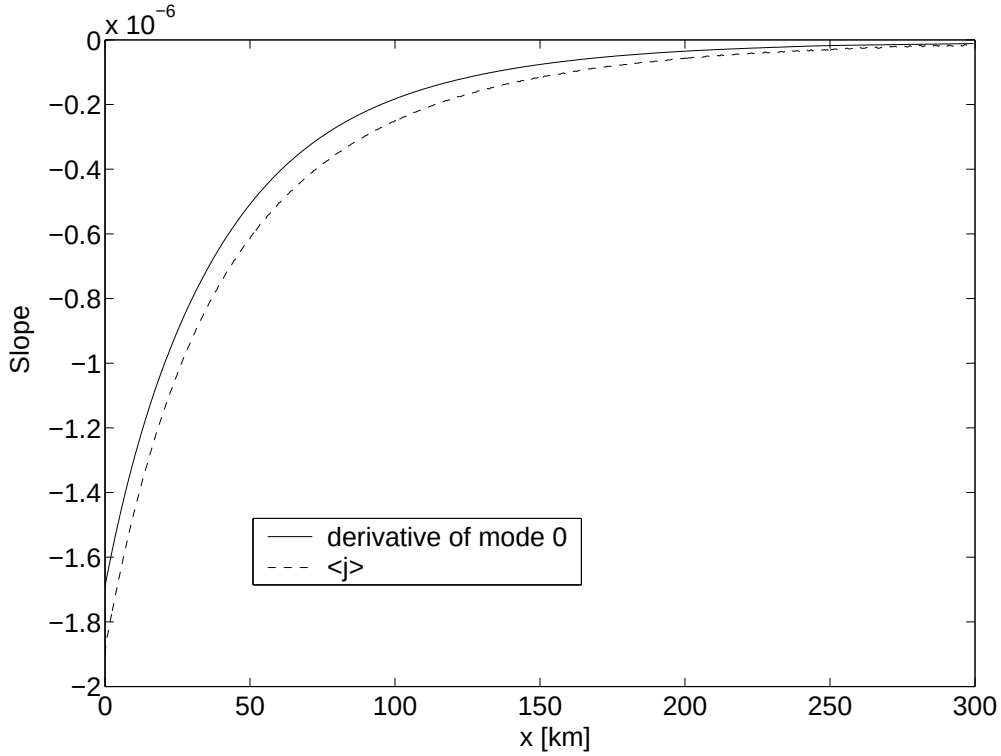

Figure 2.7: Tidally averaged value of the free surface slope evaluated through equations 2.35 and 2.36 or from the longitudinal slope $\partial h_0/\partial x$ of the mode 0 of the spectrum of the free surface elevation. $\varepsilon = 0.1$, $k_s = 45m^{1/3}s^{-1}$ ($k_s = \sqrt{g}C_h R_h^{-1/6}$), $D_0 = 10m$, transparent boundary condition.

linear closure (2.4), is shown in figure 2.7. It is worth noticing that the two curves do not coincide due to the non completely negligible contribution of the advective term $U\frac{\partial U}{\partial x}$. A similar comparison can be given in terms of the value of mode h_0 of the spectrum of the free surface profile along the estuary and the value of the mean free surface elevation obtained through the following equation:

$$\langle h(x)\rangle = -\int_0^x \langle j\rangle \, d\sigma \tag{2.37}$$

Such a comparison is given in figure 2.8 for a convergent estuary ($\gamma = 7.4$). In this case the contribution of the advective term is even more negligible since the longitudinal scale is larger with respect to the case of non-convergent estuaries, as also pointed out by Lanzoni and Seminara (1998) and Friedrichs and Aubrey (1994); hence, in this case the estimates of the mean water level obtained through the numerical model or using the simplified formulation (2.37) are fairly close.

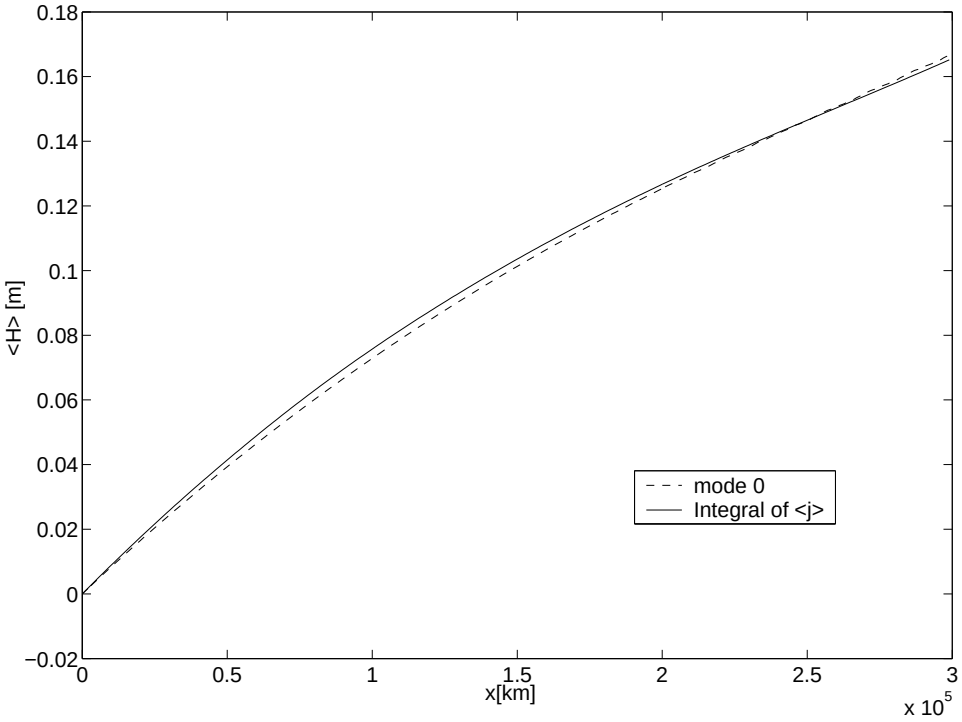

Figure 2.8: Tidally averaged value of the free surface level evaluated through equation 2.37 or from the amplitude h_0 of the mode 0 of the spectrum of the free surface elevation. $\varepsilon = 0.1$, $k_s = 45 m^{1/3} s^{-1}$ ($k_s = \sqrt{g} C_h R_h^{-1/6}$), $D_0 = 10m$, transparent boundary condition.

2.7 Marginal conditions for tide amplification

Tides tend to growth its amplitude for convergent effects, decrease in width resulting from the characteristic funnel-shaped geometry force the tidal wave through smaller cross-sectional areas. The frictional term plays the opposite effects and tends to decrease the amplitude of tidal wave.

The marginal conditions for the amplification of the wave amplitude are defined by those values of the relevant parameters for which the tidal wave does not amplify nor decay during its propagation, within a reach of the estuary relatively close to its mouth. As pointed out before the dynamic balance which governs the amplification of a tidal wave essentially involves convergence and friction; hence, theoretical considerations suggest that marginal conditions are likely to be expressed in terms of the degree of convergence γ and the friction to inertia ratio χ.

A first attempt to characterise the behaviour of a tidal wave in convergent geometries is due to Green (1837), who determined the well known relationship

$$\frac{a(x)}{a_0} = \left(\frac{B_0}{B(x)}\right)^{1/2} \left(\frac{D_0}{D(x)}\right)^{1/4}. \tag{2.38}$$

The Green's law is based on energy conservation considerations and relies on two unrealistic assumptions, namely that energy dissipation is negligible and convergence is much weaker than the tidal wavelength. In particular, the frictionless character of the relationship does not allow one to describe the wave damping. According to (2.38) any degree of channel convergence or decrease of flow depth should result into an amplification of the tidal wave, which is obviously not true in real estuaries.

Jay (1991), Friedrichs and Aubrey (1994) (see also Friedrichs et al. 1998) and Lanzoni and Seminara (1998) have proposed suitable extensions of Green's law that take into account also the role of friction. Their analytical approaches are based on the assumption that the parameter ε is relatively small. As discussed in the preceding sections the order of magnitude of χ is strictly related to ε; hence such condition corresponds to consider weakly dissipative estuaries. On the other hand, in strongly dissipative cases, tide propagation has to be treated as a strongly non-linear process. The above theories, which more or less implicitly consider marginal conditions for tide amplification, lead to relationships for the marginal state that can be cast in the following form:

$$\gamma = k\chi^m. \tag{2.39}$$

For weakly convergent and weakly dissipative estuaries Lanzoni and Seminara (1998) and Friedrichs et al. (1998) have found a linear dependence, hence m=1. On the other hand, for the case of strongly convergent channels, Friedrichs and Aubrey (1994) have found that marginal conditions are attained when the actual celerity c of the tidal wave is equal to the frictionless celerity c_0.

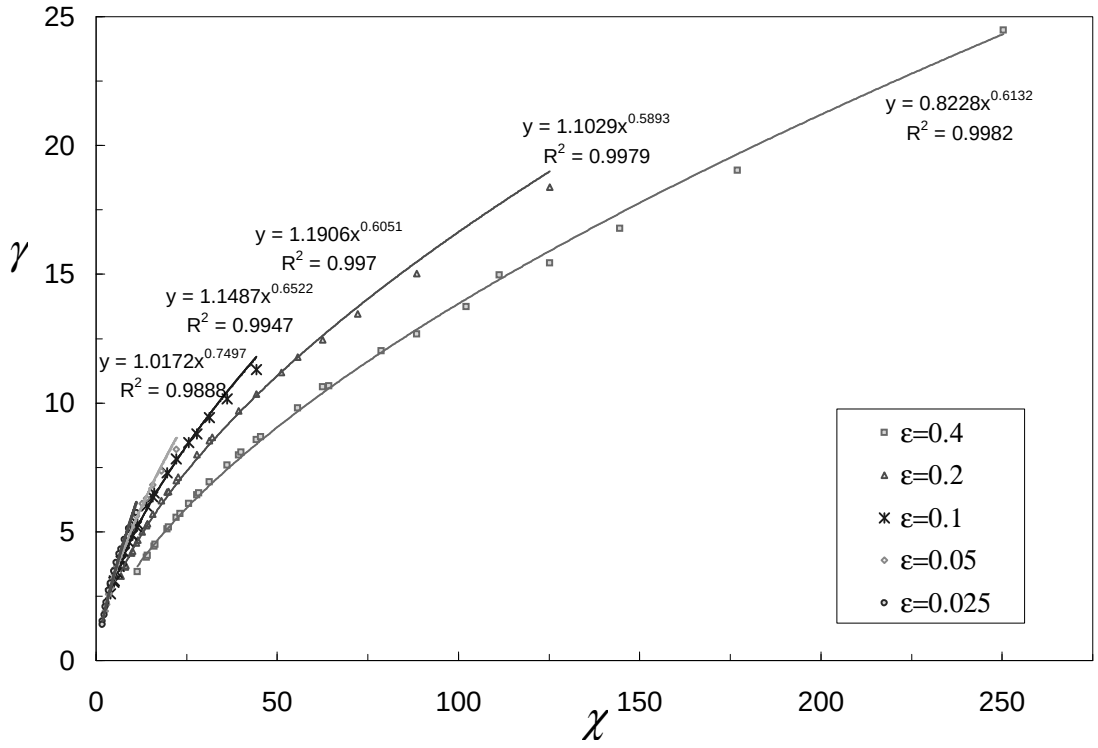

Figure 2.9: Marginal conditions for the amplification of tidal amplitude in the $\chi - \gamma$ plane, for different values of ε, as obtained through the numerical model. The interpolating power laws are reported in the plot with the corresponding correlation coefficient R^2.

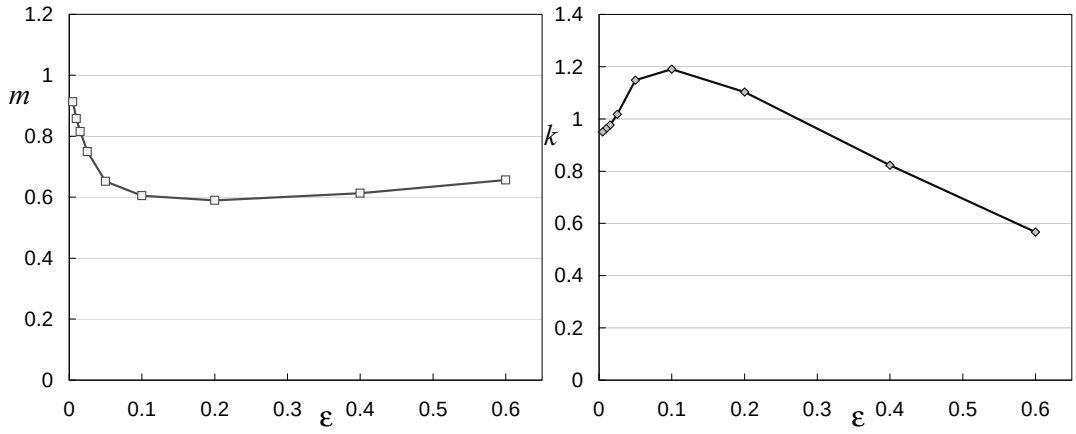

Figure 2.10: The coefficients m (left) and k (right) of equation 2.39 as function of the amplitude ratio ε.

Adapting their relationship to our notation, we find

$$\gamma = \frac{4}{\sqrt{3}}\chi^{1/2}. \tag{2.40}$$

Hence for strongly convergent estuaries the exponent of power law (2.39) reduces to $m = 0.5$.

In the present work the marginal conditions for tide amplification have been determined through numerical experiments and comparing the resulting tidal amplitude at a given section with that imposed at the mouth. An iterative algorithm has been developed in order to obtain, within a given tolerance, the value of the length L_b for which the difference was minimised. Simulations have been performed placing both a reflective barrier landward in a very long channel and the transparent condition, obtaining comparable results. More than 200 simulations have been conducted in a wide range of values of the parameters, namely $D_0 \in [2.5m \div 50m]$, $\varepsilon \in [0.005 \div 0.6]$, $C_h \in [10 \div 30]$, paying particular attention to the choice of typical conditions of real estuaries.

The marginal conditions obtained numerically are plotted in figure 2.9 in terms of the dimensionless ratio between friction and inertia χ and the degree of convergence γ, for different values of the amplitude ratio ε. Below the numerical points the wave is damped during its propagation landward, while above them it is amplified. It is worth noticing that the larger are the dissipative effects along the estuary (large χ), the stronger is the required degree of convergence to achieve the marginal conditions. On the contrary, a relatively weak variation of channel geometry can produce wave amplification in weakly dissipative estuaries.

From figure 2.9 it appears that numerical points corresponding to a given value of ε can be fitted fairly well through power law curves of the form (2.39), whose coefficients m and k only depend on the parameter ε. The above dependence embodies the effect of the finite amplitude of

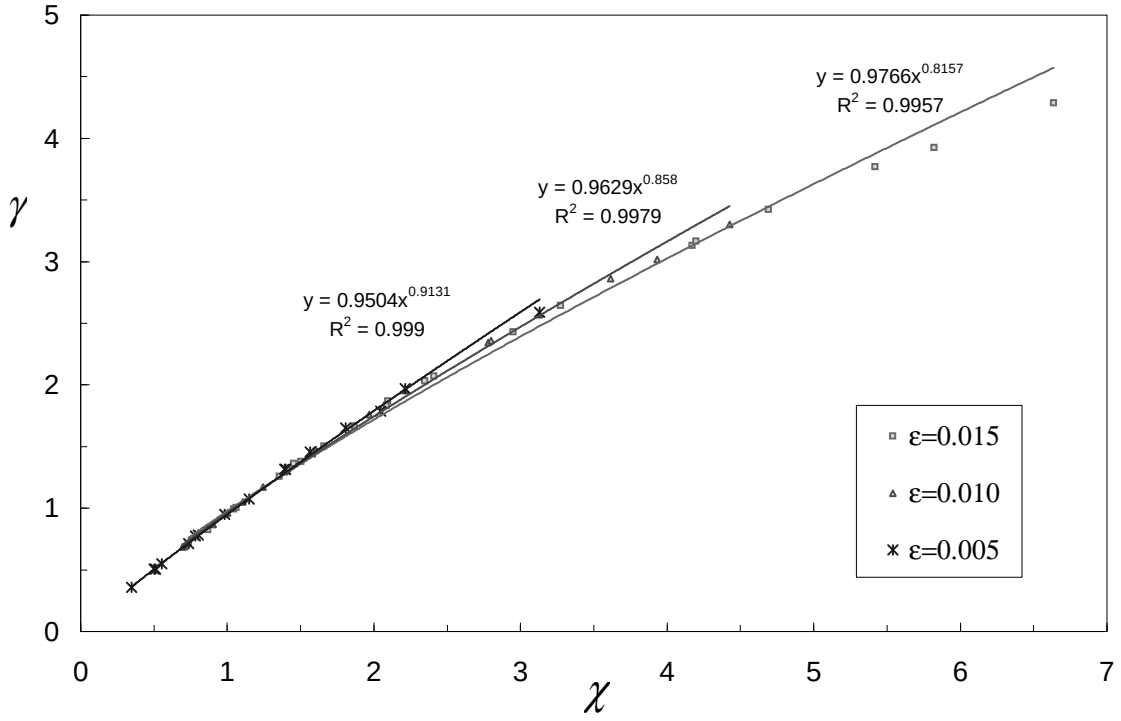

Figure 2.11: Marginal conditions for the amplification of tidal amplitude in the $\chi - \gamma$ plane, for different values of ε, as obtained through the numerical model. The interpolating power laws are reported in the plot with the corresponding correlation coefficient R^2.

the tidal wave on its amplification. The numerical findings are summarised in figure 2.10 where m and k are plotted as a function of ε: it is shown that the exponent m depends strongly on finite amplitude effects such that its value decreases sharply as ε increases and reaches an almost constant value, nearly equal to 0.6, for relatively large values of ε.

Numerical results for the weakly convergent and weakly dissipative case are represented in more detail in figure 2.11. As pointed out before, analytical results suggest that in this case a linear relationship should hold, with m=1. Numerical results conform to this behaviour only for very small values of ε. For commonly observed values of the tidal range within this class of estuaries the power law is non-linear. This is even clearer when considering that, as shown in figure 2.10, the tendency of m towards unity is almost vertical. Notice that the linear solution would be satisfactory in the case of an horizontal asymptotic trend of the curve towards m=1. Also notice that the landward boundary condition becomes more and more important in the numerical model as we approach the frictionless limit, hence when we consider very small values of χ and ε.

In the case of strong convergence a significant influence of the tidal amplitude on wave characteristics can be expected along with a substantial deviation from the linear behaviour. In this case

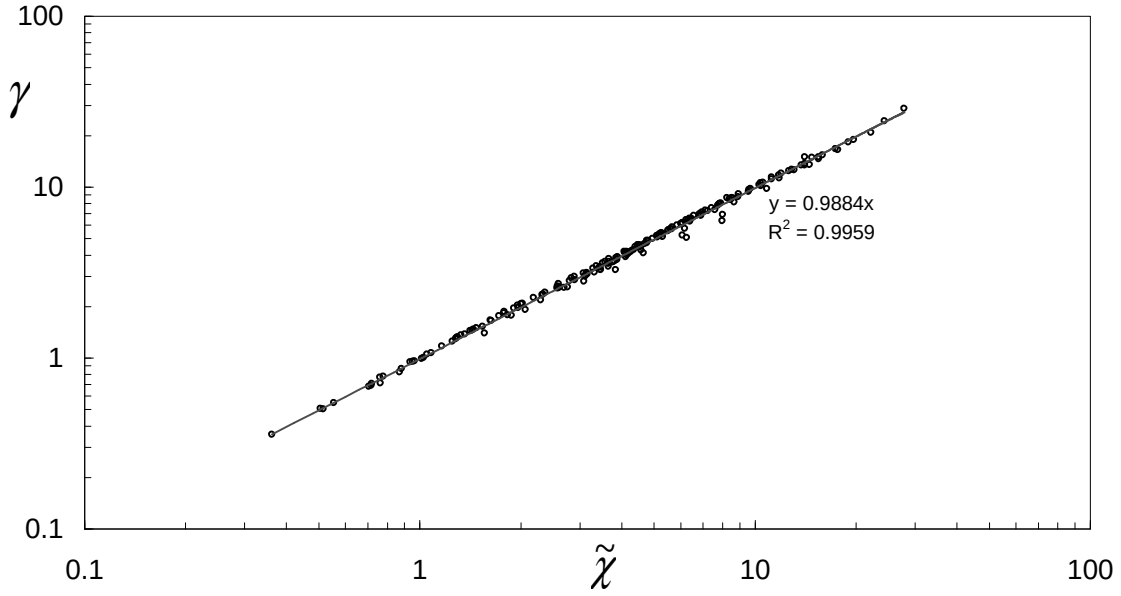

Figure 2.12: Marginal conditions in term of the modified dimensionless parameter $\tilde{\chi}$ defined in equation 2.41 The interpolating power law is reported with the corresponding correlation coefficient R^2.

the approximate analytical solution (see equation 2.40) leads to a value of the exponent m =0.5 which is fairly close to the numerical result ($m \simeq 0.6$) within a wide range of values of ε, namely those which are typically encountered in real estuaries according to the data reported in Table 1. Notice, however, that the coefficient $k \simeq 2.31$ of the relationship (2.40) does not fall within the range (0.6-1.2) obtained through numerical simulations and reported in figure 2.10.

It is worth noticing that if we introduce a modified parameter

$$\tilde{\chi}(\chi,\varepsilon) = k(\varepsilon)\chi^{m(\varepsilon)}, \tag{2.41}$$

using the values of the coefficients k and m given in figure 2.10, the numerical points which define the marginal conditions for tide amplification collapse on a single logarithmic plot as shown in figure 2.12.

3 Large scale equilibrium profiles in convergent estuaries

3.1 Long term equilibrium profiles in convergent estuaries

The morphodynamics of tidal channels has been investigated with increasing effort in the last years, both for the conceptual relevance of the subject and for various practical problems associated with human intervention in tidal systems like estuaries and lagoons.

At 'local' scale, say of the order of few channel widths, the recent analysis of Seminara and Tubino (2001) suggests that tidal bars can form through an instability mechanism, which is similar to that of river bars. At a large scale the evolution of these natural systems typically occurs on a fairly long time period, say of the order of centuries, and it is not easy to distinguish the "internal" morphological changes (i.e. those associated with the mutual interactions between the flow field and the bottom surface) from those related to the influence of the changing external conditions (sea level rise, subsidence, etc.). The long term erosional depositional processes in tidal channels are determined by the residual sediment transport, that is mainly related to the degree of asymmetry between the flood and the ebb peak values of flow velocity, which arises form the non-linear dependence of sediment transport on flow velocity. Typical values of velocity in tide dominated estuaries range between $1-3m/s$ enough to keep sediment in motion for most of the tidal cycle.

In this chapter the long-term evolution of the bottom profile of a convergent tidal channel is investigated. As pointed out in the preceding chapter, channel convergence may strongly affect the hydrodynamics of estuaries (see also Friedrichs and Aubrey, 1994 and Friedrichs et al., 1998). Its role on the morphological evolution of tidal channels, which was neglected in previous morphological analysis, (e.g. Schuttelaars and de Swart, 2000), has been recently highlighted by Lanzoni and Seminara (2002). In their work a classification of tidal channels is proposed, based on the relative role of the different mechanisms than control tidal hydrodynamics, as discussed in Chapter 2. However, the analysis of Lanzoni and Seminara (2002) is mainly oriented to characterise the behaviour of the solution in the asymptotic limits defined by the dominance of one of these effects; therefore, it is restricted to a limited number of situations and does not allow one to fully

recognize the role of the different parameters involved. The “intermediate” conditions in between the asymptotical behaviours, are the most common in natural systems.

In the present work we employ a one-dimensional model, starting from initially horizontal bed and neglecting the effect of intertidal areas. We will show how under these conditions the tidal channels are typically flood dominated in a large part of their length and the net flux of sediment is mainly directed landward. Due to the velocity asymmetry, a net upstream sediment flux is present for example in the Ord River estuary (Australia) (Wright et al., 1973), in the Salmon River estuary (Canada) (Dalrymple et al., 1990), and in the Severn estuary (UK) (Murray and Hawkins, 1977).

Results indicate that, when river discharge is not dominant and a reflective boundary is assigned at the landward end, a sediment front forms and slowly migrates landward until it leads to the emergence of a beach, which generally inhibits a further channel development. Hence, an inclined equilibrium bed profile is established, which is bounded by a beach at the landward end. This condition determines an asymptotic intrinsic length of the estuary. It is worth noticing that both in the present work and in previous analysis (Schuttelaars and de Swart, 2000; Lanzoni and Seminara, 2002) the resulting equilibrium bed profile shows an increasing bottom elevation in the landward direction. The above scenario is also confirmed by the experimental observations of Bolla Pittaluga et al. (2001). Also notice that the flow field over the equilibrium profile is characterised by symmetrical flood and ebb phases; therefore, the net sediment flux, averaged over a tidal cycle vanishes.

In present analysis we investigate in detail the dependence of such equilibrium length on the relevant physical parameters which characterise the tide and the channel geometry. Furthermore, we analyse the role of the seaward boundary condition for sediment transport on channel development.

Two different scenarios can be identified as the role of channel convergence increases.

1. in weakly convergent estuaries the equilibrium length coincides with the initial length of the channel, which is defined as the distance from the mouth to the landward boundary condition, where a reflective barrier is imposed;

2. when channel convergence is strong the landward beach may form within an internal section of the channel, provided that the landward boundary is located sufficiently far from the mouth. In this case the equilibrium length is shorter and mainly depends on the convergence length and on the mean channel depth.

In the former case the final length of the channel coincides with the initial imposed length, while in the latter case the equilibrium length is controlled by channel convergence. Another relevant result is that the equilibrium profile doesn’t depend appreciably on the type of boundary condition

for the sediment flux imposed at the mouth. In the perspective of the present results the analysis of Lanzoni and Seminara (2002) seems specially suitable to describe the case of relatively short estuaries.

3.2 Formulation of the problem and numerical scheme

The long term morphodynamic evolution of a tidal channel is investigated within the context of a one-dimensional framework whereby the standard de Saint-Venant equations (2.3a, 2.3b) are coupled with the sediment continuity equation, which reads:

$$B(1-p)\frac{\partial \eta}{\partial t}+\frac{\partial B q_s}{\partial x}=0, \tag{3.1}$$

where p is the sediment porosity and q_s is the total solid discharge per unit width. In the present analysis Engelund and Hansen formula is adopted which accounts for both bed and suspended load; in dimensional form it reads:

$$q_s=\sqrt{g\Delta D_s^3}0.05C_h^2\theta^{5/2} \tag{3.2}$$

where θ denotes the Shields stress

$$\theta=\frac{\tau}{(\rho_s-\rho)gD_s}=\frac{U^2/C_h^2}{g\Delta D_s}, \tag{3.3}$$

which is computed in terms of the local values of the bed shear stress τ or of the flow velocity $U=Q/\Omega$. In (3.3 and 3.2) ρ is water density, ρ_s and D_s are sediment density and diameter, respectively, and C_h is the dimensionless Chezy coefficient, $\Delta=(\rho_s-\rho)/\rho$ and g is the gravity acceleration.

Substituting from (3.1) into (2.3b) the set of governing equations can be cast in the following form:

$$\frac{\partial Q}{\partial t}+\frac{\partial}{\partial x}\left(\frac{Q^2}{\Omega}\right)+g\Omega\frac{\partial h}{\partial x}+\frac{Q|Q|}{\Omega C_h^2 R_h}=0, \tag{3.4a}$$

$$\frac{\partial h}{\partial t}+\frac{1}{B}\frac{\partial Q}{\partial x}+\frac{1}{(1-p)b}\frac{\partial q_s}{\partial x}=0 \tag{3.4b}$$

$$(1-p)\frac{\partial \eta}{\partial t}+\frac{1}{B}\frac{\partial b q_s}{\partial x}=0 \tag{3.4c}$$

The introduction of the continuity equation for the sediments doesn't change the mathematical nature of the system, in fact it is easy to show that system (3.4) is hyperbolic, like system (2.3); the number of eigenvalue in this case is three. The numerical scheme employed for the resolution

is similar to that discussed in Chapter 2 and consists in the MacCormak TVD algorithm in the form proposed by Garcia-Navarro et al. (1992).

3.3 Boundary conditions

In addition to the boundary conditions required to solve de Saint Venant equations, which are given in term of the free surface elevation at the mouth and the flow discharge at the upstream end, as discussed in Chapter 2, a further boundary condition is needed to solve the coupled system (3.4). At the landward end of the estuary a reflecting barrier is invariably assumed in the application of the morphological model; this implies that sediment flux vanishes at the landward end. At the mouth of the estuary, during the ebb phase an equilibrium sediment flux condition establishes, which means that the sediment flux outgoing from the estuary to the sea corresponds to the sediment load computed in terms of the local and instantaneous values of bed shear stress at the seaward end of the channel; as for the flood phase, we have tested the influence of two different boundary conditions: vanishing flux or equilibrium flux. We note that the definition of a suitable boundary condition for the sediment transport at a tidal inlet is still a debated question. A proper formulation would require a detailed analysis of the flow structure close to the inlet, which is beyond the scope of the present work. Notice however that the conditions adopted herein correspond to two extreme situations: in fact, the first condition reproduces the case in which the sediment input from the sea is negligible, while the second condition corresponds to a sediment supply from the sea which is able to compensate the transport capacity of the channelized flow at the inlet.

The MacCormak scheme consists of two steps, a prediction (forward finite differences) step and a correction step (backward finite differences). As pointed out in section 2.3 the number of boundary conditions needed by the numerical scheme is twice the number of physically based conditions. Hence, to include the solution of Exner equation (3.4c) in the numerical solution two additional conditions must be imposed, one at each boundary; as pointed out before, while at the mouth two different conditions have been tested, at the upstream end of the channel the vanishing sediment flux is imposed.

Also notice that during the numerical computation with mobile bed the deposition of sediment may induce bed aggradation whose thickness can growth until a beach is formed inside the channel. Under this condition part of the computational domain must be excluded from the computation. In fact, the governing equations (3.4) exhibit a singularity when the flow depth vanishes. To overcome the above difficulty the computational cells in which the flow depth is smaller than a given small value are excluded from the domain; on the contrary, cells are reintroduced in the computational domain when the rise of free surface occurring in the flood phase leads to new submerged areas.

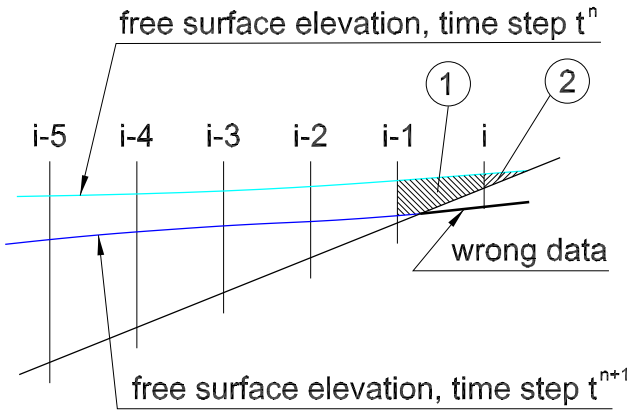

Figure 3.1: Boundary condition in the case of drying area.

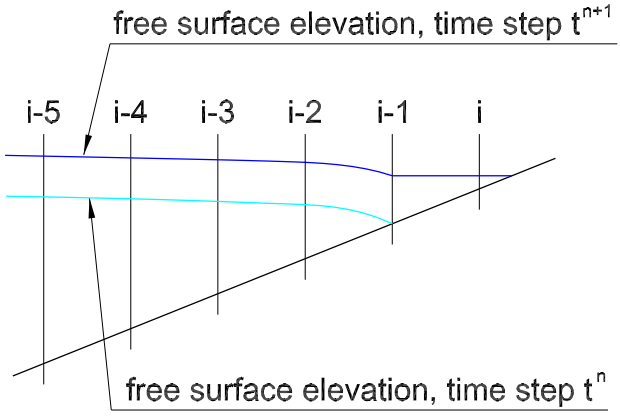

Figure 3.2: Boundary condition in the case of wetting area.

In order to consider wetting and drying areas the numerical algorithm has been modified in the following form.

- In the drying phase, when the free surface elevation is decreasing, the maximum flow discharge in every cell is evaluated through geometrical considerations. Let consider a situation like that represented in figure 3.1: in this case the value of the predicted free surface elevation, and then of flow discharge, is not compatible with the position of the bed profile. Hence, the maximum flow discharge in the cell i and $i-1$ is evaluated in term of the volume of water (volumes 1 and 2 for the cell i and $i-1$, respectively) stored between two consecutive sections, divided by the time step of the computation. A similar procedure is adopted for the adjacent cells. If the numerical algorithm evaluates a flow discharge smaller than the maximum value previously defined, the numerical result is kept as the correct value: under this condition the depth doesn't vanishes, as in the case of sections from $i-5$ to $i-2$ in figure 3.1. On the other hand, when the numerical scheme evaluates a discharge greater than the maximum discharge, the latter value is taken as the right one and the free surface elevation is imposed equal to the bottom elevation (sections i and $i-1$ in figure 3.1).

- In the wetting phase the cells is reintroduced in the computational domain when the free surface elevation, which is assumed horizontal beyond the last active cell (see figure 3.2), is larger than the bed elevation. The flow discharge in the new submerged cell is evaluated through geometrical considerations.

We may notice that this approximated procedure requires relatively small values of the Courant number (nearly equal to 0.5) in order to preserve the stability of the scheme. Also notice that the above procedure allows one to satisfy the continuity equation within the domain subject to wetting and drying, while the momentum equation is not solved therein.

3.4 Bottom equilibrium profiles

The morphodynamic evolution of a tide dominated convergent estuary is investigated solving the flow field and the sediment continuity equation over several tidal cycles, until the equilibrium configuration is reached. Once the equilibrium is achieved the bed profile induces a symmetrical flow field, such that the sediment flux averaged over a tidal cycle vanishes. The numerical simulation of the above process requires a large amount of computational time. In fact, the time step must be kept small with respect to the tidal period, which in turn is much smaller than the characteristic time scale of the bed evolution. An estimation of the latter scale can be given in the following

form:

$$T_{bed} = \frac{(1-p)U_0 L_0}{\sqrt{g\Delta D_s^3}}, \tag{3.5}$$

where U_0 and L_0 are suitable scales for the velocity and the length of the estuary, respectively (see discussion in Chapter 2). For reasonable choice of parameters ($U_0 \sim 1-2ms^{-1}, L_0 \sim 10-100km, D_s^* = 0.1-0.2mm$) we obtain that T_{bed} ranges between $10-500$ years!

According to the results of numerical simulations the morphological evolution of a tidal channel can be described as follows. Starting from an initial horizontal bed profile a sediment front is formed where the divergence of the sediment flux is larger and negative. The front migrates landward and amplifies until it reaches the last section, where it may be reflected. For values of the relevant parameters which are typical of real estuaries, after a fairly long period of time, say of the order of hundreds of years, the system tends to an equilibrium configuration, which is characterised by a bottom profile displaying an upward concavity, as also found by Lanzoni and Seminara (2002). As shown in figure 3.3, the morphological evolution of the channel may follow two different behaviours, depending upon the role of the physical constraint which is posed by the finite length of the estuary (notice that in both cases the channel is convergent).

Results reported in figure 3.3a correspond to a relatively short estuary. In this case the asymptotic configuration is characterised by the formation of a beach at the landward end, such that the final length coincides with the imposed length of the estuary L_e. This is the case treated by Lanzoni and Seminara (2002). In longer channels (figure 3.3b) the sediment front, which migrates landward, may stop at a certain distance from the mouth because a beach is formed inside the channel. This condition generally prevents the further development of the channel. In this case the equilibrium bottom profile establishes within a fraction of the total length of the estuary. Hence, for given values of the relevant parameters an equilibrium length of the estuary L_a can be defined, which is achieved provided that the landward boundary condition is located sufficiently far from the mouth. Notice that results presented herein refer to relatively large values of ε and hence of solid discharge q_s, which implies a much faster evolution of the system.

In figure 3.4 the effect of the seaward boundary condition for the sediment transport is investigated. Bed profiles, evaluated through the condition of vanishing inflow of sediment at the mouth of the estuary, are plotted with dashed lines, while continuous lines denote results obtained with sediment influx from the sea equal to the transport capacity computed according to the local and instantaneous flow conditions at the mouth. We may notice that the former condition implies a larger scour at the mouth, whose effect on the equilibrium solution depends on the initial length of the estuary: in short channels, where the equilibrium bottom profile extends over the whole estuary, a larger scour at the mouth leads to a slight increase of the equilibrium slope; in long channels, where the asymptotic length L_a can be achieved, the slope is roughly constant and the

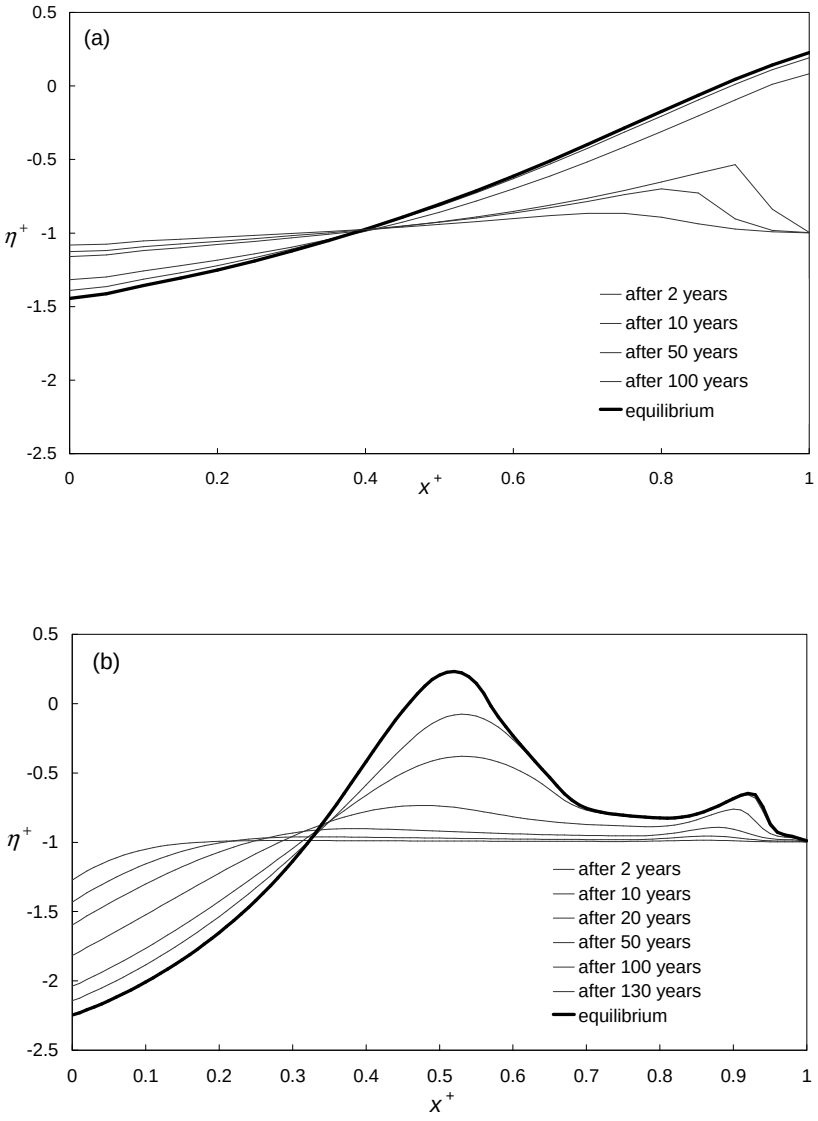

Figure 3.3: The long term evolution of the bottom profile of a convergent estuary for different values of channel length. $L_b = 120km$, $D_0 = 10m$, $a_0 = 4m$, $C_h = 20$, $D_s = 10^{-1}mm$; $L_e = 160km$ (a), $L_e = 480km$ (b). The longitudinal coordinate x^+ is scaled with the length L_e, the bottom elevation η^+ is scaled with the reference depth D_0.

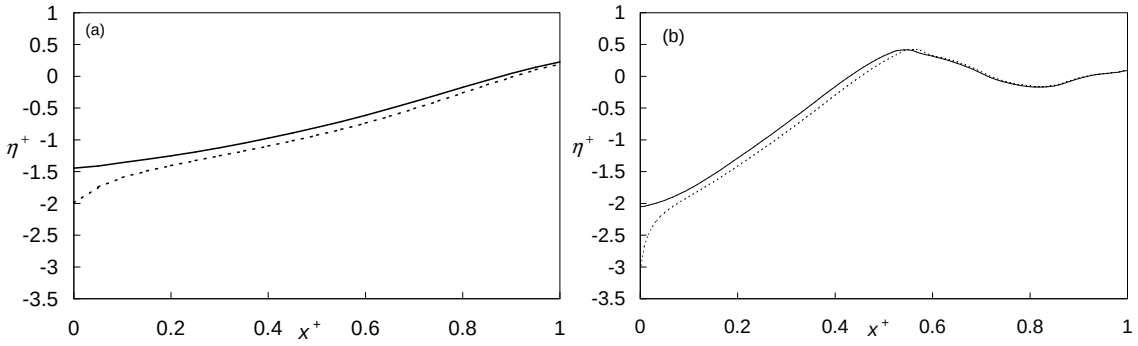

Figure 3.4: The equilibrium bottom profiles in "short" (a) and "long" (b) channels with different boundary conditions at the mouth of the tidal channel: vanishing sediment flux (dashed lines) and equilibrium sediment flux (solid lines). $D_0 = 10m$, $a_0 = 4m$, $C_h = 20$, $D_s = 10^{-1}mm$; $L_e = 160km$, $L_b = 120km$ (a); $L_e = 280km$, $L_e = 40km$ (b). The longitudinal coordinate x^+ is scaled with the length L_e, the bottom elevation η^+ is scaled with the reference depth D_0.

equilibrium beach slightly migrates landward.

It is worth noticing that the longitudinal location of the sediment front in the channel depends strongly on the degree of convergence, inasmuch as the hydrodynamic behaviour of the system is influenced by this factor. Also notice that the non-symmetric (flood-dominated) character of many estuaries is driven toward a more symmetrical configuration when the bottom profiles increases its slope (Friedrichs and Aubrey, 1994; Toffolon, 2002). Recalling that sediment transport mainly depends on flow velocity through an exponent larger than 1, it is possible to relate the residual sediment transport to the peak values of velocity during the ebb and flood phases; for this purpose it is convenient to define the degree of asymmetry as follows :

$$\alpha = log \frac{|U_{flood\,max}|}{|U_{ebb\,max}|}. \tag{3.6}$$

The influence of the degree of convergence on sediment transport, and hence on the morphological evolution, is shown in figure 3.5, where characteristic values of both velocity U and sediment flux q_s are plotted at the initial stage of evolution (horizontal bed). We note that the asymmetry exhibited by the peak values of velocity, which is related to the residual sediment flux, may induce a different behaviour depending upon the degree of convergence of the estuary. In weakly convergent estuaries, the asymmetry decreases almost monotonically in the landward direction and the sediment front starts to form close to the landward boundary. On the other hand, when the degree of convergence increases, a maximum of velocity and residual transport occurs inside the channel, which determines there a larger sediment flux gradient; as a consequence the sediment

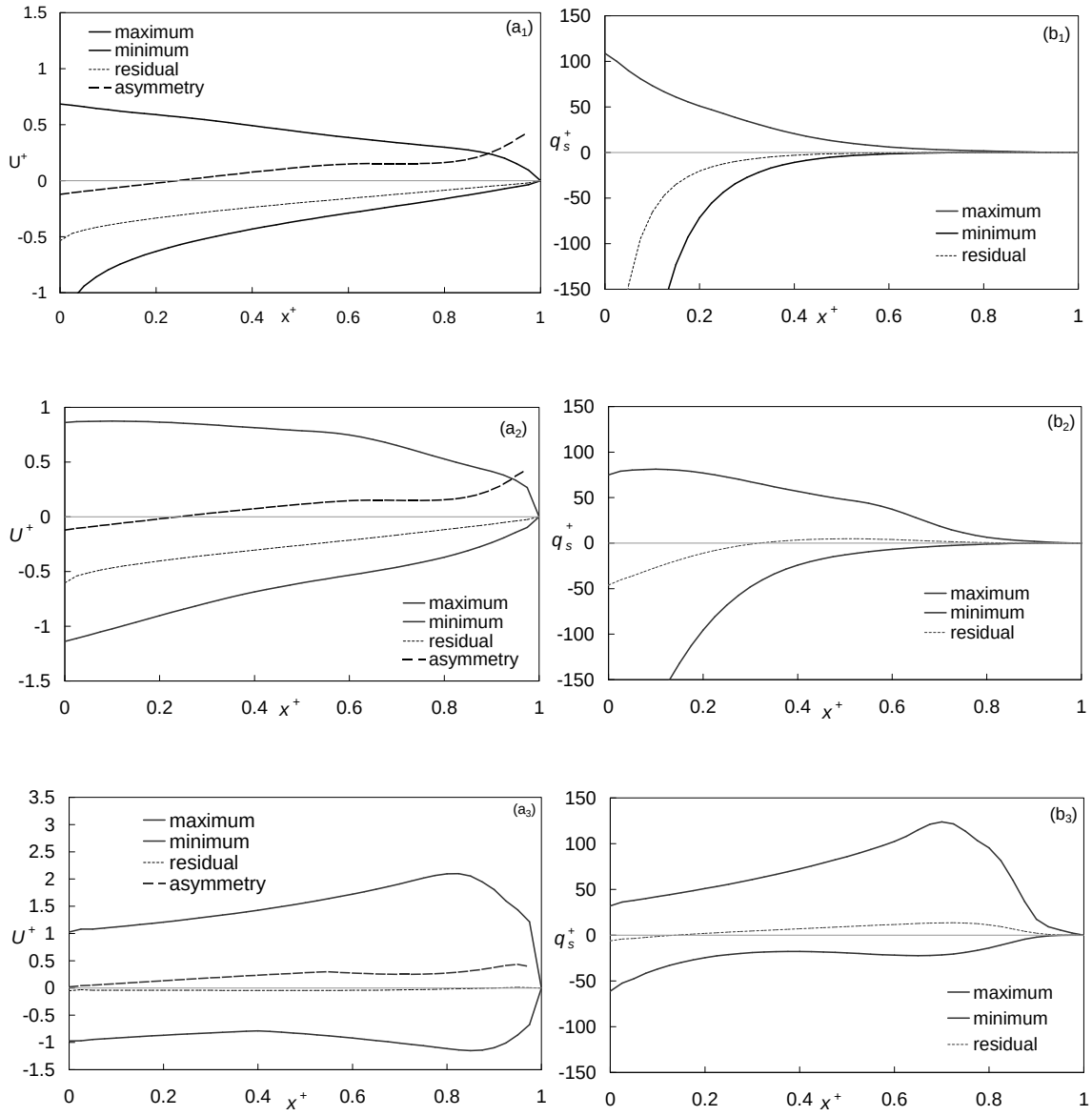

Figure 3.5: Degree of asymmetry, maximum, minimum and residual values of flow velocity (a), normalised with the average of its peaks at the mouth, and of sediment flux (b), normalised with $\sqrt{g\Delta D_s^3}$, along the estuary, the longitudinal coordinate x^+ is scaled with L_e. $L_e = 160km$, $D_0 = 10m$, $a_0 = 4m$, $C_h = 20$, $d_s = 10^{-1}mm$; different values of convergence length: $L_b \to \infty$, (a_1, b_1), $L_b = 160km$, (a_2, b_2), $L_b = 10km$, (a_3, b_3).

front develops in an internal section of the channel.

It is worth noticing that in the numerical simulations we impose an impermeable barrier at the landward end of the estuary; hence, the equilibrium configuration requires that the net sediment flux vanishes everywhere. In fact, when the tidally averaged asymptotic condition is achieved and the mean bed level keeps constant, the sediment continuity equation (3.1), written in terms of the residual sediment transport recalling also the (2.5), reads:

$$\frac{\partial \langle q_s \rangle}{\partial x} + \frac{\langle q_s \rangle}{L_b} = 0 \tag{3.7}$$

where the square brackets denote tidal average. With the imposed boundary condition at the landward end, equation (3.7) only admits of the solution $\langle q_s \rangle = 0$. In figure 3.6 we plot the maximum, minimum and residual values of flow velocity U as a function of the landward coordinate, as obtained at the beginning of the simulation (when the bed is horizontal) and at equilibrium, for different boundary conditions at the mouth of the estuary. We note that at equilibrium the peak value of velocity keeps almost constant along the whole estuary, as it is commonly observed in real estuaries. A similar plot is given in figure 3.7 in terms of the sediment flux. It is interesting to note that the equilibrium conditions asymptotically reached by the system are dynamical, since they are achieved only in terms of net transport. Results reported in figure 3.7 also clarify the influence of the seaward boundary condition for sediment transport. When sediment inflow is set equal to zero, sediment transport must vanish at the mouth in order to reach a stable configuration. This implies a larger scour at the entrance and hence a smaller velocity. On the contrary, when sediment inflow balances the equilibrium transport capacity associated with the local hydrodynamic conditions, the sediment transport can maintain a non-vanishing peak value even at equilibrium.

Results of numerical simulations concerning the equilibrium length of the estuary are summarised in figure 3.8 in dimensional form, in terms of the initial length L_e, i.e. the distance from the mouth of the landward boundary, and the convergence length L_b. The final length L_a is defined as the distance between the mouth and the beach, at equilibrium. As pointed out before, when the channel is not sufficiently long, that is for small values of L_e, the equilibrium length L_a coincides with the physical dimension imposed to the system: the corresponding points fall on the bisector line of the graph. On the contrary, when the channel is long enough the system can reach an equilibrium length which depends on the degree of convergence of the channel: the stronger is channel convergence (i.e. small values of L_b), the shorter is the equilibrium length L_a. Numerical results also suggest that a transition zone occurs close to the bisector line, in which L_a still depends on the initial physical dimension, beyond which an asymptotic value of the equilibrium length is reached, for a given value of L_b. Hence, we can define this asymptotic length as the convergence-induced equilibrium length L_c. Notice that the width of the transition zone increases as the convergence

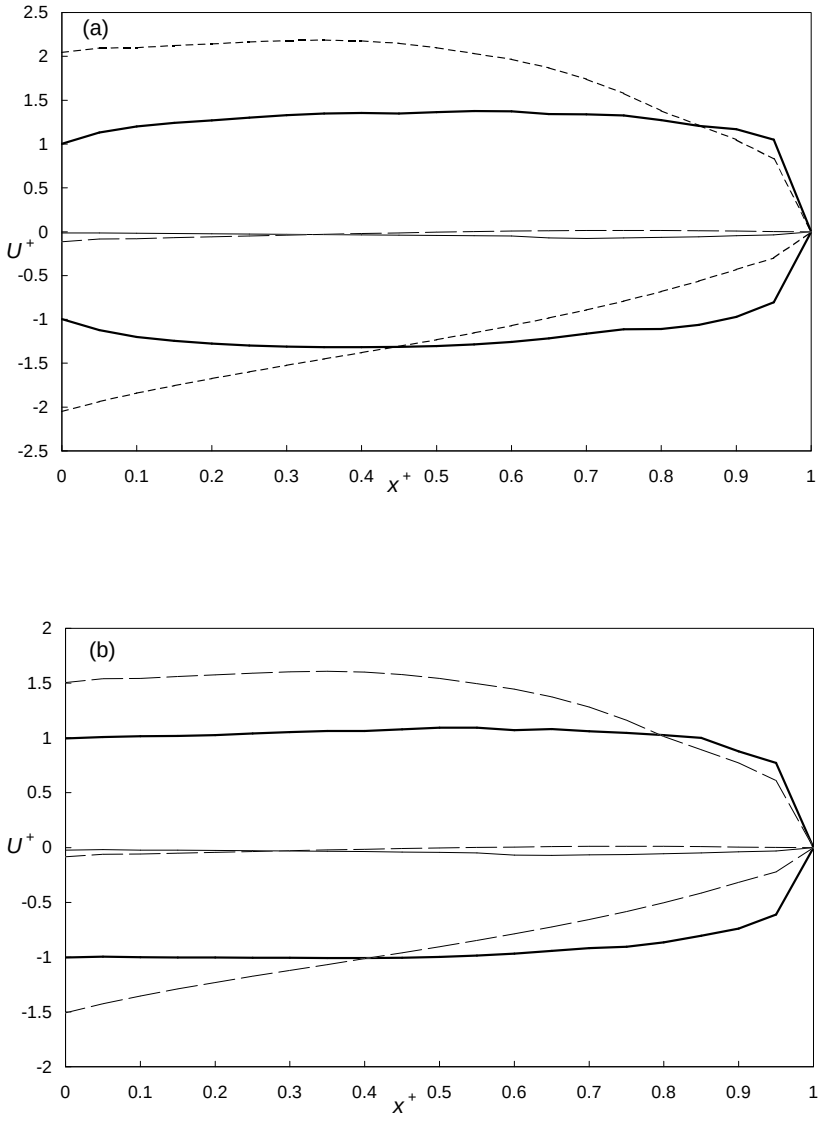

Figure 3.6: Maximum, minimum and residual values of flow velocity U^+, along the estuary after one cycle (dashed line) and at equilibrium (continuous line), for different boundary conditions at the seaward and: (a) vanishing sediment flux; (b) equilibrium sediment flux. $L_e = 40km$, $L_b = 20km$, $D_0 = 5m$, $a_0 = 2m$, $C_h = 20$, $d_s = 10^{-1}mm$; the velocity U^+ is normalized with the maximum value at the mouth at equilibrium and the longitudinal coordinate x^+ is scaled with L_e.

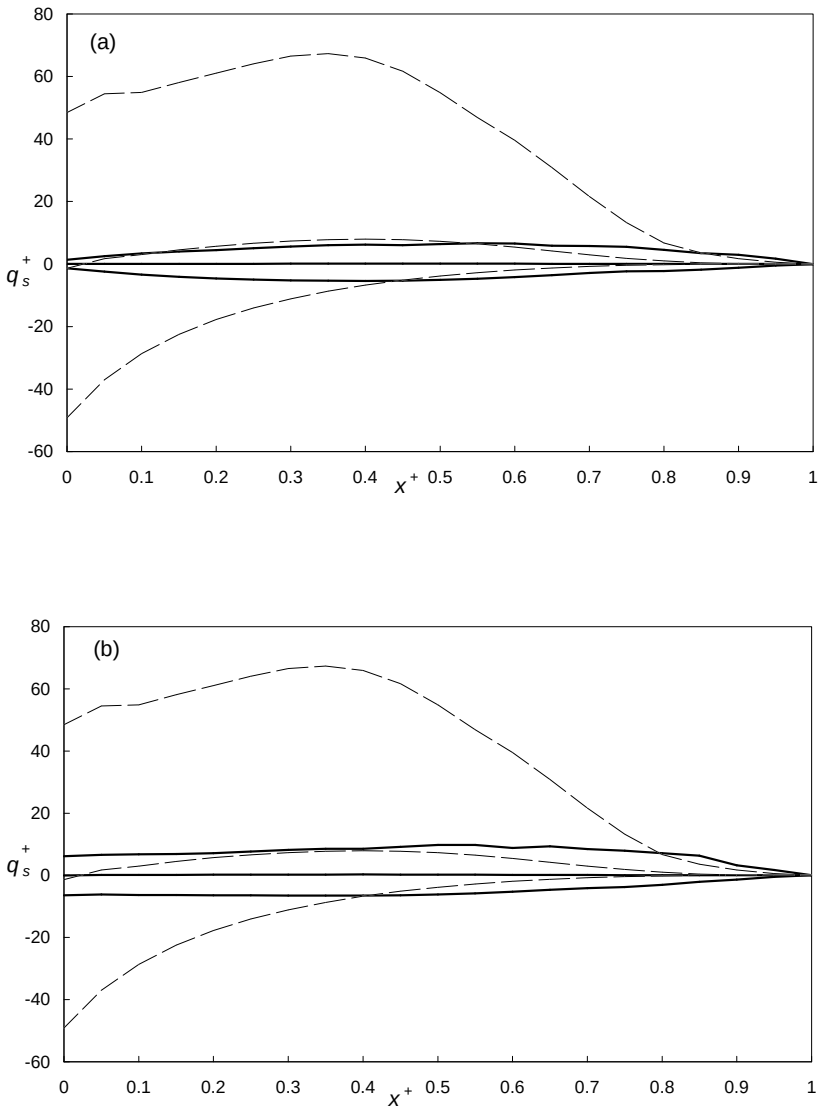

Figure 3.7: Maximum, minimum and residual sediment flux q_s^+ scaled with $\sqrt{g\Delta D_s^3}$ along the estuary after one tidal cycle (dashed line) and at equilibrium (continuous line), for different boundary conditions at the seaward end: (a) vanishing sediment flux; (b) equilibrium sediment flux. Data as in figure 3.6. The longitudinal coordinate x^+ is scaled with L_e.

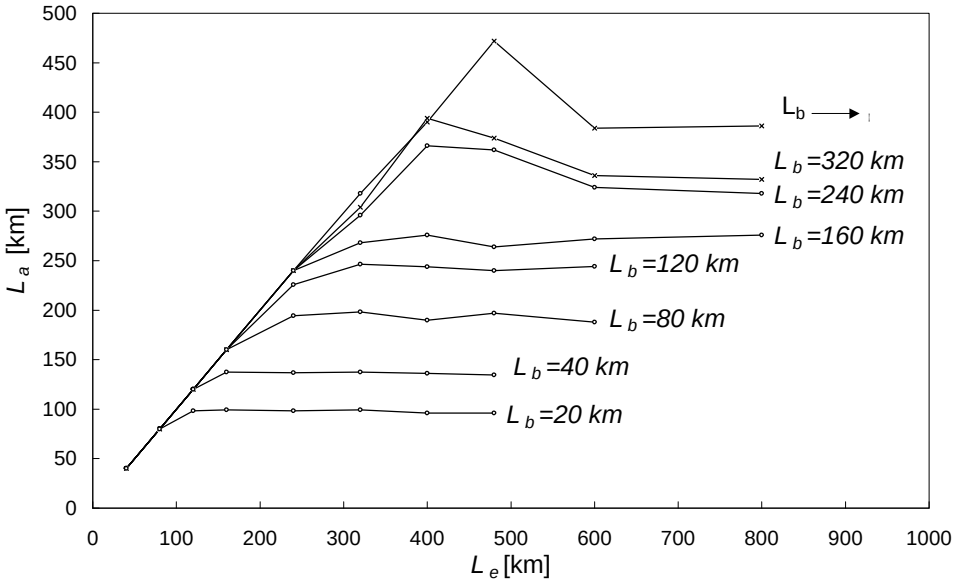

Figure 3.8: Equilibrium length of the estuary L_a as a function of the initial length L_e, for different values of convergence length. $D_0 = 10m$, $a_0 = 4m$, $C_h = 20$, $d_s = 10^{-1}mm$.

length increases.

The convergence-induced equilibrium length also depends on the initial depth D_0. In fact, when the initial depth is large, a longer reach is required to let the beach to emerge. However, the above dependence can be ruled out once the equilibrium length L_c is scaled with the initial depth D_0, as shown in figure 3.9. Also notice that in weakly convergent channels or in constant width channels the beach does not always emerge. However, a suitable equilibrium length can be defined also in this case in terms of the distance from the mouth of the leading edge of bottom profile (the corresponding points are denoted by 'x' in figure 3.8).

3.5 Discussion

In this chapter we have investigated the long-term morphological evolution of estuarine channels through a relatively simple one-dimensional numerical model.

The final equilibrium profile is the natural response of the system to the external forcing effects due to tide propagation and channel convergence. After a long period of time, say of the order of the centuries, an equilibrium configuration is achieved, which displays the presence of a beach at the end of the channel or inside the estuary, depending upon the length and the degree of convergence.

The channel convergence can be considered as a forcing term, as in the fluvial case, where

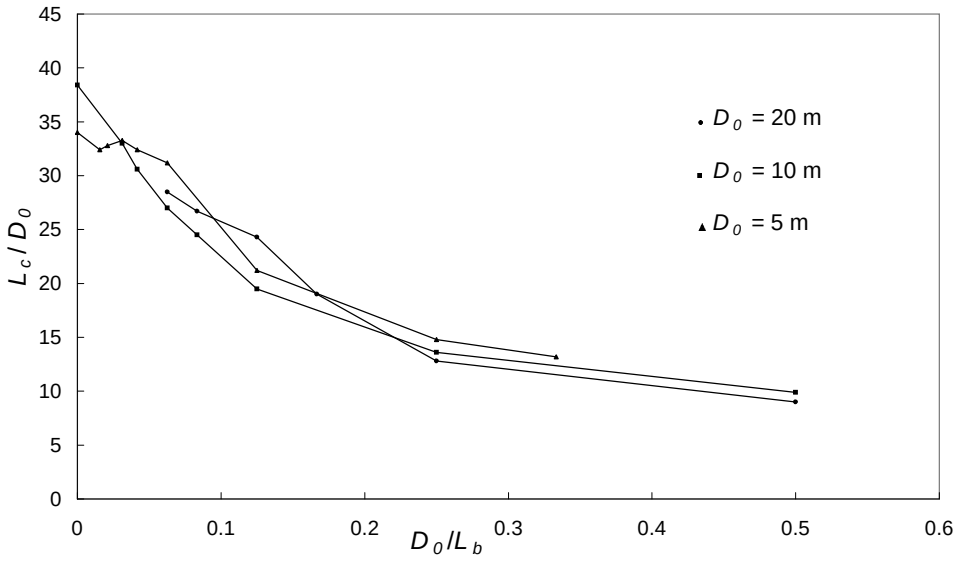

Figure 3.9: Dimensionless equilibrium length L_c/D_0 as a function of the dimensionless degree of convergence D_0/L_b, for different values of D_0. $\varepsilon = 0.4$, $C_h = 20$, $d_s = 10^{-1}mm$.

width variations can induce the development of bed forms. In the case of tidal channels, the convergence, which exerts an important effect on the hydrodynamics (see Chapter 2), also plays a significant role on bed evolution, increasing the ability of the tidal flow to form deposits inside the channel.

In the case of a short channel the behaviour of the bottom profile is the following: a flux of sediment takes place inside the channel, because in tide dominated estuaries the hydrodynamics is generally flood dominated, which induces a landward transport of sediment. At the landward end of the channel a reflective boundary condition is imposed; hence, the flow discharge and the sediment flux vanish. Due to the decrease of sediment discharge close to the landward end, its gradient may attain high values and a sediment front is formed. Then, the front tends to migrate landward, until the final section is reached and a beach at the end of the estuary establishes.

In long convergent channels the beach forms within an internal section, because as the length of the channel increases the maximum gradient of solid discharge moves away from the landward end. From figure 3.3b we may note that close to the channel end a smaller secondary front is still present due to the effect of the vanishing flux condition.

The equilibrium configuration has been defined as the condition in which the tidally averaged sediment flux vanishes or, alternatively, the bottom elevation attains a constant value. The dynamic equilibrium achieved by the channel is characterised by negligible residual values of the sediment transport and almost constant values of the velocity along the estuary. As described above, the

final equilibrium length of the channel is found to depend mainly on two parameters, namely the physical length of the channel and the degree of convergence. In particular, for relatively short and weakly convergent estuaries, a beach is formed at the landward end of the channel and the equilibrium length coincides with the initial length of the channel, that is the distance of the landward boundary from the mouth. When the initial length of the channel exceeds a threshold value, which decreases for increasing values of the degree of convergence of the channel, the beach forms within an internal section of the estuary and the final equilibrium length is much shorter and mainly governed by the convergence length.

Present results also suggest that imposing the condition of vanishing sediment input flux from the outer sea during the flood phase determines a larger scour in the seaward part of the estuary, though the overall longitudinal bottom profile does not differ much from which one obtained with the alternative boundary condition of sediment influx equal to the equilibrium transport capacity of the channelized flow at the mouth.

Numerical results are in fairly good agreement with the experimental observations of Bolla Pittaluga et al. (2001) and Bolla Pittaluga (2002), which refer to a laboratory flume, $30\,cm$ wide and $24\,m$ long, with constant width. In fact, the experimental runs lead to equilibrium profiles which are similar to those predicted by the present model, displaying a landward slope, an upward concavity and a beach at the landward end. Furthermore, the maximum scour at the mouth is nearly equal to the mean flow depth.

Finally, it is worth noticing that several factors have been neglected, which may play an important role in the morphological evolution of tidal channels. In particular, the input of fresh water and sediment discharge at the landward boundary is not considered. One may argue that the above effect is likely to counteract the formation of emerged areas and, consequently, it may affect both the length and the structure of the final bottom configuration. However, the slope of the equilibrium profile seems to be mainly determined by the hydrodynamic behaviour of the estuary and by the tendency of the system to minimise the asymmetry between the flood and the ebb phases; hence, we expect that within the seaward part of the estuary results are not likely to change, at least qualitatively, also in the presence of river discharge.

4 Local-scale model for tidal channels

As pointed out in Chapter 1, the morphodynamic equilibrium of tidal channels, as well as that of rivers, can be investigated at different scales. In this chapter we focus the attention to the meso-scale; more specifically we investigate the instability process which leads to the formation of free bars in systems characterised by fine sediments, like tidal channels or the lower reaches of alluvial rivers. The mechanisms of erosion and deposition associated with meso-scale feature like estuarine bars often determine complex pathways of sediment transport, such that some channels may be dominated by ebb transport and other by flood transport.

A "local" analysis is performed, which implies that we restrict our attention to a conveniently short reach of the channel, whose length is of the order of few tens of channel widths. To characterise adequately the suspended sediment transport a three dimensional model for the flow and the concentration field is adopted, coupled with an evolution equation for the bed topography. Further discussion on the suitability of the three dimensional approach with respect to the much simpler two-dimensional model is also contained in Chapter 7.

4.1 Formulation of the problem

We consider a straight channel with vertical banks, characterised by a cohesionless bed and constant width $2B^*$. We refer the flow field, the concentration field and bed topography to an orthogonal co-ordinate system, where x^* is the longitudinal co-ordinate of the channel, y^* is the transversal co-ordinate, and z^* the vertical co-ordinate pointing upwards (hereinafter an asterisk as superscript denotes dimensional quantities).

The following notation is adopted: (u^*, v^*, w^*) is the velocity vector, η^* and h^* denote the local values of bed and free surface elevation, respectively, $D^* = h^* - \eta^*$ is the local flow depth, C the volumetric concentration of suspended sediment and t^* is time (figure 4.1).

The dimensional variables are made dimensionless adopting suitable scales for the study of meso-scale bed-forms, whose planimetric dimension is comparable with the channel width. In particular, we use:

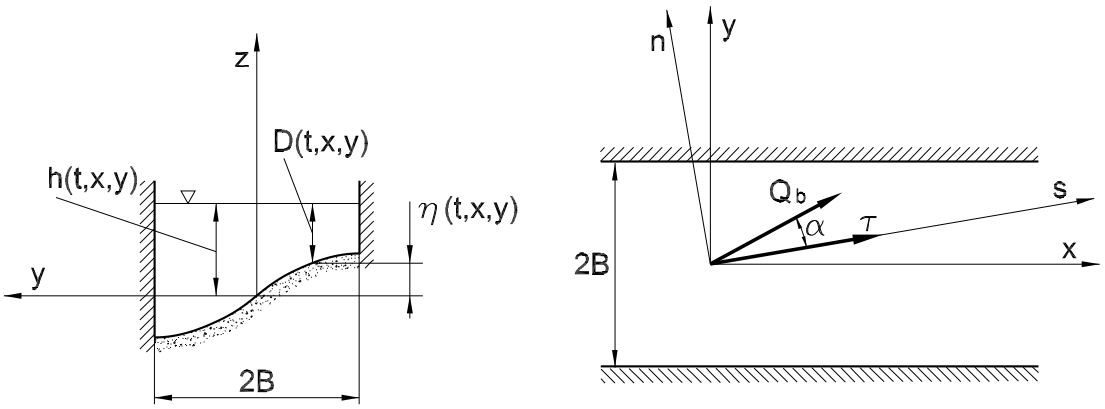

Figure 4.1: Sketch of the channel and notation.

- the channel half width B^* to scale the planimetric coordinates x^* and y^*;
- a reference flow depth D_0^* to scale the vertical coordinate z^*, the local free surface elevation h^*, bed elevation η^* and flow depth D^*;
- a reference flow velocity U_0^* to scale the velocity components.

Furthermore, a characteristic time scale $T_0^* = B^*/U_0^*$ is introduced. Hence, we write:

$$(x,y) = \frac{(x^*,y^*)}{B^*} \tag{4.1a}$$

$$(z,\eta,h,D) = \frac{(z^*,\eta^*,h^*,D^*)}{D_0^*} \tag{4.1b}$$

$$(u,v,w) = \frac{(u,v,w)}{U_0^*} \tag{4.1c}$$

$$t = \frac{t^*}{T_0^*} \tag{4.1d}$$

The reference values U_0^* and D_0^* can be readily defined in the river case as the depth averaged velocity and depth of the uniform flow, for given discharge, bed slope and sediment size. In dimensionless form such reference state is completely determined once the following dimensionless parameters are given:

$$\beta = \frac{B^*}{D_0^*}, \tag{4.2a}$$

$$D_s = \frac{D_s^*}{D_0^*}, \tag{4.2b}$$

$$\theta_0 = \frac{U_0^{*2} C_{f0}}{\Delta g D_s^*}, \tag{4.2c}$$

$$R_p = \frac{\sqrt{\Delta g D_s^3}}{\nu}, \tag{4.2d}$$

where D_s^* is sediment diameter, Δ is the relative density of sediment, ν is the cinematic viscosity of fresh water, g is gravitational acceleration and C_{f0} is the friction coefficient of the reference uniform flow.

For tidal channels the reference state can not be identified simply as in the river case. In particular, as discussed in Chapter 2 the velocity scale in a tidal channel is not an external variable and depends on the relative importance of the main ingredients, which control the propagation of a tidal wave, namely inertia, friction and degree of convergence of the channel. Furthermore, it also depends on the landward boundary condition. The reference state can be defined using for example the velocity scale proposed by Toffolon (2002) and a tidally averaged value for the flow depth. In the simplified approach introduced by Seminara and Tubino (2001), which mainly apply to tidal channels like the main channels of Venice lagoon, a reference state is defined assuming a sinusoidal oscillation for the flow velocity and keeping constant depth during the tidal cycle.

The flow field and the concentration field in a tidal channel are investigated here within the framework of a three dimensional model where the standard shallow water approximation is adopted. The hydrostatic approximation is justified provided the channels is wide enough and the tidal wavelength largely exceeds the flow depth, as generally occurs in tidal systems. Notice that in strongly convergent estuaries, like for example the Araguari river or the Gironde estuary, the tidal wave can break during its propagation and form shock wave, which cannot be studied within the context of the shallow water approximation. However, this phenomenon affects only locally the morphodynamic behaviour, since it is confined within a short length of the channel and lasts for a relatively short time.

In dimensionless form, and keeping only the significant turbulent fluxes, the Reynolds equations, the flow continuity equation and the transport equation for the suspended sediment read:

$$u_{,t} + uu_{,x} + vu_{,y} + \beta w u_{,z} - \gamma(\nu_T u_{,z})_{,z} + \frac{h_{,x}}{F_o^2} - \frac{i_F}{F_0^2} = 0, \tag{4.3a}$$

$$v_{,t} + uv_{,x} + vv_{,y} + \beta w v_{,z} - \gamma(\nu_T v_{,z})_{,z} + \frac{h_{,y}}{F_o^2} = 0, \tag{4.3b}$$

$$u_{,x} + v_{,y} + \beta w_{,z} = 0, \tag{4.3c}$$

$$C_{,t} + (uC)_{,x} + (vC)_{,y} + \beta\left[(w - W_s)C\right]_{,z} + \\ -\gamma(\Psi_T C_{,z})_{,z} = 0, \tag{4.3d}$$

where (u,v,w) denote the three-dimensional velocity field, C is the volumetric concentration of suspended particles, $\gamma = \beta\sqrt{C_{f0}}$, W_s is particle fall velocity, scaled with U_0^*, and F_0 is the Froude number of the reference flow. Furthermore, the subscripts $(,t)$, $(,x)$,$(,y)$,$(,z)$ denote partial derivative with respect to t, x, y and z, respectively, and i_F is the mean bed slope in the longitudinal direction.

Closure assumptions for the eddy viscosity ν_T and diffusivity Ψ_T are introduced assuming that the slowing varying character of the flow field both in space and in time leads to a sequence of equilibrium states. Therefore we employ a self-similar structure for ν_T and Ψ_T, written in term of a boundary fitted coordinate:

$$\xi = \frac{z - \eta}{D}. \tag{4.4}$$

Furthermore, the scales of the eddy viscosity ν_T and diffusivity Ψ_T are given in term of the local and instantaneous values of flow depth and shear velocity. Hence, we write:

$$\nu_T = \frac{\nu_T^*}{\sqrt{C_{f0}}U_0^* D_0^*} = u_* D N(\xi), \tag{4.5}$$

$$\Psi_T = \frac{\Psi_T^*}{\sqrt{C_{f0}}U_0^* D_0^*} = u_* D P(\xi), \tag{4.6}$$

where ν_T^* and Ψ_T^* are the dimensional values of eddy viscosity and diffusivity and u_* is the shear velocity scaled with $\sqrt{C_{f0}}U_0^*$

$$u_* = \frac{1}{\sqrt{C_{f0}}U_0^*}\sqrt{\frac{|\tau^*|}{\rho}}, \tag{4.7}$$

τ^* is the dimensional bed shear stress and $N(\xi)$ and $P(\xi)$ are the vertical distributions of ν_T and Ψ_T at equilibrium, for which the relationships proposed by Dean (1974) and McTigue (1981) are employed. They read:

$$N(\xi) = \frac{K_v \xi (1-\xi)}{1 + 2A\xi^2 + 3B\xi^3}, \tag{4.8}$$

$$P(\xi) = \begin{cases} 0.35\xi & \text{if} \quad \xi < 0.314 \\ 0.11 & \text{if} \quad \xi \geq 0.314 \end{cases} \tag{4.9}$$

where $A = 1.84$, $B = -1.56$ and $K_v = 0.4$ is the von Karman constant.

Sediments in fluvial and tidal channels are transported as bed load and suspended load. Usually the former mechanism is assumed to be confined in a thin layer close to the bed (the bed layer) and it is evaluated as a direct function of the bed shear stress. Suspended load occurs in the

upper part of the water layer (i.e. over the reference level sketched in figure 4.2), where value of sediment concentration depends on advective and diffusive effects. The main distinctive feature of suspended load, with respect to bed load, is the non-instantaneous response to flow variations, since it requires a relatively large adaptation length to achieve local equilibrium with changing hydraulic conditions. The advection-diffusion equation (4.3d), in which sediments are considered as passive tracers except for their tendency to settle, is the differential equation that reproduces this delay. The net sediment exchange between the two layers is due to turbulent and settling effects, as shown in figure 4.2. The suitability of this approach requires small values of sediment concentration and Richardson number, and a particle grain size much smaller than turbulent length scales. Close to the bottom, where sediment concentration attains larger values due to settling effect, these condition are only approximately satisfied.

The formulation of the problem is completed through the introduction of the continuity equation for the sediments which describes the development of bottom topography; considering the bed load fluxes and also the net sediment flux through the reference level, the mass balance for sediments reads:

$$\begin{aligned}(1-p)\,\eta_{,t} + Q_0\,(Q_{bx,x} + Q_{by,y}) + \\ +\beta\left[\hat{\mathbf{k}} W_s\,(C - C_e)\cdot\hat{\mathbf{n}}\right]_{\xi=a} = 0,\end{aligned} \tag{4.10}$$

where p is sediment porosity, (Q_{bx}, Q_{by}) is bed-load vector, scaled with $\sqrt{g\Delta D_s^{*3}}$, $\hat{\mathbf{k}}$ is the unit vector in the z-direction, and

$$\hat{\mathbf{n}} = \frac{-aD_{,x} - \eta_{,x}\,; -aD_{,y} - \eta_{,y}\,; 1}{\sqrt{1 + (aD_{,x} + \eta_{,x})^2 + (aD_{,y} + \eta_{,y})^2}} \tag{4.11}$$

is the unit vector in the direction normal to the bed. Furthermore, a is the conventional dimensionless level, scaled with the flow depth, where the bed boundary condition for the evaluation of the concentration field is imposed. Finally the dimensionless parameter Q_0 is given in this form:

$$Q_0 = \sqrt{g\Delta D_s^{*3}} \,/\, (U_0^* D_0^*)\,. \tag{4.12}$$

The last term in (4.10) accounts for the net flux of sediment exchanged between the bed layer and the water column (suspended load), which is computed as the difference between the actual value of local concentration at the reference level and the value C_e that concentration field may attain at equilibrium with the local and instantaneous flow conditions (see below the discussion of the boundary conditions).

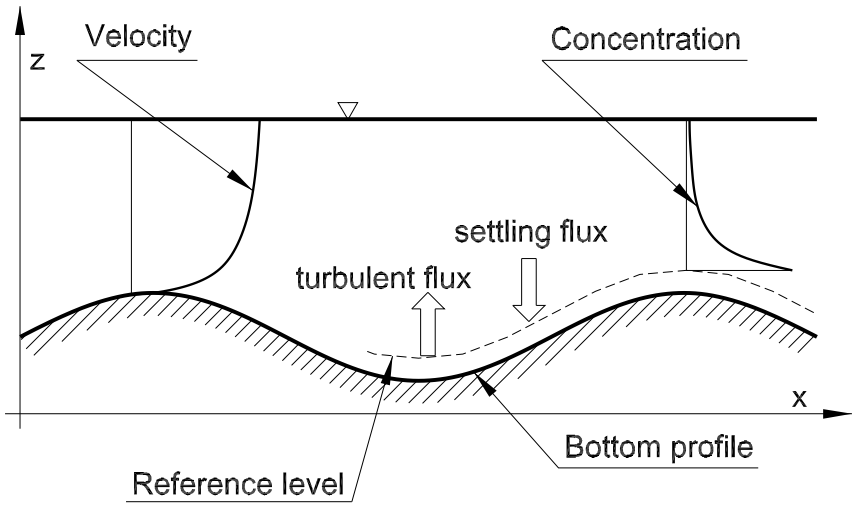

Figure 4.2: Suspension of sediment: relevant fluxes.

4.2 Boundary conditions

Suitable boundary conditions must be imposed for the differential problem (4.3). For the flow field the kinematic and dynamic conditions at the bed and at the free surface are imposed, which read:

- no slip at the bottom ($\xi = z_0$):

$$u = v = 0, \tag{4.13}$$

  with z_0 dimensionless conventional reference level where vanishing of flow velocity is imposed (see 5.14);

- cinematic condition and vanishing stress at the free surface ($\xi = 1$):

$$\beta w - u h_{,x} - v h_{,y} - h_{,t} = 0, \tag{4.14}$$

$$v_{,z} = 0, \quad u_{,z} = 0; \tag{4.15}$$

- cinematic condition at the bed ($\xi = z_0$):

$$\beta w - u\eta_{,x} - v\eta_{,y} - \eta_{,t} = 0; \tag{4.16}$$

Further boundary conditions are required for the concentration field at the free surface and at the bed. The first condition is that of vanishing sediment flux at the free surface ($\xi = 1$):

$$\left(W_s C\hat{\mathbf{k}} + \sqrt{C_{f0}}\Psi_T \nabla \mathbf{C}\right) \cdot \hat{\mathbf{n}}_s = 0, \tag{4.17}$$

with $\hat{\mathbf{n}}_s$ unit vector normal to the free surface:

$$\hat{\mathbf{n_s}} = \frac{-h_{,x}; -h_{,y}; 1}{\sqrt{1+(h_{,x})^2+(h_{,y})^2}}. \tag{4.18}$$

At the bed two different choices for the boundary condition have been discussed in the literature (see, e.g., Van Rijn (1985)). The simplest way is to impose the so-called "concentration boundary condition", which implies that at the reference level a the concentration attains the reference value C_e, which is evaluated using the local and instantaneous values of the flow characteristics. The second procedure is known as "gradient boundary condition" and prescribes a given sediment flux at the reference level a. This condition is more suitable under non uniform conditions, as pointed out by Parker (1978), since it doesn't force the concentrations field to attain its equilibrium value near the bed and leads to a smooth adaptation of the concentration filed to changing flow conditions. Note that in the case of uniform flow and concentration field (Rouse solution) the two conditions are equivalent. In the present work the "gradient boundary condition" is adopted, where the entrainment condition for the net flux of sediment at the reference level ($\xi = a$) is related to the difference between the local value of the concentration at the reference level and the equilibrium value C_e:

$$\sqrt{C_{f0}}\Psi_T \nabla \mathbf{C} \cdot \hat{\mathbf{n}} - \left(\mathbf{u} - W_s \hat{\mathbf{k}}\right) \hat{\mathbf{n}} C_e = 0, \tag{4.19}$$

Finally we impose the sidewalls of the channel to be impermeable both to the flow and to the sediment :

$$v = Q_{by} = 0 \qquad (y = \pm 1). \tag{4.20}$$

4.2.1 Boundary conditions in the longitudinal direction

Channel geometry is reported in figure 4.1. Besides the boundary conditions at the sidewalls, at the free surface and at the bed, suitable boundary conditions must be imposed in the longitudinal direction. The three dimensional formulation is able to reproduce the typical morphological structures at the meso-scale. The most important bed forms observed at this scale are bars, which display alternate sequences of scours and deposits. However, the development of regular trains of free bars requires a relatively long straight channel reach, say of the order of several bar wavelengths. In a numerical solution, like that discussed in the following chapters, this would imply the use of a fairly long computational domain, resulting in large computational time. However, when periodic boundary conditions are adopted the longitudinal extension of the domain can be set equal to bar wavelength.

The application of periodic boundary conditions is straightforward; for the generic variable,

denoted by Υ , periodicity can be written as:

$$\Upsilon(x = L_d, t, y, z) = \Upsilon(x = 0, t, y, z) \tag{4.21}$$

having denoted by L_d the dimensionless longitudinal length of the domain, scaled by the channel width.

In the fluvial case a given bed slope is set as the forcing term of the flow, while in tidal context the forcing term due to gravity, which is represented by term i_f in (4.3a), is assumed to be a sinusoidal function of time, which reproduces an oscillating bed shear stress, as employed by Seminara and Tubino (2001).

4.3 Closure and empirical inputs

Some empirical inputs must be introduced in the model for the evaluation of the sediment fluxes, settling velocity and bed roughness.

Bed load transport is quantified in terms of the local and instantaneous value of the Shields stress:

$$\theta = \frac{|\tau^*|}{\rho \Delta g D_s^*}, \tag{4.22}$$

where τ^* is the local bed stress vector evaluated in the form described in paragraph 5.1. Gravitational effects on bed load transport are taken into account, like in many other contributions (see for example Tubino et al., 1999), through a simplified semi-empirical approach which is formally justified only for small values of local bed slopes (Ikeda, 1982b; Kovacs and Parker, 1994). With reference to figure 4.1 we write:

$$Q_{bx} = \frac{|\mathbf{Q_b}|}{|\tau|} \left[\tau_x \cos(\alpha) - \tau_y \sin(\alpha)\right] \tag{4.23a}$$

$$Q_{by} = \frac{|\mathbf{Q_b}|}{|\tau|} \left[\tau_x \sin(\alpha) + \tau_y \cos(\alpha)\right] \tag{4.23b}$$

$$\tan(\alpha) = -\frac{r}{\beta\sqrt{\theta}} \frac{\partial \eta}{\partial n}, \tag{4.24}$$

where s is directed as the local bed stress vector, while n is orthogonal to the above direction. Finally bed load intensity $|\mathbf{Q_b}|$ is assumed to be a function of $\left(\theta - \overline{\theta}_{cr}\right)$, with

$$\overline{\theta}_{cr} = \left(\theta_{cr} + \frac{r_1}{\beta} \frac{\partial \eta}{\partial s}\right) \sqrt{1 - \frac{(\partial \eta / \partial n)^2}{\tan^2(\phi)}}, \tag{4.25}$$

where ϕ is the angle of repose of the bed material and θ_{cr} is the standard critical value of Shields stress for vanishing slope. According to experimental observations the empirical constants r and r_1 fall in the range $(0.3-0.6)$ and $(0.1-0.2)$, respectively.

Calculation are performed employing the Van Rijn (1985) relationships for the reference level a and the reference concentration C_e. They read:

$$C_e = 0.015\frac{D_s}{a}\frac{T^{\frac{3}{2}}}{R_p^{0.2}} \tag{4.26a}$$

$$T = \frac{\theta' - \overline{\theta}_{cr}}{\overline{\theta}_{cr}} \tag{4.26b}$$

$$a = \max(0.01, e_s) \tag{4.26c}$$

where e_s is the equivalent dimensionless roughness which accounts for the effect of small scale bed forms, like dunes or ripples, which are often superimposed on meso-scale topography when the sediment is fine, and θ' is the effective Shields stress acting on the bed. Its definition arises from the stress-partition procedure which is typically adopted to model resistance effects induced by small scale bed-forms (see Einstein, 1950), which assumes that the total bed stress can be viewed as the sum of friction (the effective shear stress) and form drag. The local values of the effective shear stress acting on the bed is computed, in dimensionless form, that is in term of the Shields stress θ', using the empirical formulation proposed by Engelund and Fredsoe (1982), namely

$$\theta' = 0.06 + 0.3\theta^{1.5}, \tag{4.27}$$

where θ is computed using the total shear stress.

The above approach is also used to compute the friction coefficient C_f in the following form:

$$C_f^{-2} = \sqrt{\frac{\theta'}{\theta}}\left[6 + 2.5\ln\left(\frac{\theta'}{2.5\theta D_s}\right)\right] \tag{4.28}$$

Implicit in this procedure is the assumption that small scale bed-forms respond instantaneously to changing flow conditions, as suggested, for instance, by field observations in the Severn estuary where mega-ripples crests can be rebuilt within a tidal cycle, resulting in amplitude changes by as much as 2 metres (Harris and Collins, 1985).
Furthermore, the intensity of bed load transport $|\mathbf{Q_b}|$ is evaluated using Parker's formula:

$$|\mathbf{Q_b}| = 0.00218\theta^{\frac{3}{2}}G(\varsigma) \tag{4.29a}$$

$$G = \begin{cases} 5474\,(1-0.853/\varsigma)^{4.5} & \text{if} \quad \varsigma \geq 1.5878 \\ \exp\left[14.2\,(\varsigma-1)-9.28\,(\varsigma-1)^2\right] & \text{if} \quad 1 \leq \varsigma < 1.65 \\ \varsigma^{14.2} & \text{if} \quad \varsigma \leq 1 \end{cases} \tag{4.29b}$$

$$\varsigma = \frac{\theta'}{0.0386} \tag{4.29c}$$

Finally a fit of the experimental curve reported by Parker (1978) is used to estimate the dimensional particle fall velocity, in the following form:

$$W_s^* = \sqrt{g\Delta D_s^*}\,10^{\left(-1.181+0.966A-0.1804A^2+0.003746A^3+0.0008782A^4\right)} \tag{4.30}$$

where $A = \log_{10}(Rp)$.

5 A three dimensional numerical model for suspended sediment transport

In the present chapter we describe the finite difference numerical model which is adopted for the solution of the flow and concentration field. In order to keep the required detail to reproduce correctly suspended sediment transport and its effect on bed morphology the problem is tackled within the context of a three-dimensional framework, as discussed in the preceding chapter. Many numerical schemes have been developed so far for the solution of the flow field using a 3D approach, while only few contributions are available in the literature in which a 3D approach is used for the solution of the concentration field. In the last years the increasing interest for the solution of environmental problems, related to estuarine and coastal sediment dynamics and to the transport of heavy metals and toxic waste through their adsorption on sediment particles, has motivated the development of more refined models, like those proposed by Lin and Falconer (1996), in which a semi analytical scheme is proposed for the simulation of the concentration field in the Humber estuary, and by Wu et al. (2000), where a $k-\varepsilon$ approach for the turbulence closure is employed to investigate the over-deepening process which occurs when two straight channels are joined thought a 180 degree bend.

In the present model we follow the numerical procedure proposed by Casulli and Cattani (1994), according to which the non-linear terms appearing in the momentum equations are discretized using a lagrangian approach. Furthermore, the concentration field is solved using an original semi-analytical scheme. The resulting numerical scheme seems sufficiently accurate and efficient to represent adequately the flow and concentration fields of fluvial and tidal systems and their role in the development of bed topography.

5.1 Vertical coordinate

Velocity profiles display fairly large gradients close to the bottom due to the non slip condition. Similarly, concentration profiles exhibit a sharp variation close to the bed where turbulence changes quite rapidly and its intensity is strong enough to keep a relative large concentration of

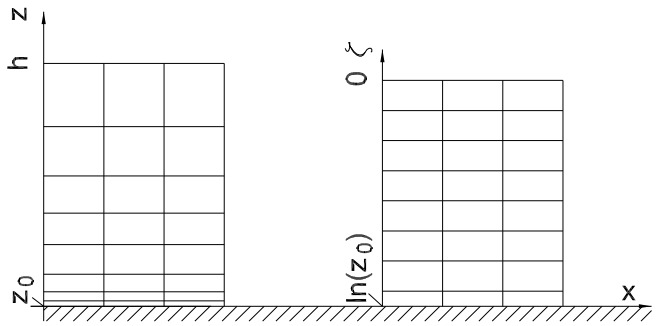

Figure 5.1: Computational domain in natural scale (left) and in logarithmic deformed scale (right).

suspended particles. The 3D approach adopted herein allows for the direct evaluation of the bed shear stress, which takes the following simplified form when the shallow water approximation is introduced:

$$\tau = (\tau_x, \tau_y) = \left(\nu_T \frac{\partial u}{\partial z}, \nu_T \frac{\partial v}{\partial z} \right) \Bigg|_{z^\tau} \tag{5.1}$$

where τ is the dimensionless shear stress, scaled with $\rho\sqrt{C_{f0}}U_0^{*2}$, and z^τ is a suitable dimensionless level for the evaluation of the bed shear stress, which can be assumed to be of the same order of magnitude of the grain size D_s. Analogously, the evaluation of turbulent fluxes in the transport equation for suspended particles requires the numerical estimate of vertical gradients of velocity "near the bed". Hence, using the natural vertical boundary fitted coordinate ξ, as defined in (4.4), the relatively small vertical spacing needed to reproduce correctly the solution near the bed would involve an exceedingly large number of computational points, in particular near the free surface: there, the velocity gradient attains smaller values and a sparser numerical grid is sufficient to obtain the required accuracy. Hence, in the present model a suitable logarithmic vertical coordinate is introduced in the following form:

$$\zeta = \ln(\xi) = \ln\left(\frac{z-\eta}{D} \right) \tag{5.2}$$

through which a grid is obtained whose density decreases from the bed to the free surface (see figure 5.1). The above transformation leads to a vertical domain falling within the range

$$\zeta \in [\ln(z_0), 0].$$

The logarithmic vertical coordinate ζ also minimizes the numerical truncation errors. Let us consider the simple case of a uniform flow. In this case the vertical velocity profile, which is logarithmic in the variable ξ, becomes a linear function when the variable ζ is adopted. The trun-

cation error of the numerical scheme, which is first order accurate in the vertical direction, as will be pointed out in the following sections, is proportional to the second derivative of velocity with respect to ζ in some internal point between the grid points; hence, the error becomes vanishingly small when the logarithmic coordinate is used. It is worth noticing that in tidal flows, where conditions are typically non uniform, the vertical velocity profiles often display for most of the tidal cycle a self similar structure, that is a vertical logarithmic structure with the mean velocity varying in time due to the tidal oscillation. Hence, also in this case the use of the variable ζ may provide a better numerical approximation.

As for the computational efficiency, the number of grid points which are found to be necessary for a good accuracy of the numerical simulation when using the natural vertical coordinate ξ, for reasonable choices of flow parameters, is about $200-300$ in the vertical direction, while using the logarithmic coordinate ζ the number of grid point to achieve the same accuracy reduces by one order of magnitude.

5.2 Equations

In order to solve equations (4.3a), (4.3b) and (4.3c) we first introduce the transformation into the new coordinate system, in which we use the vertical coordinate ζ defined in (5.2). The coordinate system is non-orthogonal and boundary fitted; the computational domain is transformed into a nice rectangular box. The following transformation rules are introduced:

$$\frac{\partial}{\partial t} \rightarrow \frac{\partial}{\partial t} - r_t \frac{e^{-\zeta}}{D} \frac{\partial}{\partial \zeta} \tag{5.3a}$$

$$\frac{\partial}{\partial x} \rightarrow \frac{\partial}{\partial x} - r_x \frac{e^{-\zeta}}{D} \frac{\partial}{\partial \zeta} \tag{5.3b}$$

$$\frac{\partial}{\partial y} \rightarrow \frac{\partial}{\partial y} - r_y \frac{e^{-\zeta}}{D} \frac{\partial}{\partial \zeta} \tag{5.3c}$$

$$\frac{\partial}{\partial z} \rightarrow \frac{e^{-\zeta}}{D} \frac{\partial}{\partial \zeta} \tag{5.3d}$$

where the coefficients r_t, r_x, and r_y are, respectively:

$$r_t = \frac{\partial \eta}{\partial t} + \frac{z-\eta}{D} \frac{\partial D}{\partial t} = \frac{\partial \eta}{\partial t} + e^{\zeta} \frac{\partial D}{\partial t} \tag{5.4a}$$

$$r_x = \frac{\partial \eta}{\partial x} + \frac{z-\eta}{D} \frac{\partial D}{\partial x} = \frac{\partial \eta}{\partial x} + e^{\zeta} \frac{\partial D}{\partial x} \tag{5.4b}$$

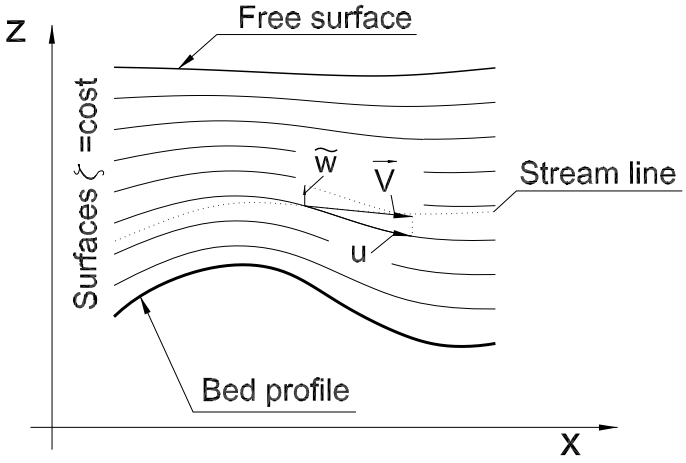

Figure 5.2: The boundary fitted coordinate system.

$$r_y = \frac{\partial \eta}{\partial y} + \frac{z-\eta}{D}\frac{\partial D}{\partial y} = \frac{\partial \eta}{\partial y} + e^{\zeta}\frac{\partial D}{\partial y} \tag{5.4c}$$

In order to write the governing equations into the new system of coordinate it is convenient to introduce the contravariant vertical component of the velocity. Following Pielke (1994) we define the contravariant vertical component of the velocity as:

$$\widetilde{w} = w - r_t - u r_x - v r_y \tag{5.5}$$

It is worth noticing that $\widetilde{w}$ represents the vertical velocity in terms of base vectors that are tangent to the surface along which the ζ coordinate is constant, as represented in figure 5.2. Using the contravariant vertical component of velocity, the vertical Courant number $c_z = \widetilde{w}\frac{\Delta t}{\Delta \zeta}$, where $\Delta\zeta$ is the vertical spacing and Δt the time step, keeps generally very small in the computation. In particular, the Courant number c_z vanishes at the bed and at the free surface, because bed and free surface are steram lines and coincide with the surfaces $\zeta = \ln(z_0)$ and $\zeta = 0$, respectively.
In the new coordinate system, and adopting (5.5), equations (4.3) become:

$$u_{,t} + u u_{,x} + v u_{,y} + \beta \frac{e^{-\zeta}}{D}\widetilde{w} u_{,\zeta} - \gamma \frac{e^{-\zeta}}{D}\left(\frac{e^{-\zeta}}{D}\nu_T u_{,\zeta}\right)_{,\zeta} + \frac{h_{,x}}{F_0^2} - \frac{i_F}{F_0^2} = 0, \tag{5.6a}$$

$$v_{,t} + u v_{,x} + v v_{,y} + \beta \frac{e^{-\zeta}}{D}\widetilde{w} v_{,\zeta} - \gamma \frac{e^{-\zeta}}{D}\left(\frac{e^{-\zeta}}{D}\nu_T v_{,\zeta}\right)_{,\zeta} + \frac{h_{,y}}{F_0^2} = 0, \tag{5.6b}$$

$$u_{,x} + v_{,y} + \beta \frac{e^{-\zeta}}{D}\left(\widetilde{w} + r_t\right)_{,\zeta} = 0, \tag{5.7}$$

and the boundary conditions read:

- no slip at the bottom ($\zeta = \ln(z_0)$):

$$u = v = 0, \tag{5.8}$$

- vanishing stress at the free surface ($\zeta = 0$):

$$v_{,\zeta} = 0, \quad u_{,\zeta} = 0; \tag{5.9}$$

The kinematic conditions at the bed and at the free surface are automatically satisfied provided $\widetilde{w} = 0$ there.

Finally, the advection diffusion equation for the concentration of suspended sediment (4.3d) becomes:

$$\begin{aligned}(CD)_{,t} + (DuC)_{,x} + (DvC)_{,y} + \beta e^{-\zeta}\left[(\widetilde{w} - W_s)C\right]_{,\zeta} - \\ -\gamma e^{-\zeta}\left(\frac{e^{-\zeta}}{D}\Psi_T C_{,\zeta}\right)_{,\zeta} = 0,\end{aligned} \tag{5.10}$$

The boundary conditions for the above equation are discussed in section 5.3.3.

5.3 Numerical solution

The solutions for the flow field and the concentration field are obtained using finite-differences technique. The spatial mesh adopted in the numerical solution is a staggered grid (figures 5.3 and 5.4) and consists of rectangular boxes of length Δx, width Δy and height $\Delta\zeta$. The center of each box is numbered with indices i, j and k. The discrete values of the velocity components are defined as indicated in figure 5.3 and 5.4: the x-component is evaluated at point $i+\frac{1}{2}, j, k$ (squares in figures 5.4 and 5.6), the y-component at point $i, j+\frac{1}{2}, k$ (crosses in figure 5.4) and the z-component at point $i, j, k+\frac{1}{2}$ (diamonds in figure 5.6). The free surface elevation and the bed elevation are defined at integer i and j (circles in figure 5.4); the sediment concentration is defined at the centre of each computational cell (stars in figure 5.6). The equations (5.6) and (5.7), with boundary conditions (5.8) and (5.9), are then solved through a semi-implicit finite difference scheme. For the solution of the flow field the $Eulerian - Lagrangian$ approach is adopted, in the form proposed by Casulli and Cattani (1994), which has been suitably modified to account for the no slip condition at the bed.

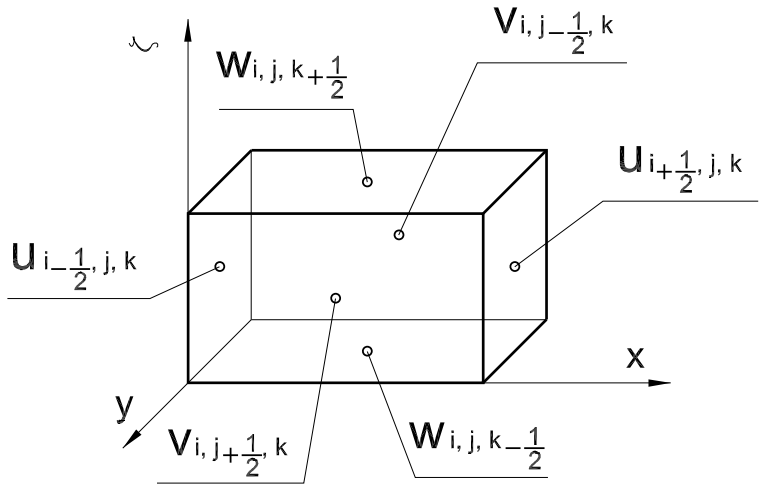

Figure 5.3: Computational cell.

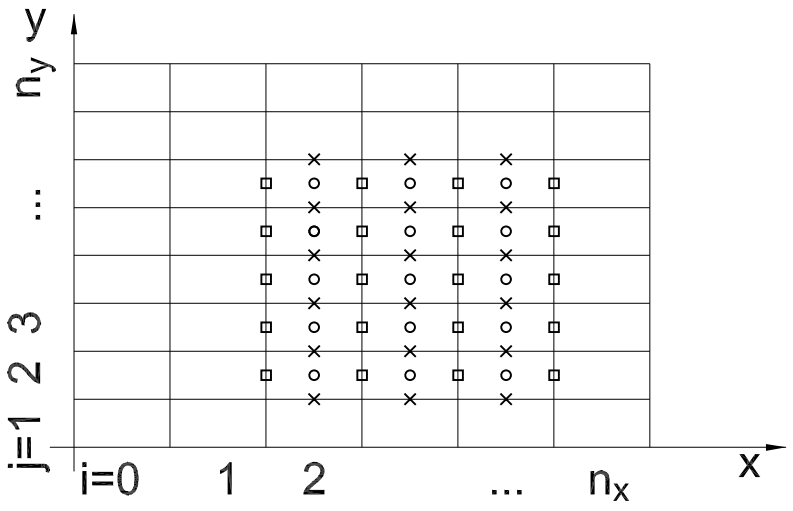

Figure 5.4: Computational grid: horizontal spacing.

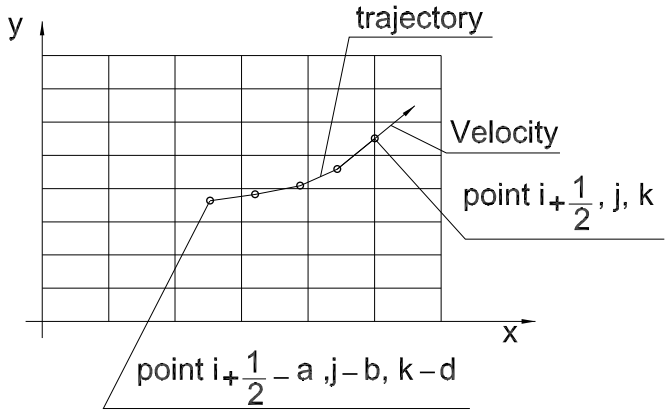

Figure 5.5: Lagrangian approach, an example of trajectory.

5.3.1 The numerical scheme of Casulli and Cattani (1994)

The numerical method used here is semi-implicit, in particular the non-linear terms of equations (5.6) are solved explicitly using a *Lagrangian* approach, while the pressure term and the viscous term are solved implicitly. The first step of the procedure consists in the evaluation of the total derivative

$$\frac{du}{dt} = u_{,t} + uu_{,x} + vu_{,y} + \beta\frac{e^{-\zeta}}{D}\widetilde{w}u_{,\zeta} \simeq \frac{u^{n+1}_{i+\frac{1}{2},j,k} - u^{n}_{i+\frac{1}{2}-a,j-b,k-d}}{\Delta t}, \tag{5.11}$$

where a, b, c define the starting point of the trajectory of the considered water particle, as shown in figure 5.5, and are computed explicitly:

$$a = \int_{\Delta t} u^n dt \tag{5.12a}$$

$$b = \int_{\Delta t} v^n dt \tag{5.12b}$$

$$d = \int_{\Delta t} \beta\frac{e^{-\zeta}}{D}\widetilde{w}^n dt \tag{5.12c}$$

The trajectories are evaluated using a three-linear interpolation algorithm; therefore, the numerical scheme is first order accurate in the spatial coordinates x, y, ζ. It is worth noticing that if the time step Δt is relatively small, that is the Courant number is less that one, the *Lagrangian* scheme reduces to an up-wind difference scheme, while for relatively large values of the time step, that is for Courant numbers larger that one, the *Lagrangian* approach keeps stable, while the numerical estimate worsen. The trajectories are integrated using a time substep $\Delta t'$ smaller than the time step Δt adopted in the numerical solution, in order to cross at each substep at most one cell border (see

figure 5.5).

The remaining terms of the momentum equations (5.6) are discretized using central differences; in order to obtain a good accuracy in time the pressure term is evaluated at time step $n+\vartheta$, the weight ϑ falling within the range $\left(\frac{1}{2},1\right]$ in order to preserve the stability of the scheme. Notice that the more ϑ tends to $\frac{1}{2}$, the more the scheme is accurate; for $\vartheta=\frac{1}{2}$ the scheme is second order accurate in time but unfortunately it is unstable.

The momentum equations in discrete form read:

$$\frac{u^{n+1}_{i+\frac{1}{2},j,k}-u^{n}_{i+\frac{1}{2}-a,\,j-b,k-c}}{\Delta t}=-\frac{h^{n+\vartheta}_{i+1,j}-h^{n+\vartheta}_{i,j}}{F_0^2\Delta x}+\frac{i_F}{F_0^2}+\gamma\frac{e^{-\zeta_k}}{\left(D^{n}_{i+\frac{1}{2},j}\Delta\zeta\right)^2}$$
$$\left[e^{-\zeta_{k+\frac{1}{2}}}\nu^{n}_{T,i+\frac{1}{2},j,k+\frac{1}{2}}\left(u^{n+1}_{i+\frac{1}{2},j,k+1}-u^{n+1}_{i+\frac{1}{2},j,k}\right)-e^{-\zeta_{k-\frac{1}{2}}}\nu^{n}_{T,i+\frac{1}{2},j,k-\frac{1}{2}}\left(u^{n+1}_{i+\frac{1}{2},j,k}-u^{n+1}_{i+\frac{1}{2},j,k-1}\right)\right] \quad (5.13a)$$

$$\frac{v^{n+1}_{i,j+\frac{1}{2},k}-v^{n}_{i-a,\,j+\frac{1}{2}-b,k-c}}{\Delta t}=-\frac{h^{n+\vartheta}_{i,j+1}-h^{n+\vartheta}_{i,j}}{F_0^2\Delta y}+\gamma\frac{e^{-\zeta_k}}{\left(D^{n}_{i,j+\frac{1}{2}}\Delta\zeta\right)^2}$$
$$\left[e^{-\zeta_{k+\frac{1}{2}}}\nu^{n}_{T,i,j+\frac{1}{2},k+\frac{1}{2}}\left(v^{n+1}_{i,j+\frac{1}{2},k+1}-v^{n+1}_{i,j+\frac{1}{2},k}\right)-e^{-\zeta_{k-\frac{1}{2}}}\nu^{n}_{T,i,j+\frac{1}{2},k-\frac{1}{2}}\left(v^{n+1}_{i,j+\frac{1}{2},k}-v^{n+1}_{i,j+\frac{1}{2},k-1}\right)\right] \quad (5.13b)$$

The eddy viscosity coefficients and the flow depth are evaluated explicitly at time step n such that the resulting algebraic system is linear. In equations (5.13), for $k=1$ the values of flow velocity components at the bed appear, namely $u_{i+\frac{1}{2},j,0}$ and $v_{i,j+\frac{1}{2},0}$, which are set equal to zero, according to the no-slip boundary condition at the bed. At the free surface, $k=n_z+\frac{1}{2}$, the vanishing stress condition is imposed $u_{,\zeta}=v_{,\zeta}=0$. In the vertical direction the flow domain is divided into $n_z+\frac{1}{2}$ parts, as shown in figure 5.6. Below the level $k=\frac{1}{2}$ the velocity is zero, the additional half-cell at the bed is introduced to impose the no-slip boundary condition. The level $k=0$ correspond to the conventional level ζ_0 for the velocity, which is evaluated using the reference state:

$$z_0=e^{-\left(0.777+K_v C_{f0}^{-\frac{1}{2}}\right)}, \quad (5.14)$$

$$\zeta_0=\ln(z_0)=-\left(0.777+K_v C_{f0}^{-\frac{1}{2}}\right). \quad (5.15)$$

This approach allows one to take into account also the equivalent bed roughness which is used to simulate the presence of ripples or dunes, using a suitable value of C_{f0}. Notice that the variations of the reference level ζ_0 due to changing flow conditions are assumed to be negligible in the computation.

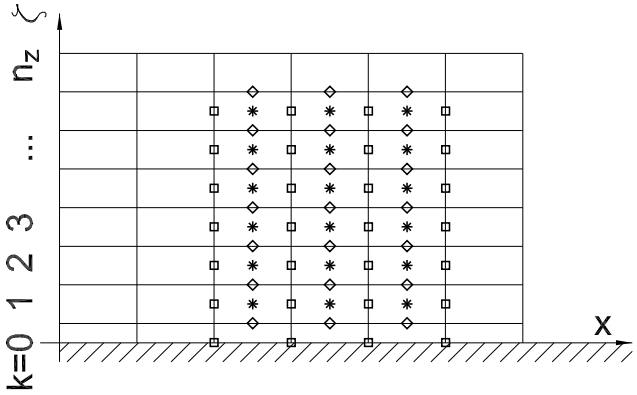

Figure 5.6: Computational grid: vertical spacing. Near the bed the half cell allows to impose the no-slip condition, at the free surface the whole cell allows to impose the vanishing stress condition.

The generic term appearing in the equations, denoted by Υ in the following, is evaluated at the time step $n+\vartheta$ using the following linear combination:

$$\Upsilon^{n+\vartheta} = (1-\vartheta)\,\Upsilon^{n} + \vartheta\Upsilon^{n+1}. \tag{5.16}$$

Equations (5.13a) and (5.13b) can be rewritten in vectorial form:

$$\mathbf{A}^{n}_{i+\frac{1}{2},j}\mathbf{U}^{n+1}_{i+\frac{1}{2},j} = \mathbf{G}^{n}_{i+\frac{1}{2},j} - \frac{\vartheta}{F_0^2\Delta x}\left(h^{n+1}_{i+1,j} - h^{n+1}_{i,j}\right) D^{n}_{i+\frac{1}{2},j}\Delta\zeta\Delta t\mathbf{E}^{\zeta} \tag{5.17a}$$

$$\mathbf{A}^{n}_{i,j+\frac{1}{2}}\mathbf{V}^{n+1}_{i,j+\frac{1}{2}} = \mathbf{G}^{n}_{i,j+\frac{1}{2}} - \frac{\vartheta}{F_0^2\Delta y}\left(h^{n+1}_{i,j+1} - h^{n+1}_{i,j}\right) D^{n}_{i,j+\frac{1}{2}}\Delta\zeta\Delta t\mathbf{E}^{\zeta} \tag{5.17b}$$

where the vectors $\mathbf{U}^{n+1}_{i+\frac{1}{2},j}$ and $\mathbf{V}^{n+1}_{i,j+\frac{1}{2}}$ are respectively:

$$\mathbf{U}^{n+1}_{i+\frac{1}{2},j} = \begin{pmatrix} u^{n+1}_{i+\frac{1}{2},j,n_z} \\ u^{n+1}_{i+\frac{1}{2},j,n_z-1} \\ .... \\ u^{n+1}_{i+\frac{1}{2},j,2} \\ u^{n+1}_{i+\frac{1}{2},j,1} \end{pmatrix}, \qquad \mathbf{V}^{n+1}_{i,j+\frac{1}{2}} = \begin{pmatrix} v^{n+1}_{i,j+\frac{1}{2},n_z} \\ v^{n+1}_{i,j+\frac{1}{2},n_z-1} \\ .... \\ v^{n+1}_{i,j+\frac{1}{2},2} \\ v^{n+1}_{i,j+\frac{1}{2},1} \end{pmatrix}, \tag{5.18}$$

the three-diagonal matrixes $\mathbf{A}^n_{i+\frac{1}{2},j}$ and $\mathbf{V}^{n+1}_{i,j+\frac{1}{2}}$ read respectively:

$$\mathbf{A}^n_{i+\frac{1}{2},j} = \begin{pmatrix} d^p_{i+\frac{1}{2},j,n_z} & d^s_{i+\frac{1}{2},j,n_z} & & & \\ d^i_{i+\frac{1}{2},j,n_z-1} & d^p_{i+\frac{1}{2},j,n_z-1} & d^s_{i+\frac{1}{2},j,n_z-1} & & \\ & \dots & \dots & \dots & \\ & & d^i_{i+\frac{1}{2},j,2} & d^p_{i+\frac{1}{2},j,2} & d^s_{i+\frac{1}{2},j,2} \\ & & & d^i_{i+\frac{1}{2},j,1} & d^p_{i+\frac{1}{2},j,1} \end{pmatrix}, \tag{5.19}$$

$$d^p_{i+\frac{1}{2},j,n_z} = D^n_{i+\frac{1}{2},j}\Delta\zeta e^{\zeta_{n_z}} + \gamma\frac{\Delta t\nu^n_{T,i+\frac{1}{2},j,n_z-\frac{1}{2}}}{D^n_{i+\frac{1}{2},j}\Delta\zeta e^{\zeta_{n_z-\frac{1}{2}}}}, \tag{5.20a}$$

$$d^p_{i+\frac{1}{2},j,k} = D^n_{i+\frac{1}{2},j}\Delta\zeta e^{\zeta_k} + \gamma\frac{\Delta t\nu^n_{T,i+\frac{1}{2},j,k+\frac{1}{2}}}{D^n_{i+\frac{1}{2},j}\Delta\zeta e^{\zeta_{k+\frac{1}{2}}}} + \gamma\frac{\Delta t\nu^n_{T,i+\frac{1}{2},j,k-\frac{1}{2}}}{D^n_{i+\frac{1}{2},j}\Delta\zeta e^{\zeta_{k-\frac{1}{2}}}}, \quad k = n_z - 1 \dots 1 \tag{5.20b}$$

$$d^s_{i+\frac{1}{2},j,k} = -\gamma\frac{\Delta t\nu^n_{T,i+\frac{1}{2},j,k-\frac{1}{2}}}{D^n_{i+\frac{1}{2},j}\Delta\zeta e^{\zeta_{k-\frac{1}{2}}}}, \quad k = n_z \dots 2 \tag{5.20c}$$

$$d^i_{i+\frac{1}{2},j,k} = -\gamma\frac{\Delta t\nu^n_{T,i+\frac{1}{2},j,k+\frac{1}{2}}}{D^n_{i+\frac{1}{2},j}\Delta\zeta e^{\zeta_{k+\frac{1}{2}}}}, \quad k = n_z - 1 \dots 1 \tag{5.20d}$$

$$\mathbf{A}^n_{i,j+\frac{1}{2}} = \begin{pmatrix} d^p_{i,j+\frac{1}{2},n_z} & d^s_{i,j+\frac{1}{2},n_z} & & & \\ d^i_{i,j+\frac{1}{2},n_z-1} & d^p_{i,j+\frac{1}{2},n_z-1} & d^s_{i,j+\frac{1}{2},n_z-1} & & \\ & \dots & \dots & \dots & \\ & & d^i_{i,j+\frac{1}{2},2} & d^p_{i,j+\frac{1}{2},2} & d^s_{i,j+\frac{1}{2},2} \\ & & & d^i_{i,j+\frac{1}{2},1} & d^p_{i,j+\frac{1}{2},1} \end{pmatrix}, \tag{5.21}$$

$$d^p_{i,j+\frac{1}{2},n_z} = D^n_{i,j+\frac{1}{2}}\Delta\zeta e^{\zeta_{n_z}} + \gamma\frac{\Delta t\nu^n_{T,i,j+\frac{1}{2},n_z-\frac{1}{2}}}{D^n_{i,j+\frac{1}{2}}\Delta\zeta e^{\zeta_{n_z-\frac{1}{2}}}}, \tag{5.22a}$$

$$d^p_{i,j+\frac{1}{2},k} = D^n_{i,j+\frac{1}{2}}\Delta\zeta e^{\zeta_k} + \gamma\frac{\Delta t\nu^n_{T,i,j+\frac{1}{2},k+\frac{1}{2}}}{D^n_{i,j+\frac{1}{2}}\Delta\zeta e^{\zeta_{k+\frac{1}{2}}}} + \gamma\frac{\Delta t\nu^n_{T,i,j+\frac{1}{2},k-\frac{1}{2}}}{D^n_{i,j+\frac{1}{2}}\Delta\zeta e^{\zeta_{k-\frac{1}{2}}}}, \quad k = n_z - 1 \dots 1 \tag{5.22b}$$

$$d^s_{i,j+\frac{1}{2},k} = -\gamma\frac{\Delta t\nu^n_{T,i,j+\frac{1}{2},k-\frac{1}{2}}}{D^n_{i,j+\frac{1}{2}}\Delta\zeta e^{\zeta_{k-\frac{1}{2}}}}, \quad k = n_z \dots 2 \tag{5.22c}$$

$$d^i_{i,j+\frac{1}{2},k} = -\gamma \frac{\Delta t \nu^n_{T,i,j+\frac{1}{2},k+\frac{1}{2}}}{D^n_{i,j+\frac{1}{2}} \Delta\zeta e^{\zeta_{k+\frac{1}{2}}}}, k = n_z - 1 \ldots 1 \tag{5.22d}$$

and finally:

$$\mathbf{G}^n_{i+\frac{1}{2},j} = \begin{pmatrix} \left[\frac{u^n_{i+\frac{1}{2}-a,j-b,n_z-c}}{\Delta t} - \frac{1-\vartheta}{F_0^2 \Delta x}\left(h^n_{i+1,j} - h^n_{i,j}\right) + i_F\right] D^n_{i+\frac{1}{2},j} \Delta\zeta \Delta t\, e^{\zeta_{n_z}} \\ \left[\frac{u^n_{i+\frac{1}{2}-a,j-b,n_z-1-c}}{\Delta t} - \frac{1-\vartheta}{F_0^2 \Delta x}\left(h^n_{i+1,j} - h^n_{i,j}\right) + i_F\right] D^n_{i+\frac{1}{2},j} \Delta\zeta \Delta t\, e^{\zeta_{n_z-1}} \\ \ldots \\ \left[\frac{u^n_{i+\frac{1}{2}-a,j-b,2-c}}{\Delta t} - \frac{1-\vartheta}{F_0^2 \Delta x}\left(h^n_{i+1,j} - h^n_{i,j}\right) + i_F\right] D^n_{i+\frac{1}{2},j} \Delta\zeta \Delta t\, e^{\zeta_2} \\ \left[\frac{u^n_{i+\frac{1}{2}-a,j-b,1-c}}{\Delta t} - \frac{1-\vartheta}{F_0^2 \Delta x}\left(h^n_{i+1,j} - h^n_{i,j}\right) + i_F\right] D^n_{i+\frac{1}{2},j} \Delta\zeta \Delta t\, e^{\zeta_1} \end{pmatrix}, \tag{5.23}$$

$$\mathbf{G}^n_{i,j+\frac{1}{2}} = \begin{pmatrix} \left[\frac{v^n_{i-a,j+\frac{1}{2}-b,n_z-c}}{\Delta t} - \frac{1-\vartheta}{F_0^2 \Delta y}\left(h^n_{i,j+1} - h^n_{i,j}\right)\right] D^n_{i,j+\frac{1}{2}} \Delta\zeta \Delta t\, e^{\zeta_{n_z}} \\ \left[\frac{v^n_{i-a,j+\frac{1}{2}-b,n_z-1-c}}{\Delta t} - \frac{1-\vartheta}{F_0^2 \Delta y}\left(h^n_{i,j+1} - h^n_{i,j}\right)\right] D^n_{i,j+\frac{1}{2}} \Delta\zeta \Delta t\, e^{\zeta_{n_z-1}} \\ \ldots \\ \left[\frac{v^n_{i-a,j+\frac{1}{2}-b,2-c}}{\Delta t} - \frac{1-\vartheta}{F_0^2 \Delta y}\left(h^n_{i,j+1} - h^n_{i,j}\right)\right] D^n_{i,j+\frac{1}{2}} \Delta\zeta \Delta t\, e^{\zeta_2} \\ \left[\frac{v^n_{i-a,j+\frac{1}{2}-b,1-c}}{\Delta t} - \frac{1-\vartheta}{F_0^2 \Delta y}\left(h^n_{i,j+1} - h^n_{i,j}\right)\right] D^n_{i,j+\frac{1}{2}} \Delta\zeta \Delta t\, e^{\zeta_1} \end{pmatrix}, \tag{5.24}$$

$$\mathbf{E}^\zeta = \begin{pmatrix} e^{\zeta_{n_z}} \\ e^{\zeta_{n_z-1}} \\ \ldots \\ e^{\zeta_2} \\ e^{\zeta_1} \end{pmatrix} = \begin{pmatrix} 1 \\ \ldots \\ \ldots \\ \ldots \\ z_0 \end{pmatrix}. \tag{5.25}$$

The flow continuity equation (4.3c) is integrated over the flow depth in the following form:

$$\int_{\eta+z_0}^{h} u_{,x}\, dz + \int_{\eta+z_0}^{h} v_{,y}\, dz + \beta\left(w|_{free\,surface} - w|_{bed}\right) = 0. \tag{5.26}$$

Using the Leibnitz rule and recalling the kinematic conditions at the bed (4.16) and at the free surface (4.15) we then obtain:

$$\frac{\partial(h-\eta)}{\partial t} + \frac{\partial}{\partial x}\left[\int_{\eta+z_0}^{h} u dz\right] + \frac{\partial}{\partial y}\left[\int_{\eta+z_0}^{h} v dz\right] = 0. \tag{5.27}$$

Finally, introducing the transformation (5.2) we obtain:

$$\frac{\partial (h-\eta)}{\partial t} + \frac{\partial}{\partial x}\left[D\int_{\ln z_0}^{0} u e^{\zeta} d\zeta\right] + \frac{\partial}{\partial y}\left[D\int_{\ln z_0}^{0} v e^{\zeta} d\zeta\right] = 0. \tag{5.28}$$

The numerical algorithm adopted in the present work is decoupled, namely the flow field and the bottom topography are evaluated independently. Therefore, as a first step the flow field is evaluated, keeping a constant bed level; then the new bed topography is updated with reference to the computed flow field. According to this procedure equation (5.28), in discrete form, becomes:

$$\begin{aligned}&\frac{h_{i,j}^{n+1}-h_{i,j}^{n}}{\Delta t} + \frac{1}{\Delta x}\left(D^{n}_{i+\frac{1}{2},j}\sum_{k=1}^{n_z} u^{n+\vartheta}_{i+\frac{1}{2},j,k} e^{\zeta_k}\Delta\zeta - D^{n}_{i-\frac{1}{2},j}\sum_{k=1}^{n_z} u^{n+\vartheta}_{i-\frac{1}{2},j,k} e^{\zeta_k}\Delta\zeta\right) + \\ &+ \frac{1}{\Delta y}\left(D^{n}_{i,j+\frac{1}{2}}\sum_{k=1}^{n_z} v^{n+\vartheta}_{i,j+\frac{1}{2},k} e^{\zeta_k}\Delta\zeta - D^{n}_{i,j-\frac{1}{2}}\sum_{k=1}^{n_z} v^{n+\vartheta}_{i,j-\frac{1}{2},k} e^{\zeta_k}\Delta\zeta\right) = 0.\end{aligned} \tag{5.29}$$

Using the vectorial notation, recalling the relationship (5.16) and substituting $\mathbf{U^{n+1}_{i+\frac{1}{2},j}}$ and $\mathbf{V^{n+1}_{i,j+\frac{1}{2}}}$ from equation (5.17) the continuity equation can be given the following discrete form:

$$\begin{aligned}&h_{i,j}^{n+1} - h_{i,j}^{n} - \frac{\vartheta^2\Delta t^2}{F_0^2\Delta x^2}\left[\left(D^{n}_{i+\frac{1}{2},j}\Delta\zeta\right)^2\left(h^{n+1}_{i+1,j}-h^{n+1}_{i,j}\right)\left(\mathbf{E}^{\zeta T}\cdot\mathbf{A}^{-1}\cdot\mathbf{E}^{\zeta}\right)_{i+\frac{1}{2},j} - \right. \\ &\left. - \left(D^{n}_{i-\frac{1}{2},j}\Delta\zeta\right)^2\left(h^{n+1}_{i,j}-h^{n+1}_{i-1,j}\right)\left(\mathbf{E}^{\zeta T}\cdot\mathbf{A}^{-1}\cdot\mathbf{E}^{\zeta}\right)_{i-\frac{1}{2},j}\right] + \frac{\vartheta\Delta t}{\Delta x}\left[D^{n}_{i+\frac{1}{2},j}\Delta\zeta\left(\mathbf{E}^{\zeta T}\cdot\mathbf{A}^{-1}\cdot\mathbf{G}^{n}\right)_{i+\frac{1}{2},j} - \right. \\ &\left. - D^{n}_{i-\frac{1}{2},j}\Delta\zeta\left(\mathbf{E}^{\zeta T}\cdot\mathbf{A}^{-1}\cdot\mathbf{G}^{n}\right)_{i-\frac{1}{2},j}\right] + \frac{(1-\vartheta)\Delta t}{\Delta x}\left(D^{n}_{i+\frac{1}{2},j}\mathbf{U}^{n}_{i+\frac{1}{2},j}\cdot\mathbf{E}^{\zeta}\Delta\zeta - D^{n}_{i-\frac{1}{2},j}\mathbf{U}^{n}_{i-\frac{1}{2},j}\cdot\mathbf{E}^{\zeta}\Delta\zeta\right) - \\ &- \frac{\vartheta^2\Delta t^2}{F_0^2\Delta y^2}\left[\left(D^{n}_{i,j+\frac{1}{2}}\Delta\zeta\right)^2\left(h^{n+1}_{i,j+1}-h^{n+1}_{i,j}\right)\left(\mathbf{E}^{\zeta T}\cdot\mathbf{A}^{-1}\cdot\mathbf{E}^{\zeta}\right)_{i,j+\frac{1}{2}} - \right. \\ &\left. - \left(D^{n}_{i,j-\frac{1}{2}}\Delta\zeta\right)^2\left(h^{n+1}_{i,j}-h^{n+1}_{i,j-1}\right)\left(\mathbf{E}^{\zeta T}\cdot\mathbf{A}^{-1}\cdot\mathbf{E}^{\zeta}\right)_{i,j-\frac{1}{2}}\right] + \frac{\vartheta\Delta t}{\Delta y}\left[D^{n}_{i,j+\frac{1}{2}}\Delta\zeta\left(\mathbf{E}^{\zeta T}\cdot\mathbf{A}^{-1}\cdot\mathbf{G}^{n}\right)_{i,j+\frac{1}{2}} - \right. \\ &\left. - D^{n}_{i,j-\frac{1}{2}}\Delta\zeta\left(\mathbf{E}^{\zeta T}\cdot\mathbf{A}^{-1}\cdot\mathbf{G}^{n}\right)_{i,j-\frac{1}{2}}\right] + \frac{(1-\vartheta)\Delta t}{\Delta y}\left(D^{n}_{i,j+\frac{1}{2}}\mathbf{V}^{n}_{i,j+\frac{1}{2}}\cdot\mathbf{E}^{\zeta}\Delta\zeta - D^{n}_{i,j-\frac{1}{2}}\mathbf{V}^{n}_{i,j-\frac{1}{2}}\cdot\mathbf{E}^{\zeta}\Delta\zeta\right) = 0,\end{aligned} \tag{5.30}$$

where $\cdot$ represents the scalar product. (5.30) represents a linear system of n_x x n_y equations, where the unknowns are the values of the local free surface elevation $h^{n+1}_{i,j}$ and the coefficients are known and depend only on the flow field and flow depth at time step n. The system is symmetric and is solved using a conjugate gradient algorithm. We may note that the continuity equation is discretized in conservative form.

Once the free surface elevation is known, equations (5.17a-5.17b) are used in order to evaluate the flow velocities components $u^{n+1}_{i+\frac{1}{2},j,k}$ and $v^{n+1}_{i,j+\frac{1}{2},k}$. The vertical components $\widetilde{w}_{i,j,k+\frac{1}{2}}$ are

evaluated, once the horizontal component $u^{n+1}_{i+\frac{1}{2},j,k}$ and $v^{n+1}_{i,j+\frac{1}{2},k}$ are known, using a suitable finite-difference form of the continuity equation:

$$\widetilde{w}^{n+1}_{i,j,k+\frac{1}{2}} = \widetilde{w}^{n+1}_{i,j,k-\frac{1}{2}} - \frac{D^n_{i+\frac{1}{2},j} e^{\zeta_k} \Delta\zeta u^{n+1}_{i+\frac{1}{2},j,k} - D^n_{i-\frac{1}{2},j} e^{\zeta_k} \Delta\zeta u^{n+1}_{i-\frac{1}{2},j,k}}{\Delta x} - \\ - \frac{D^n_{i,j+\frac{1}{2}} e^{\zeta_k} \Delta\zeta v^{n+1}_{i,j+\frac{1}{2},k} - D^n_{i,j-\frac{1}{2}} e^{\zeta_k} \Delta\zeta v^{n+1}_{i,j-\frac{1}{2},k}}{\Delta y} - \frac{e^{\zeta_k}\Delta\zeta}{\Delta t}\left(D^{n+1}_{i,j} - D^n_{i,j}\right). \quad (5.31)$$

The above equation is applied to each water column, setting at the bed the no slip condition, $\widetilde{w}^{n+1}_{i,j,\frac{1}{2}} = 0$, and computing the values of $\widetilde{w}^{n+1}_{i,j,k+\frac{1}{2}}$ from the bed ($k = 1$) to the free surface ($k = n_z$).

5.3.2 Evaluation of the shear velocity and of the eddy-viscosity coefficients

The numerical computation requires estimations of local and instantaneous values of bed shear stress, which are used to compute the eddy viscosity, the bed load vector and the reference concentration which is needed in the boundary condition for the concentrations field at the bed. Recalling the definition of the shear velocity

$$u_* = \frac{1}{\sqrt{C_{f0}}U_0^*}\sqrt{\frac{|\tau^*|}{\rho}},$$

the shear velocity is evaluated, using (5.1), through the following expression:

$$u_* = \frac{1}{\sqrt{C_{f0}}}\sqrt{\sqrt{C_{f0}}\nu_T \frac{e^{-\zeta}}{D}\sqrt{\left(\frac{\partial u}{\partial\zeta}\right)^2 + \left(\frac{\partial v}{\partial\zeta}\right)^2}} \Rightarrow u_* = \frac{e^{-\zeta}N(\zeta)}{\sqrt{C_{f0}}}\sqrt{\left(\frac{\partial u}{\partial\zeta}\right)^2 + \left(\frac{\partial v}{\partial\zeta}\right)^2}\Bigg|_{\zeta^\tau},$$

where $N(\zeta)$ is the function proposed by Dean (1974) and reported in (4.8) and $\zeta^\tau = \ln(z^\tau)$, where z^τ is set equal to the equivalent roughness. Once the shear velocity is known, it is possible to evaluate the eddy viscosity in the following form:

$$\nu_T = u_* D N(\zeta).$$

5.3.3 Numerical scheme for the advection-diffusion equation

Due to the effect of settling velocity W_s, the vertical advection term in equation (5.10), $\left[e^{-\zeta}(\widetilde{w} - W_s)C_1\right]_{,\zeta}$, leads to relatively high values of the vertical Courant number $c_z = \frac{e^{-\zeta}(\widetilde{w}-W_s)}{\Delta\zeta}\Delta t$. In particular the Courant number is fairly large close to the bed, where the vertical grid spacing is small and the term $e^{-\zeta}$ attains high values. Under these conditions the numerical scheme doesn't perform satisfactorily, as typically occurs when advection is dominant. The overcome the above

difficulty a semi-analytical procedure for the solution of the advection-diffusion equation for the suspended sediment is introduced, in which the concentration field is splitted into two parts:

$$C = C_0 + C_1, \tag{5.32}$$

where C_0 is the solution of the following ordinary differential problem:

$$W_s C_0 + \frac{e^{-\zeta}}{D}\beta\sqrt{C_{f0}}\,|\mathbf{U}|\,P(\xi)\,C_{0,\zeta} = 0, \tag{5.33a}$$

$$C_0 = C_e, \qquad \zeta = \ln(a), \tag{5.33b}$$

and represents a Rouse-type vertical profile of concentration. More specifically, C_0 is the distribution that the concentration field would attain at equilibrium within a uniform flow characterised by the local and instantaneous flow conditions. Hence C_0 represents the contribution of the concentration field in phase with the local shear stress; assuming for the eddy diffusivity the relationship (4.9) and recalling that $\zeta = \ln\xi$, C_0 becomes:

$$C_0\left(\theta', d_s, R_p, a\right) = C_e\left(\theta', d_s, R_p, a\right) f\left(\zeta, G_1, G_2, a\right) \tag{5.34}$$

where the function $C_e(\theta', d_s, R_p, a)$ represents the reference concentration evaluated in terms of the local values hydrodynamic parameters. Furthermore the function f can be given the form:

$$f(\zeta, G_1, G_2, a) = \begin{cases} \left(\frac{a}{e^{\zeta}}\right)^{G_1} & \text{if} \quad \zeta < \ln(0.314) \\ \left(\frac{a}{0.314}\right)^{G_1}\left\{exp\left[-\left(e^{\zeta} - 0.314\right)\right]\right\}^{G_2} & \text{if} \quad \zeta \geq \ln(0.314) \end{cases} \tag{5.35}$$

having denoted by G_1 and G_2 the Rouse numbers:

$$G_1 = \frac{W_s}{0.35\sqrt{C_{f0}}u_*}, \tag{5.36a}$$

$$G_2 = \frac{W_s}{0.11\sqrt{C_{f0}}u_*}. \tag{5.36b}$$

Substituting equations (5.32) and (5.33a) into (5.10) we obtain the following equation for the component C_1:

$$\begin{aligned}(C_1 D)_{,t} + (DuC_1)_{,x} + (DvC_1)_{,y} + \beta e^{-\zeta}\left[(\widetilde{w} - W_s)C_1\right]_{,\zeta} + \\ -\gamma e^{-\zeta}\left(\frac{e^{-\zeta}}{D}\Psi_T C_{1,\zeta}\right)_{,\zeta} = \\ -(C_0 D)_{,t} - (DuC_0)_{,x} - (DvC_0)_{,y} - \beta e^{-\zeta}(\widetilde{w}C_0)_{,\zeta}\,. \end{aligned} \tag{5.37}$$

It is worth noticing that, through the right hand side of (5.37), the component C_0 produces a forcing term for C_1 which can be computed analytically evaluated through (5.34).

The boundary conditions associated with (5.37) are:

- the entrainment condition for the net flux of sediment at the reference level ($\zeta = \ln(a)$):

$$\sqrt{C_{f0}}\Psi_T \widetilde{\nabla} C_1 \cdot \hat{\mathbf{n}} + \sqrt{C_{f0}}\Psi_T \widetilde{\nabla}_h C_0 \cdot \hat{\mathbf{n}} - \left(\mathbf{u} - W_s\hat{\mathbf{k}}\right)\hat{\mathbf{n}} C_e = 0, \tag{5.38}$$

  where $\widetilde{\nabla}$ is the differential gradient operator, which is defined using (5.3b), (5.3c) and (5.3d), and $\widetilde{\nabla}_h$ is the horizontal gradient operator:

$$\widetilde{\nabla}_h = \left(\frac{\partial}{\partial x} - r_x\frac{e^{-\zeta}}{D}\frac{\partial}{\partial\zeta}, \frac{\partial}{\partial y} - r_y\frac{e^{-\zeta}}{D}\frac{\partial}{\partial\zeta}\right); \tag{5.39}$$

- vanishing sediment flux at the free surface ($\zeta = 0$):

$$\left(W_s C_1\hat{\mathbf{k}} + \sqrt{C_{f0}}\Psi_T\widetilde{\nabla}C_1 + \sqrt{C_{f0}}\Psi_T\widetilde{\nabla}_h C_0\right)\cdot\hat{\mathbf{n}}_s = 0. \tag{5.40}$$

The component C_1, which quantifies the spatial delay of sediment concentration with respect to the bed shear stress which is due to the advection and diffusion processes, is determined numerically through a mixed algorithm. In the horizontal directions we adopt the *Lax* scheme, in the form proposed by Leveque (1996); this numerical scheme is explicit, conservative and second order accurate in space; moreover it takes into account the diagonal fluxes with respect to the axis and cell orientation. hence, the method is stable within a wide range of Courant number:

$$\begin{aligned} c_x &= \frac{u\Delta t}{\Delta x} \leq 1, \\ c_y &= \frac{v\Delta t}{\Delta y} \leq 1. \end{aligned} \tag{5.41}$$

In the vertical direction an explicit scheme cannot be used because the vertical advection term

$\left[e^{-\zeta}(\widetilde{w}-W_s)C_1\right]_{,\zeta}$ leads to very high values of the vertical Courant number, as pointed out before. Hence, an implicit scheme is required. In the present work, due to the relatively high contribution of the vertical advective term, a linear combination of $up-wind$ and $central-difference$ algorithms is adopted in order to guarantee the stability, according to the following scheme

$$\delta\,(central)+(1-\delta)\,(up-wind)\,,$$

where the weighting coefficient δ is locally prescribed in order to warrant the stability of the scheme, though reducing the accuracy of the computation, according to the following relationship (Casulli and Greenspan, 1988):

$$\delta=\max\left(0,\min\left(1,\frac{2\gamma e^{-\zeta}P}{D\Delta\zeta\,|w-W_s|}\right)\right). \tag{5.42}$$

The above procedure allows one to include the $up-wind$ correction only where it is strictly necessary.

Using an explicit scheme for the horizontal fluxes, equation (5.37) reads:

$$\begin{aligned}(C_1D)_{,t}^{\,n+\frac{1}{2}}+\beta e^{-\zeta}\left[(\widetilde{w}-W_s)C_1\right]_{,\zeta}^{\,n+\vartheta}+\\ -\gamma e^{-\zeta}\left(\frac{e^{-\zeta}}{D}\Psi_T C_{1,\zeta}\right)_{,\zeta}^{n+\vartheta}=-\left(DuC_1\right)_{,x}^{\,n}-\left(DvC_1\right)_{,y}^{\,n}\\ -\left(C_0D\right)_{,t}^{\,n+\vartheta}-\left(DuC_0\right)_{,x}^{\,n+\vartheta}-\left(DvC_0\right)_{,y}^{\,n+\vartheta}-\beta e^{-\zeta}\left(\widetilde{w}C_0\right)_{,\zeta}^{\,n+\vartheta}\end{aligned} \tag{5.43}$$

Vertical terms in equation (5.43) are solved using the implicit scheme; hence we obtain:

$$\begin{aligned}&\frac{\Delta\zeta e^{\zeta_k}}{\Delta t}D_{i,j}^{n+1}C_{1,i,j,k}^{n+1}+\vartheta\left[\left(w_{i,j,k+\frac{1}{2}}^{n+\vartheta}-W_s\right)C_{1UP,i,j,k}^{n+1}-\left(w_{i,j,k-\frac{1}{2}}^{n+\vartheta}-W_s\right)C_{1DOWN,i,j,k}^{n+1}\right]-\\ &-\frac{\sqrt{C_{f0}}}{D_{i,j}^{n}}\frac{\vartheta}{\Delta\zeta}\left[\Psi_{T,i,j,k+\frac{1}{2}}e^{\zeta_{k+\frac{1}{2}}}\left(C_{1,i,j,k+1}^{n+1}-C_{1,i,j,k}^{n+1}\right)-\Psi_{T,i,j,k-\frac{1}{2}}e^{\zeta_{k-\frac{1}{2}}}\left(C_{1,i,j,k}^{n+1}-C_{1,i,j,k-1}^{n+1}\right)\right]=\\ &=\frac{\Delta\zeta e^{\zeta_k}}{\Delta t}D_{i,j}^{n}C_{1,i,j,k}^{n}-(1-\vartheta)\left[\left(w_{i,j,k+\frac{1}{2}}^{n+\vartheta}-W_s\right)C_{1UP,i,j,k}^{n}-\left(w_{i,j,k-\frac{1}{2}}^{n+\vartheta}-W_s\right)C_{1DOWN,i,j,k}^{n}\right]+\\ &+\frac{\sqrt{C_{f0}}}{D_{i,j}^{n}}\frac{(1-\vartheta)}{\Delta\zeta}\left[\Psi_{T,i,j,k+\frac{1}{2}}e^{\zeta_{k+\frac{1}{2}}}\left(C_{1,i,j,k+1}^{n}-C_{1,i,j,k}^{n}\right)-\Psi_{T,i,j,k-\frac{1}{2}}e^{\zeta_{k-\frac{1}{2}}}\left(C_{1,i,j,k}^{n}-C_{1,i,j,k-1}^{n}\right)\right]\\ &+\text{explicit terms}\end{aligned} \tag{5.44}$$

where $C_{1UP,i,j,k}$ and $C_{1DOWN,i,j,k}$ are evaluated using the mixed $up-wind$ and $central-differencing$

algorithm:

$$C_{1UP,i,j,k} = \frac{\delta}{2}\left(C_{1,i,j,k+1} + C_{1,i,j,k}\right) + (1-\delta)\begin{cases} C_{1,i,j,k+1} & \text{if } \left(w^{n+\vartheta}_{i,j,k+\frac{1}{2}} - W_s\right) < 0 \\ C_{1,i,j,k} & \text{if } \left(w^{n+\vartheta}_{i,j,k+\frac{1}{2}} - W_s\right) > 0 \end{cases} \tag{5.45a}$$

$$C_{1DOWN,i,j,k} = C_{1UP,i,j,k-1} \tag{5.45b}$$

When $\delta = 1$ the proposed scheme reduces to a central difference, while the condition $\delta = 0$ implies a first-order upwind differencing. Results of computational tests suggest that in our case δ is always very close to 1. Smaller values of δ can be expected for large values of sediment diameter, which leads to high value of the settling velocity W_s, or for low values of flow velocity, which may be the case of tidal flows during flow reversal. Notice that the decomposition (5.32) guarantees a good computational accuracy since the dominant component C_0 is determined through an analytical procedure. Using the explicit scheme for the horizontal fluxes and the implicit procedure for the vertical flux leads to the solution of simple three-diagonal algebraic systems, one for each water column. The solution for each system is obtained using the standard *LU* decomposition algorithm.

The above numerical procedure, which is summarised by (5.44) and (5.45), has been tested under different conditions, as discussed in the next sections. Notice that the standard test presented by many authors, which checks the ability of the model to reproduce the equilibrium concentration profiles in uniform flow, is here unnecessary because the proposed decomposition (5.32) automatically satisfies the above condition. In fact, in the case of uniform flow the contribution of C_1 vanishes and the concentration profile C=C_0 coincides with that evaluated analytically without any numerical approximation.

5.3.4 Exner equation

The continuity equation for the sediment (4.10) requires the definition of bed load components Q_{bx} and Q_{by}. They are evaluated in terms of the local values of Shields stress using (4.29a); furthermore, the effect of gravity is accounted for through the relationships (4.23a) and (4.23b). The continuity equation is solved using a finite difference algorithm

$$(1-p)\frac{\eta^{n+1}_{i,j} - \eta^{n}_{i,j}}{\Delta t} + Q_0\left(\frac{Q^{n+\vartheta}_{bx,i+\frac{1}{2},j} - Q^{n+\vartheta}_{bx,i-\frac{1}{2},j}}{\Delta x} + \frac{Q^{n+\vartheta}_{by,i,j+\frac{1}{2}} - Q^{n+\vartheta}_{by,i,j-\frac{1}{2}}}{\Delta y}\right) + \\ + \beta\left[\hat{\mathbf{k}} W_s C^{n+\vartheta}_{1,i,j,n_a} \cdot \hat{\mathbf{n}}\right] = 0, \tag{5.46}$$

where n_a represent the $\zeta - index$ at the reference level a where the "bed" boundary condition for the concentration is imposed. The quantities at time step $n+\vartheta$ are evaluated using the relationship (5.16):

$$(1-p)\frac{\eta_{i,j}^{n+1}-\eta_{i,j}^{n}}{\Delta t}+Q_0\left[\vartheta\left(\frac{Q_{bx,i+\frac{1}{2},j}^{n+1}-Q_{bx,i-\frac{1}{2},j}^{n+1}}{\Delta x}+\frac{Q_{by,i,j+\frac{1}{2}}^{n+1}-Q_{by,i,j-\frac{1}{2}}^{n+1}}{\Delta y}\right)+\right.$$
$$\left.(1-\vartheta)\left(\frac{Q_{bx,i+\frac{1}{2},j}^{n}-Q_{bx,i-\frac{1}{2},j}^{n}}{\Delta x}+\frac{Q_{by,i,j+\frac{1}{2}}^{n}-Q_{by,i,j-\frac{1}{2}}^{n}}{\Delta y}\right)\right]+,$$
$$+\beta\left[\hat{\mathbf{k}}W_s\left(\vartheta C_{1,i,j,N_a}^{n+1}+(1-\vartheta)C_{1,i,j,n_a}^{n}\right)\cdot\hat{\mathbf{n}}\right]=0. \qquad (5.47)$$

Since the values of Q_{bx}^{n+1} and Q_{by}^{n+1} depend on the local bed elevation $\eta_{i,j}^{n+1}$, which is still unknown at this stage, an iterative procedure is required.

5.3.5 Numerical procedure

The numerical procedure adopted in the solution for the flow field, the concentration field and the bed topography is the following:

- starting from the $n-th$ time step the trajectories and the velocity component $u_{i+\frac{1}{2}-a,\,j-b,k-d}^{n}$ and $v_{i-a,\,j+\frac{1}{2}-b,k-d}^{n}$ are evaluated;
- the vectors $\mathbf{G}_{i+\frac{1}{2},j}^{n}$, $\mathbf{G}_{i,j+\frac{1}{2}}^{n}$, the matrixes $\mathbf{A}_{i+\frac{1}{2},j}^{n}$, $\mathbf{A}_{i,j+\frac{1}{2}}^{n}$ and their inverse $\left(\mathbf{A}_{i+\frac{1}{2},j}^{n}\right)^{-1}$ and $\left(\mathbf{A}_{i,j+\frac{1}{2}}^{n}\right)^{-1}$ are computed ;
- the system (5.30) is solved using the conjugate gradient method;
- the horizontal components of the velocity, $u_{i+\frac{1}{2},j,k}^{n+1}$ and $v_{i,j+\frac{1}{2},k}^{n+1}$, are computed;
- the vertical component of the velocity $\widetilde{w}_{i,j,k+\frac{1}{2}}^{n+1}$ is computed;
- once the flow field is completely determined, the shear velocity and the eddy-viscosity coefficients are evaluated;
- the analytical contribution to the concentration field (5.34) is determined;
- the explicit fluxes for the concentration equation are evaluated;
- equation (5.44) is solved for each i, j;
- bed load components Q_{bx} and Q_{by} are determined;

- finally, exner equation (5.47) is solved;

All the quantities $D_{i+\frac{1}{2},j}$, $D_{i,j+\frac{1}{2}}$ are evaluated using linear interpolation.

5.4 Boundary conditions in the longitudinal direction

The numerical scheme requires two set of boundary conditions in the longitudinal direction, at the upstream and downstream end, respectively. These boundary conditions can be given in term of the free surface elevation of cells $(i=0,\ j=1..n_y)$ and $(i=n_x+1,\ j=1..n_y)$ or alternatively in term of the flow velocities at the cell border $\left(i=\frac{1}{2},\ j=1..n_y,\ k=1...n_z\right)$ and $\left(i=n_x+\frac{1}{2},\ j=1..n_y,\ k=1...n_z\right)$. The first type of boundary condition can be used when the free surface elevation is known, for example at the mouth of an estuary, where the tidal oscillation is imposed. The second type can be used when a barrier is present at the end of the channel and the velocity vanishes.

In the study of free bars formation in rivers and tidal channels the longitudinal extension of the computational domain is set equal to L_d^*. In the initial and final section of the channel periodic boundary conditions are imposed. Hence, the solution for each dependent variable can be given the standard Fourier representation:

$$f(x,y,\zeta,t)=\sum_{-n_x}^{n_x}\sum_{-n_y}^{n_y}F_{km}(\zeta,t)\exp\left(i\left(k\lambda x+m\frac{\pi}{2}y\right)\right), \tag{5.48}$$

where $\lambda=\frac{2\pi}{L_d^*/B^*}$ is the longitudinal wave-number, k indicates the longitudinal mode, m the transverse mode, the integers n_x and n_y denote the computational cells.

5.5 Numerical tests

5.5.1 Vertical velocity profile in uniform flow

The fist numerical test is designed to check the ability of the numerical model to reproduce the vertical velocity profile under uniform flow condition, namely the standard logarithmic profile suitably corrected to account for the wake effect. Adopting the relationship (4.8) for the eddy viscosity the analytical solution reads:

$$u_{analytical}(\xi)=\frac{\sqrt{C_{f0}}}{K_v}\left[\ln\left(\frac{\xi}{z_0}\right)+A\xi^2+B\xi^3\right] \tag{5.49}$$

where $A=1.84$, $B=-1.56$ and z_0 is computed as in (5.14).

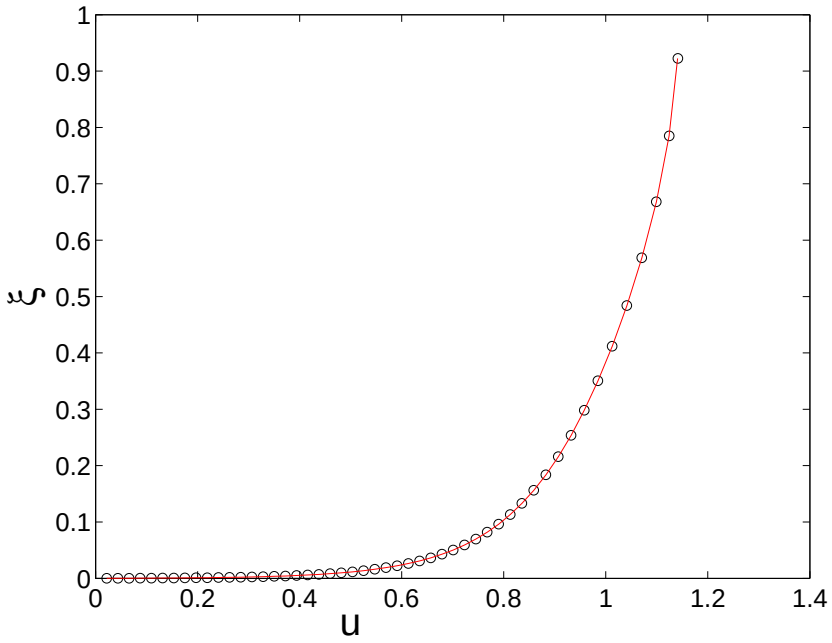

Figure 5.7: Vertical velocity profile under uniform flow condition: analytical solution (red solid line) and numerical solution (black dots). $\theta_0 = 1$, $R_p = 4$, $D_s = 10^{-5}$, $\lambda = 0.1$, $n_z = 50$.

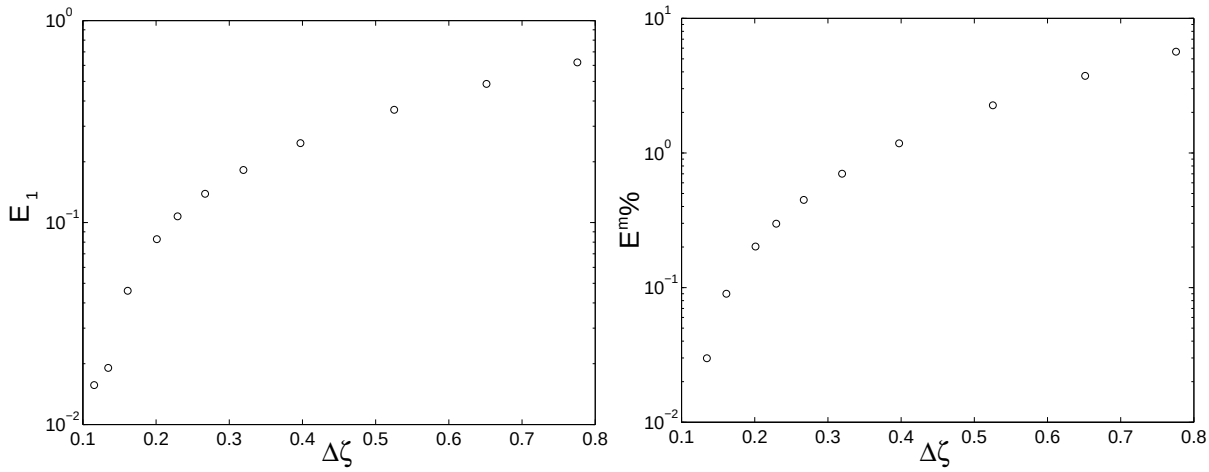

Figure 5.8: Numerical error in the estimate of velocity profile under uniform flow condition: norm E_1 (left), mean value (right). $\theta_0 = 1$, $R_p = 4$, $D_s = 10^{-5}$.

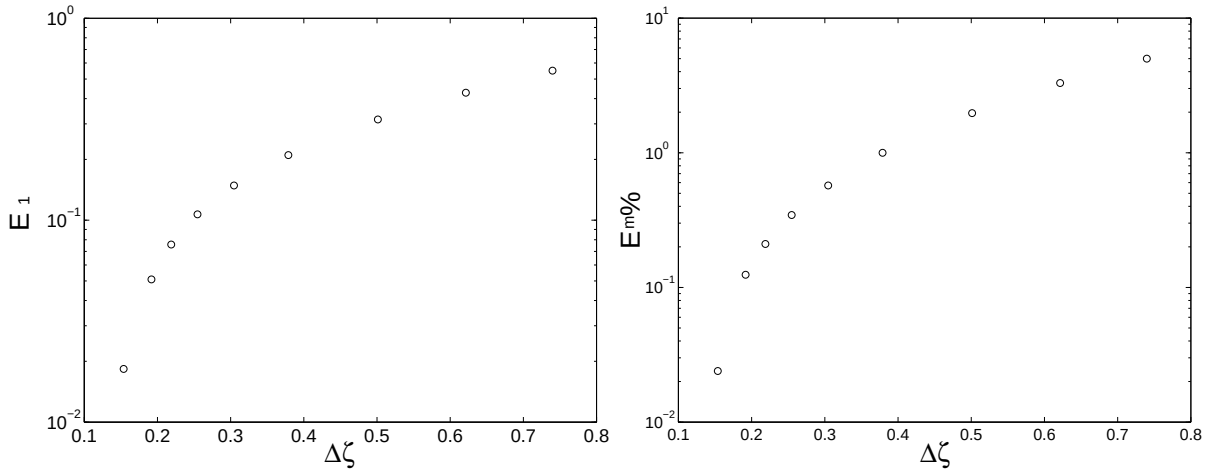

Figure 5.9: Numerical error in the estimate of velocity profile under uniform flow condition: norm E_1 (left), mean value (right). $\theta_0 = 1, R_p = 10, D_s = 2 \cdot 10^{-5}$.

The numerical model reproduces the vertical analytical velocity profile as shown in figure 5.7, where the solution is plotted versus the natural vertical coordinate ξ. It is worth noticing that the use of a logarithmic vertical coordinate implies a large number of numerical points close to the bed, which allows for a satisfactory reproduction of the velocity profile where the gradient is large.

A quantitative estimate of the numerical error is obtained in terms of the norm

$$E_1 = \sum_{k=1}^{n_z} \left| u_{numerical} - u_{analytical} \right|,$$

and the mean value of the truncation error

$$E_m\% = \frac{100}{n_z} \sum_{k=1}^{n_z} \left(u_{numerical} - u_{analytical} \right).$$

Comparisons are made for different choice of flow parameters: the results are reported in figure 5.8, for $\theta = 1, R_p = 4, D_s = 10^{-5}$, and in figure 5.9, for $\theta = 1, R_p = 10, D_s = 2 \cdot 10^{-5}$, where E_1 (left) and $E_m\%$ (right) are reported as functions of the vertical grid spacing.

We should note that the scheme is first order accurate; hence, the error is sufficiently small for values of $\Delta\zeta$ less than 0.2, that is n_z ranging between 30-40 depending on flow parameters.

5.5.2 Vertical velocity and concentrations profile with perturbed flow

The numerical model is then tested under non-uniform flow conditions. In this case only few solutions are available, because the complexity and the non-linear character of the momentum

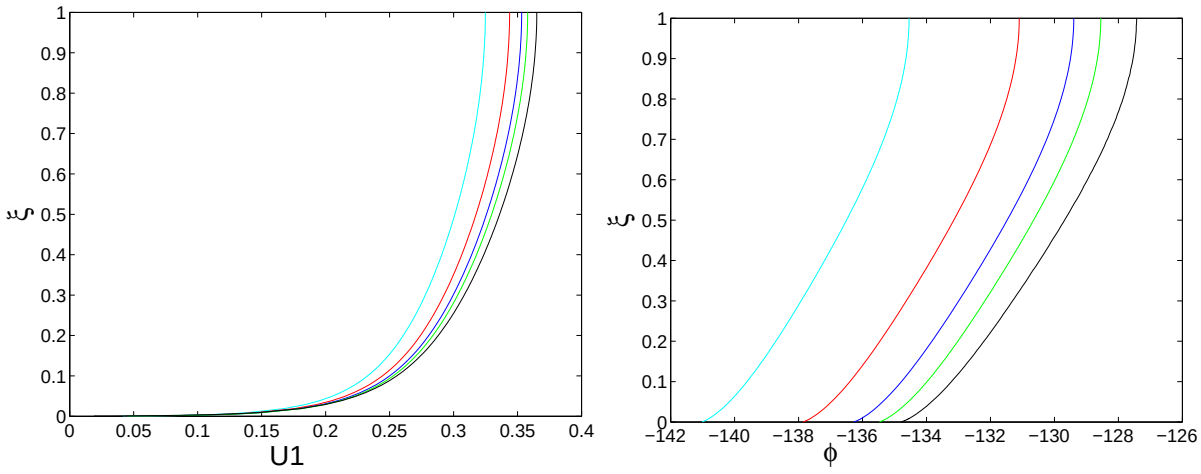

Figure 5.10: Comparison of present numerical results with the analytical solution of Tubino et al. (1999): vertical profiles of the amplitude $U1$ (left) and phase lag ϕ (right) of the perturbation of longitudinal velocity. $n_x = 16$ (cyan), $n_x = 32$ (red), $n_x = 64$ (blue), $n_x = 128$ (green) and the analytical solution (black). The phase lag Φ is measured with respect to the peak of bed elevation, the amplitude $U1$ is scaled with the dimensionless amplitude of bottom profile A_η. $\theta_0 = 1$, $R_p = 4$, $D_s = 10^{-5}$, $\lambda = 0.1$, $\beta = 15$, $n_y = 32$, $n_z = 100$, $A_\eta = 10^{-2}$.

equations do not allow to derive analytical solutions except for particular simplified conditions.

The validation of the numerical model, under non-uniform flow conditions, is made through the comparison of numerical results with the analytical solution of Tubino et al. (1999), which is valid for straight channels with a perturbed bottom whose amplitude is small with respect to the water depth.

5.5.2.1 The analytical solution of Tubino et al. (1999)

In this contribution the Authors consider an infinitely long straight channel with fixed banks and a varying bottom, subject to steady boundary conditions. The problem is cast in three dimensional form, in terms of longitudinal, transverse and vertical coordinates x, y and z , as described in Chapter 4; the solution for the flow and the concentration field is obtained analytically, using a perturbative approach which is based on the assumption that the ratio between the amplitude of bed perturbation and the mean flow depth is a small parameter. Under these conditions, when the bed is perturbed using a regular function like, for example a Fourier mode 11, all the dependent variables (flow velocity, free surface elevation, bed shear stress, concentration, etc.) display a perturbation with respect to the uniform basic state which exhibits the same regular structure, with different amplitudes and phase lags with respect to the bottom profile. A phase lag $\phi = 0$ corresponds to

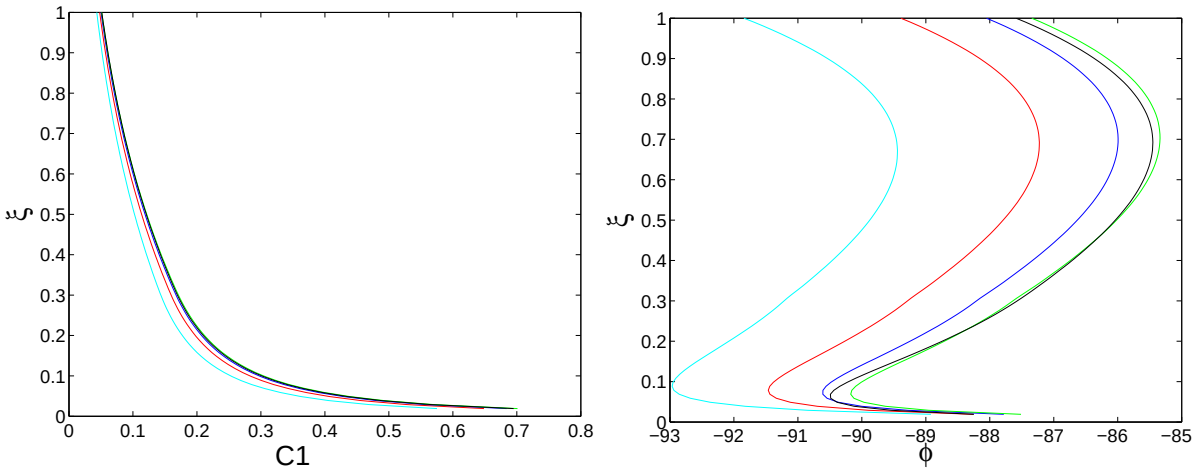

Figure 5.11: Comparison of numerical results with the analytical solution of Tubino et al. (1999): vertical profiles of the amplitude $C1$ (left) and phase lag ϕ (right) of the perturbation of the concentration. $n_x = 16$ (cyan), $n_x = 32$ (red), $n_x = 64$ (blue), $n_x = 128$ (green) and the analytical solution (black). The phase lag ϕ is measured with respect to the peak of bottom profile, the amplitude $C1$ is scaled with the dimensionless amplitude of bottom profile A_η. $\theta_0 = 1$, $R_p = 4$, $D_s = 10^{-5}$, $\lambda = 0.1$, $\beta = 15$, $n_y = 32$, $n_z = 100$, $A_\eta = 10^{-2}$.

a perturbation in phase with the bottom profile, that is the peak value of the variable is located at bar crest, while $\phi = 90^\circ$ corresponds to a perturbation whose maximum value is located where the bottom profile crosses the average bed level, i.e. where bed perturbation vanishes.

In figures 5.10, 5.11, 5.12 and 5.13 a comparison is pursued between the results of numerical computations and theoretical findings of Tubino et al. (1999). The comparison is given in terms of the amplitude (left) and phase lag (right) with respect to the peak of bottom profile of the perturbations of velocity and of suspended sediment concentration with respect to the uniform basic state.

The figure 5.14 shows that a satisfactory agreement with the analytical solution is achieved both at the free surface ($\xi = 1$) and close to the bed ($\xi = 0.01$). It is worth noticing that the accuracy of the numerical solution doesn't change even for relatively large values of bar wave-number λ (see figure 5.14), whence numerical diffusion is strongly inhibited by the numerical procedure adopted herein. Furthermore the numerical model correctly reproduces the shift of the peak of sediment concentration from negative to positive values of Φ as λ increases. The shift is larger at the free surface where advective terms are stronger.

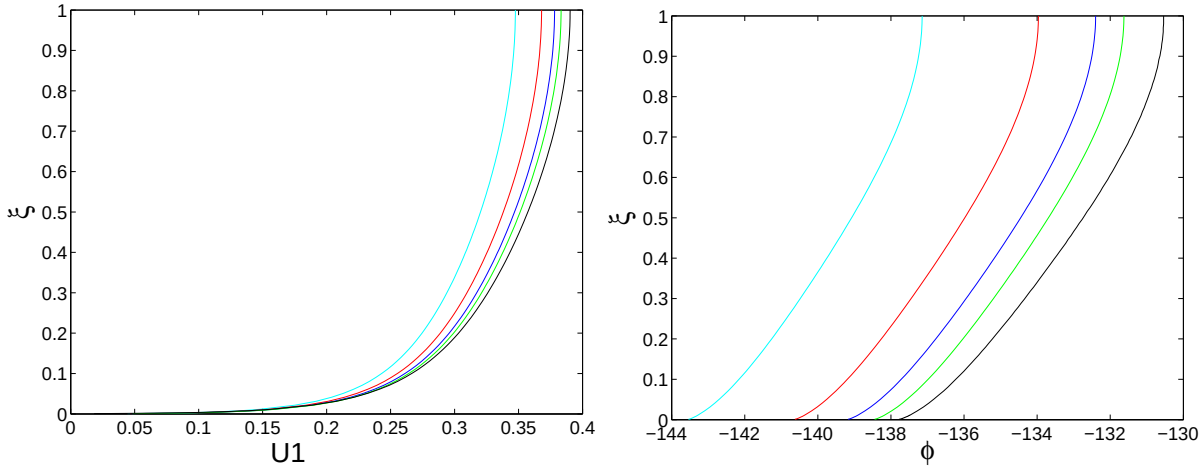

Figure 5.12: Comparison of numerical results with the analytical solution of Tubino et al. (1999): vertical profiles of the amplitude $U1$ (left) and phase lag ϕ (right) of the perturbation of the longitudinal velocity. $n_x = 16$ (cyan), $n_x = 32$ (red), $n_x = 64$ (blue), $n_x = 128$ (green) and the analytical solution (black). The phase lag ϕ is measured with respect to the peak of bottom profile, the amplitude $U1$ is scaled with the dimensionless amplitude of bottom profile A_η. $\theta_0 = 1$, $R_p = 10$, $D_s = 2 \cdot 10^{-5}$, $\lambda = 0.1$, $\beta = 15$, $n_y = 32$, $n_z = 100$, $A_\eta = 10^{-2}$.

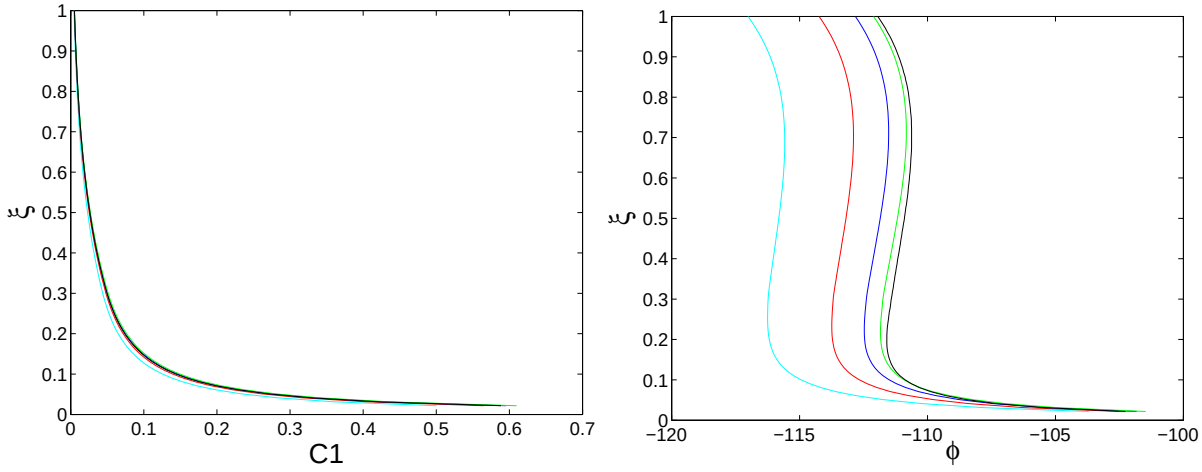

Figure 5.13: Comparison of numerical results with the analytical solution of Tubino et al. (1999): vertical structure of the amplitude $C1$ (left) and phase lag ϕ (right) of the perturbation of the concentration. $n_y = 16$ (cyan), $n_y = 32$ (red), $n_y = 64$ (blue), $n_y = 128$ (green) and the analytical solution (black). The phase lag ϕ is measured with respect to the peak of bottom profile, the amplitude $C1$ is scaled with the dimensionless amplitude of bottom profile A_η. $\theta_0 = 1$, $R_p = 10$, $D_s = 2 \cdot 10^{-5}$, $\lambda = 0.1$, $\beta = 15$, $n_x = 32$, $n_z = 100$, $A_\eta = 10^{-2}$.

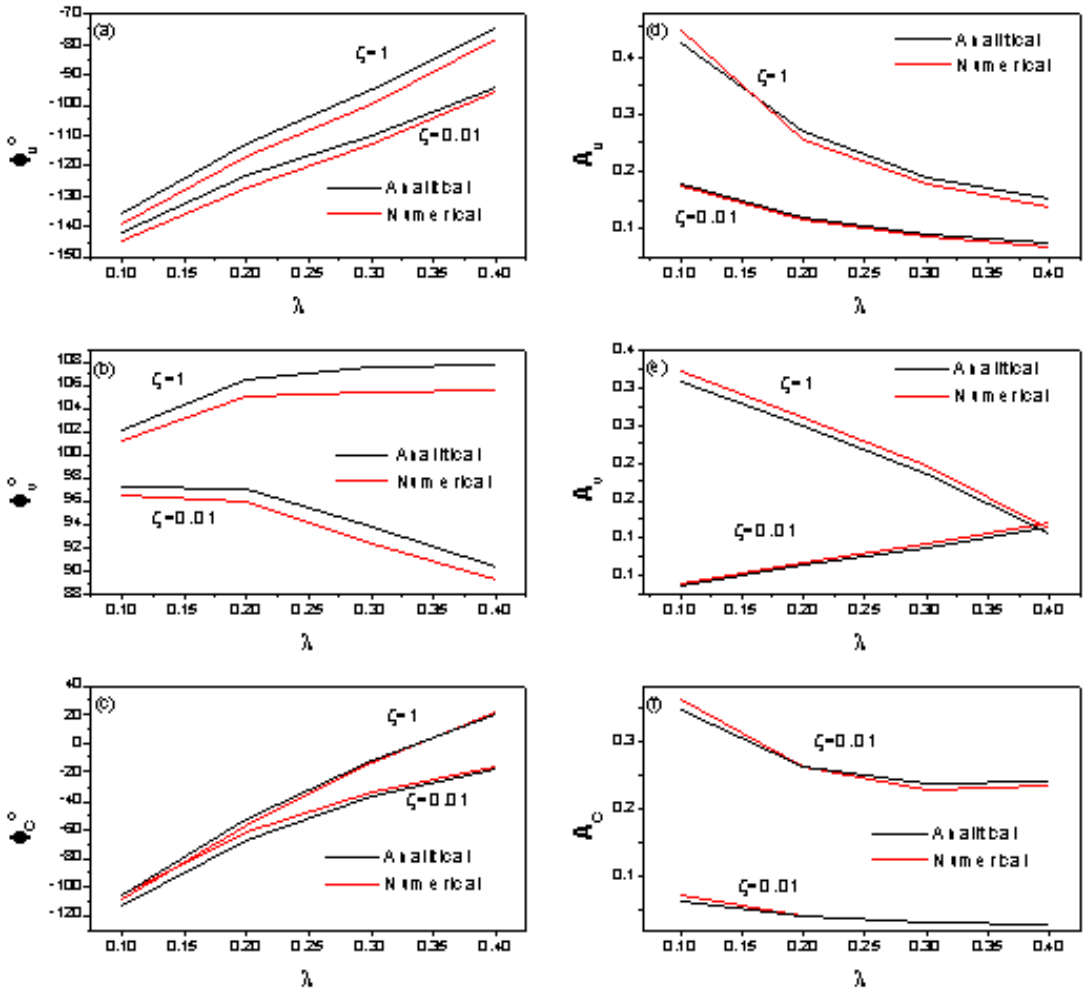

Figure 5.14: Comparison of numerical results with the analytical solution of Tubino et al. (1999): the phase and the amplitude of the perturbations of longitudinal (Φ_u, A_u) and transverse (Φ_v, A_v) components of velocity and of suspended sediment concentration (Φ_c, A_c) with respect to the wave-number λ. The phase lag Φ is measured with respect to the peak of bottom profile, the amplitude A is scaled with the dimensionless amplitude of bottom profile A_η. $\theta_0 = 1$, $\beta = 20$, $D_s = 10^{-5}$, $R_p = 4$, $n_z = 100$, $A_\eta = 10^{-2}$.

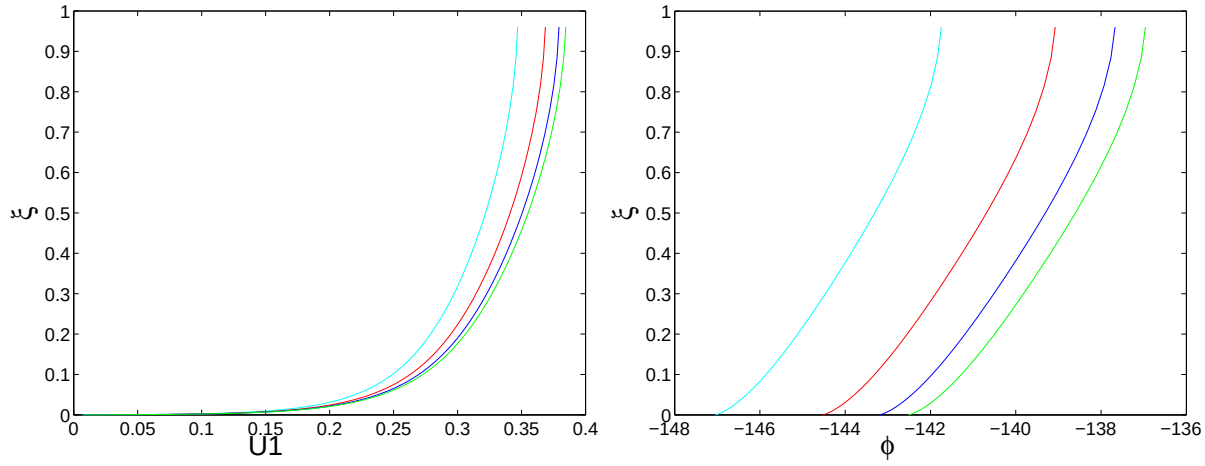

Figure 5.15: Dependence on the longitudinal grid spacing of the numerical results for the vertical profiles of the amplitude $U1$ (left) and phase lag ϕ (right) of the perturbation of the longitudinal velocity component: $n_x = 16$ (cyan), $n_x = 32$ (red), $n_x = 64$ (blue), $n_x = 128$ (green). The phase lag ϕ is measured with respect to the peak of bottom profile, the amplitude $U1$ is scaled with the dimensionless amplitude of bottom profile A_η. $\theta_0 = 1$, $R_p = 4$, $D_s = 10^{-5}$, $\lambda = 0.1$, $\beta = 15$, $n_y = 32$, $n_z = 100$, $A_\eta = 0.5$.

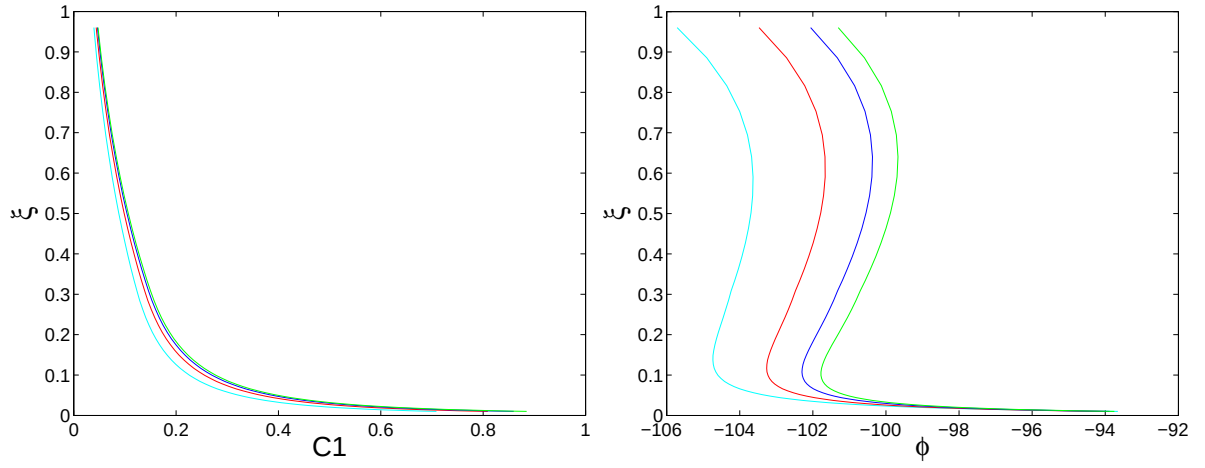

Figure 5.16: Dependence on the longitudinal grid spacing of the numerical results for the vertical profiles of the amplitude $C1$ (left) and phase lag ϕ (right) of the perturbation of the concentration: $n_x = 16$ (cyan), $n_x = 32$ (red), $n_x = 64$ (blue), $n_x = 128$ (green). The phase lag ϕ is measured with respect to the peak of bottom profile, the amplitude $C1$ is scaled with the dimensionless amplitude of bottom profile A_η. $\theta_0 = 1$, $R_p = 4$, $D_s = 10^{-5}$, $\lambda = 0.1$, $\beta = 15$, $n_y = 32$, $n_z = 100$, $A_\eta = 0.5$.

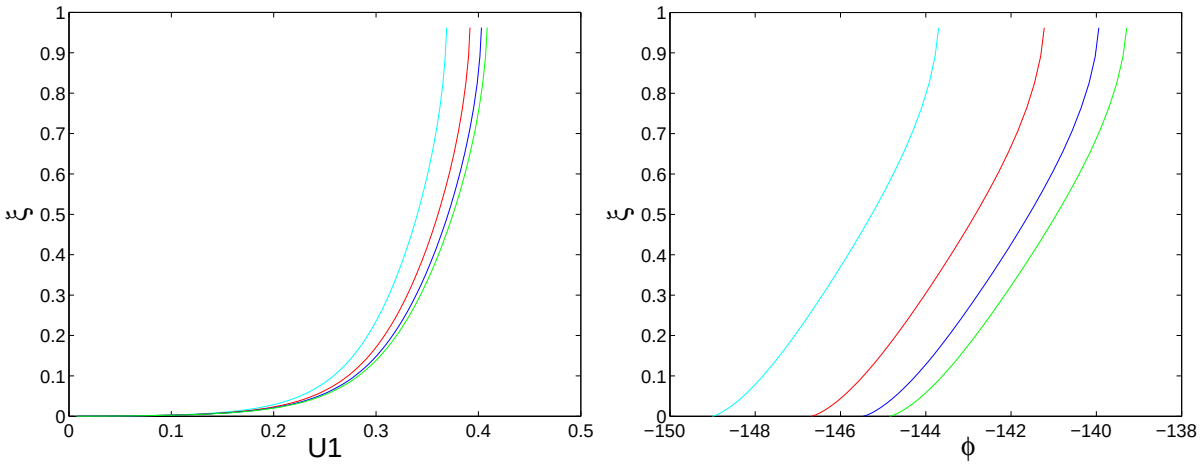

Figure 5.17: Dependence on the longitudinal grid spacing of numerical results for the vertical profiles of the amplitude $U1$ (left) and phase lag ϕ (right) of the longitudinal component of the velocity: $n_x = 16$ (cyan), $n_x = 32$ (red), $n_x = 64$ (blue), $n_x = 128$ (green). The phase lag ϕ is measured with respect to the peak of bottom profile, the amplitude $U1$ is scaled with the dimensionless amplitude of bottom profile A_η. $\theta_0 = 1$, $R_p = 10$, $D_s = 2 \cdot 10^{-5}$, $\lambda = 0.1$, $\beta = 15$, $n_y = 32$, $n_z = 100$, $A_\eta = 0.5$.

5.5.2.2 Results under non-linear conditions

The comparisons presented in section 5.5.2.1 are made between the numerical solution and the analytical linear solution, which is valid provided the amplitude of bed perturbation is small with respect to the mean flow depth. In this case the numerical solution smoothly converges to the analytical solution when the grid spacing is sufficiently small.

A check of the model behaviour under non-linear conditions is made using a regular bed perturbation with an amplitude equal to half flow depth. In this case the linear analytical solution is no longer valid; hence in figures 5.15, 5.16, 5.17 and 5.18, the test is made in terms of the numerical results obtained with different longitudinal grid spacing.

5.5.2.3 Comparison between the numerical scheme for the concentrations field with and without splitting

The semi-analytical scheme adopted in the present numerical model for the concentration field is based on the splitting of the concentration into two parts C_0 and C_1; the former is evaluated analytically, while the latter is computed numerically using the procedure described in section 5.3.3. One may wonder whether the splitting procedure does indeed improve the results with respect to the direct numerical solution of equation 5.10.

The comparison between the two approaches is made solving equation 5.10 with the same nu-

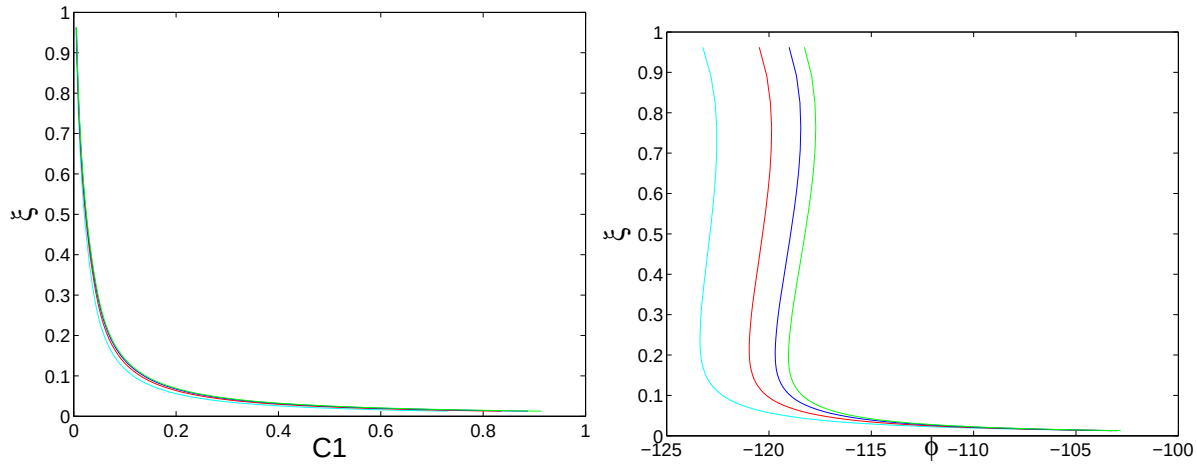

Figure 5.18: Dependence on longitudinal grid spacing of numerical results for the vertical profiles of the amplitude $C1$ (left) and phase lag ϕ (right) of the perturbation of the concentration: $n_x = 16$ (cyan), $n_x = 32$ (red), $n_x = 64$ (blue), $n_x = 128$ (green). The phase lag ϕ is measured with respect to the peak of bottom profile, the amplitude $C1$ is scaled with the dimensionless amplitude of bottom profile A_η. $R_p = 10$, $D_s = 2 \cdot 10^{-5}$, $\lambda = 0.1$, $\beta = 15$, $n_y = 32$, $n_z = 100$, $A_\eta = 0.5$.

merical scheme adopted for the splitting-method, suitable modified to take into account a different bed boundary condition, since when splitting is not introduced the whole sediment flux exchanged between the bed and the water column has to be considered.

The first numerical test is made in order to verify that the numerical scheme is able to reproduce the equilibrium Rouse profile (5.35) under uniform flow and sediment transport conditions; the result is reported in figure 5.19 for $\theta = 1$, $R_p = 4$, $D_s = 10^{-5}$, $n_z = 100$.

A comparison between the two approaches under non-uniform conditions is given in figure 5.20 where the numerical results are compared with the analytical solution of Tubino et al. (1999). We may notice that the amplitute and the perturbation of the concentration field is quite well reproduced by both models, while in terms of the phase lag ϕ the solution obtained using the splitting procedure adopted herein seems more accurate, in particular in the upper part of the water column.

A possible explanation of the above behaviour is the following. Using equation (5.37) the bed boundary condition is implicitly embodied in the right hand side, which is a forcing term for the unknown C_1, and is acting over the whole depth. On the contrary, using equation (5.10) the bed boundary condition is imposed at the reference level a, which corresponds to the numerical node n_a, and its effect over the depth is affected by the propagation of numerical approximations. The better performance of the splitting-method can be appreciated from the results reported in figure

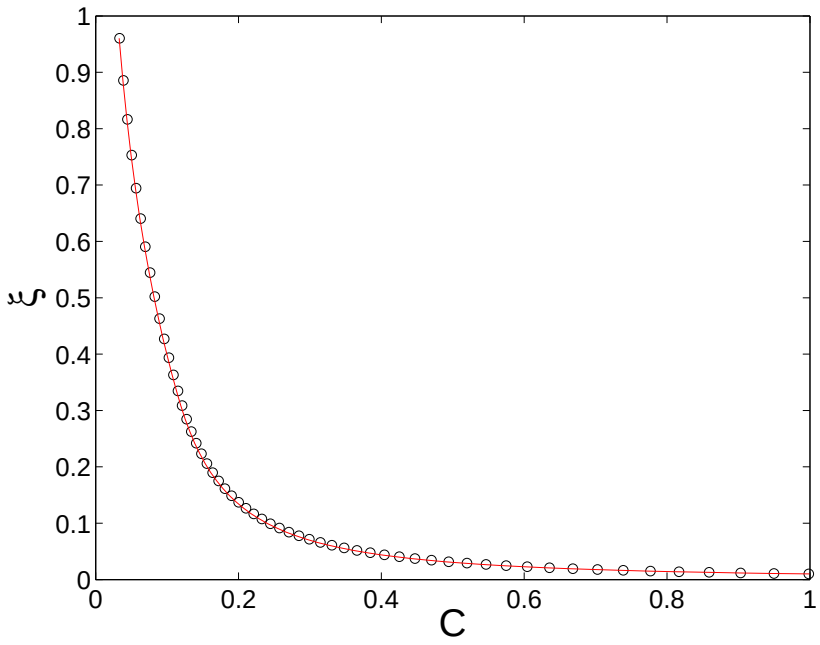

Figure 5.19: Vertical concentration profile under uniform flow and suspended load conditions evaluated without the splitting procedure: analytical solution (red solid line) and numerical solution (black dots). $\theta_0 = 1$, $R_p = 4$, $D_s = 10^{-5}$, $\lambda = 0.1$, $\beta = 15$, $n_z = 100$.

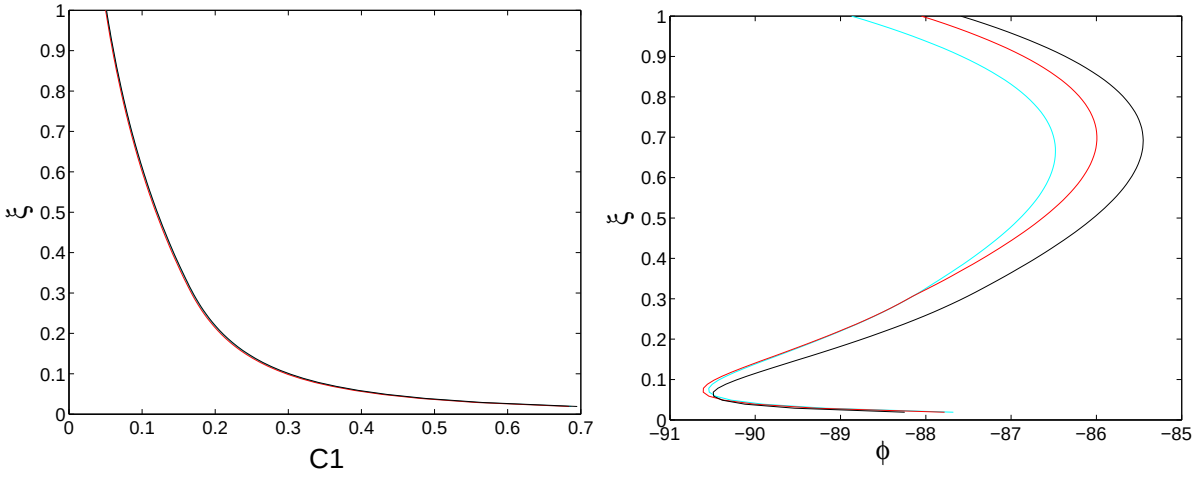

Figure 5.20: Comparison of the numerical results obtained with the splitting procedure or the direct solution of the equation for the concentration field: vertical profiles of the amplitude $C1$ (left) and phase lag ϕ (right) of the perturbation of the concentration. Analytical solution (black), splitting method (red) and direct solution method (cyan). The phase lag ϕ is measured with respect to the peak of bottom profile, the amplitude $C1$ is scaled with the dimensionless amplitude of bottom profile A_η. $\theta_0 = 1$, $R_p = 4$, $D_s = 10^{-5}$, $\lambda = 0.1$, $\beta = 15$, $n_x = 64$, $n_y = 32$, $n_z = 100$, $A_\eta = 10^{-2}$.

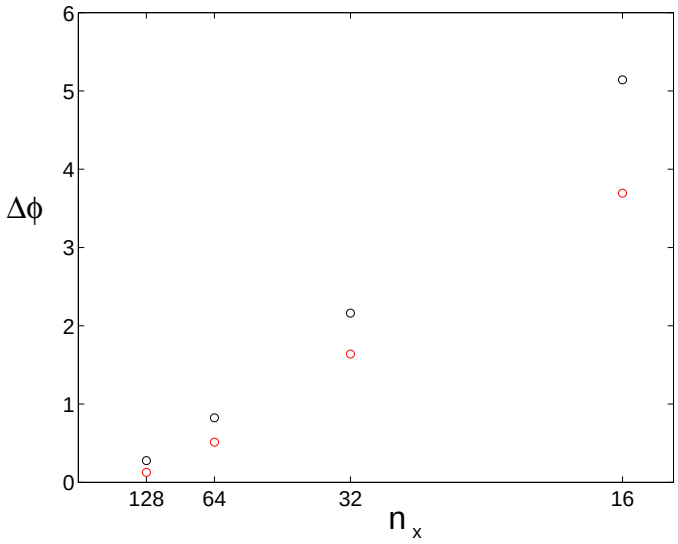

Figure 5.21: Comparison of the numerical results obtained with the splitting procedure or the direct solution of the equation for the concentration field: difference between the values of the phase lag predicted with the numerical solution with splitting (red dots) and without splitting (black dots) and those computed with the analytical solution. $\theta_0 = 1$, $R_p = 4$, $D_s = 10^{-5}$, $\lambda = 0.1$, $\beta = 15$, $n_y = 32$, $n_z = 100$, $A_\eta = 10^{-2}$.

5.21, where the difference between the analytical solution and numerical solutions

$$\Delta\phi = \frac{1}{n_z - n_a} \sum_{k=n_a}^{n_z} \left| \phi_{numerical} - \phi_{analytical} \right|,$$

is reported as a function of the longitudinal grid spacing.

Finally, it is worth noticing that the splitting-method better reproduces the typical delay of suspended load with respect to the local bottom shear stress, which affects crucially the stability of meso-scale bed forms as will be pointed out in the following chapter.

6 Meso-scale bed forms: an application to fluvial and tidal bars

In this chapter the formation of free bars in rivers and tidal channels is investigated using the 3D model presented in Chapter 5.

Bars induce a fairly regular sequence of scours and deposits along the channel. The spontaneous development of these bed-forms in almost straight reaches seems to require only the ability of the flow, when perturbed by a non uniform bottom profile, to enhance the altimetric form through selective processes of erosion and deposition. With reference to a regular bed wave this implies that flow and sediment transport must reach their maximum just upstream the crests so that deposition occurs at the crests and immediately downstream, leading to bed-forms whose amplitude increases in time while migrating in the downstream direction. The increase of the amplitude of bar fronts is mainly counteracted by the downward pull of gravity on sediment particles along transverse slopes. The latter effect becomes weaker as the width to depth ratio β of the channel increases, as transverse slopes are gentler when the transverse scale largely exceeds the vertical scale, like in natural channels. As a result a threshold value β_c exists below which free bars are not expected (and observed) to form.

The above scenario mainly applies to almost straight channels whose width is nearly constant and not exceedingly large, with well sorted sediments mainly transported as bed load. Under these circumstances various theoretical works (e.g. Blondeaux and Seminara, 1985; Fredsoe, 1978; Colombini et al., 1987; Struiksma and Crosato, 1989; Shimizu and Itakura, 1989) and a large number of experimental observations in laboratory flumes (e.g. Kinoshita, 1961; Chang et al., 1971; Ikeda, 1982a; Jaeggi, 1984; Fujita and Muramoto, 1985; Garcia and Niño, 1993) suggest the following picture.

The instability process which leads to bar formation is not strongly size-selective in the longitudinal direction, since different longitudinal modes within the unstable range are characterised by almost similar growth rate; on the contrary the transverse mode selected by the instability process depends strongly on the width ratio β of the channel: as a result, in gravel bed rivers bars generally display an alternating structure, while central bars or higher order transverse modes are not likely

Figure 6.1: Free bars in the Rio Branco, South America. (Image Science and Analysis Laboratory, NASA-Johnson Space Center. 18 Mar. 2005. "Earth from Space - Image Information." <http://earth.jsc.nasa.gov/sseop/EFS/photoinfo.pl?PHOTO=STS61C-33-72> 28 Apr. 2005)

to form spontaneously, in the absence of some forcing mechanism, unless the channel is fairly wide. Notice that predicted and observed values of the longitudinal wavelength of bars fall in the range of 5-12 channel widths. When the width ratio is not exceedingly large with respect to the critical value β_c and the channel is long enough to allow their development, regular trains of bars which migrate almost steadily in the downstream direction are invariably observed in flume experiments. The occurrence of such equilibrium configuration, which displays typical asymmetries like diagonal depositional fronts and deeper pools, is mainly the consequence of the "low degree" of non linearity displayed by the system, which is clearly witnessed by the scarcity of relevant components in the two dimensional Fourier representation of bottom profile at equilibrium (see figure 6.2). Theoretical results of Colombini et al. (1987) suggest that for values of β sufficiently close to β_c non-linear interactions lead to a periodic solution with steady equilibrium amplitude; however, non-linearity is weak in that the growth of higher harmonics is passively driven by the development of the fundamental alternate-bar mode. As suggested by Schielen et al. (1993) the above solution may be unstable and lead to quasi periodic solutions, though a straight reach with a length of few hundred widths is required to appreciate the associated modulation of bottom configuration.

Finally, as the width ratio β increases the nonlinear competition between different modes becomes stronger and may lead to the occurrence of complex transverse structures (Fujita, 1989; Colombini and Tubino, 1991). Moreover, local emergence of bar structures, which invariably occurs for

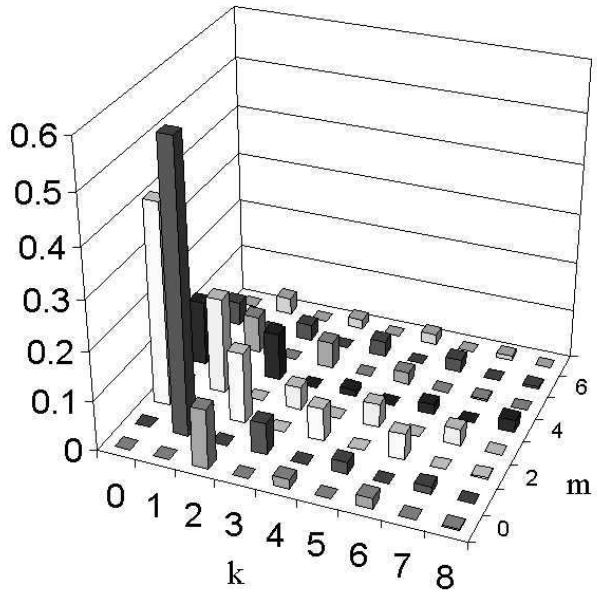

Figure 6.2: A typical Fourier spectrum of the equilibrium bar topography with dominant bed-load. *k* longitudinal modes, *m* transverse modes.

larger values of β, generally prevents the establishment of an equilibrium configuration.

6.1 Sand bars: linear theories

Bars are also encountered in sandy streams. Furthermore their occurrence in tidal channels and estuaries is widely documented in the geomorphological literature: in particular Dalrymple and Rhodes (1995) suggest that a wide spectrum of bar shapes is found depending upon channel sinuosity.

The question then arises on whether bars may develop spontaneously also in such systems where sediments are mainly transported as suspended load. In particular, does the instability process which governs bar development display similar features when suspension is dominant? Does a stable equilibrium configuration exist, like in gravel bed channels, whose occurrence doesn't require the presence of some forcing mechanism?

Flume observations on bar development with suspended load are rare and mostly refer to meandering channels (e.g., Ikeda and Nishimura, 1985). The experiments of Lanzoni (2000) in straight channels were not properly designed to reproduce transport conditions dominated by suspended load. However, in those runs where a certain amount of particles was put into suspension the formation of regular trains of bars was inhibited and bar development was found to be affected by

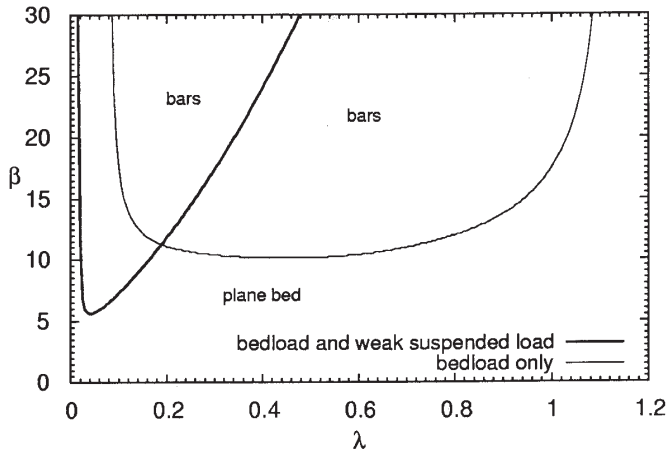

Figure 6.3: Marginal stability curves for bar formation: β is width ratio, λ is the longitudinal wave-number.

the interactions with small scale features, like ripples and dunes, such that the longitudinal bottom profiles were significantly distorted by high frequency components.

As for tidal free bars, laboratory observations are not known to the present authors. On the other hand, field observations suggest that, in spite of the oscillating character of the flow and of the dominant suspended load, the dependence of bar wavelength on channel width in tidal environments seems to conform to the trend exhibited by alternate bars in gravel bed rivers (Dalrymple and Rhodes, 1995). However, ascertaining the role played by several forcing mechanism is particularly relevant for tidal networks. In fact, such systems often display over a length of few kilometres the same degree of geometrical non uniformity which is typically distributed over an entire river basin; hence, bar development in tidal channels may be strongly influenced by forcing factors, like the finite length and the changing geometry of the channel as well as the interaction with adjacent channels and the exchange of flow and sediments with tidal flats.

Theoretical results for bar formation in both sandy rivers (Tubino et al., 1999) and tidal channels (Seminara and Tubino, 2001) have been recently derived within the context of a linear framework. Both analysis refer to an infinitely long straight channel, with bed composed by a fine homogeneous sediment; they essentially differ for the different character of the basic flow whose stability is investigated: the basic flow is steady in Tubino et al. (1999), while the channel is subject to the propagation of a tidal wave in the analysis of Seminara and Tubino (2001). In particular, in the latter work, at the leading order of approximation, local inertia and spatial variations of tidal wave are found to be negligible at the scale of bars: hence, free bars feel the tidal wave as an oscillatory longitudinally uniform flow. The reader is referred to the above papers for further details on the structure of the solution. It is important to recall here that both solutions display several distinc-

tive features with respect to the case of gravel beds. In fact, as Shields parameter increases the threshold value β_c for bar formation tends to vanish as a result of the vanishing role of the stabilising contribution of gravity. When suspended load is dominant bar stability crucially depends on the longitudinal wavelength of bars. In particular, shorter bars are damped while longer bars are enhanced, which implies a distortion of marginal curves for bar formation as qualitatively reproduced in figure 6.3. In tidal channels the above distortion is less pronounced due to the variation of Shields stress during the tidal cycle. As a result, when suspended load becomes dominant bar perturbations falling within the most unstable range of bed-load dominated gravel rivers are damped while alternate bars as long as 25-30 channel widths are expected to form, which correspond to dimensionless bar wave-numbers λ ranging about 0.1-0.12. Also notice that, while in the case of dominant bed load the alternate bar mode is the fundamental transverse mode in a wide range of values of β, the linear theory of Tubino et al. (1999) suggests that in sandy streams various transverse modes are characterised by almost similar growth rates, as shown in figure 6.4. These results can be interpreted as an indirect suppressing effect of suspended load on bar stability in that a long straight reach is required to allow for the development of regular trains of bars: for channel widths of the order of few hundred meters a river reach should keep straight and relatively uniform over a length of several tens of kilometres. Also notice that uniformity of channel geometry seems to be an essential requirement for the spontaneous development of migrating bars: in fact, results of theoretical and experimental investigations (Kinoshita and Miwa, 1974; Tubino and Seminara, 1990; Whiting and Dietrich, 1993; Repetto and Tubino, 1999) suggest that spatial variations of curvature and channel width may strongly inhibit the migration of free bars along the channel. The results of figure 6.4 suggest that to determine the finite amplitude structure of bed topography, a weakly non linear analytical approach, like that introduced by Colombini et al. (1987), may turn out to be inadequate when suspension is dominant. In this case bar development is more likely to be controlled by the simultaneous amplification and non-linear competition between several unstable transverse mode. The resulting strong non linearity may imply that local emergence of bar structure may occur even for values of β relatively close to the critical value β_c; furthermore, the system may not reach an asymptotic equilibrium configuration displaying the simple bed structure depicted in figure 6.2. Under these circumstances one should resort to a fully non linear numerical approach like that proposed in Chapter 5.

6.2 The steady case

According to the linear results of Tubino et al. (1999) the contribution of suspended load to the growth rate of bars is mainly related to the phase lag of the longitudinal component of sediment flux with respect to bottom shear stress. The phase lag mainly arises from the effect of longitudinal

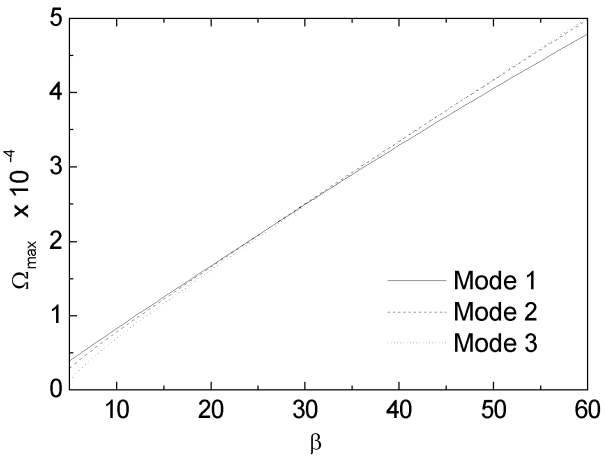

Figure 6.4: The maximum growth-rate Ω_{max} is plotted versus the width ratio β for different transverse modes.

convection, whose effect is larger for shorter wavelengths. Hence, as λ increases the contribution of suspended load to the growth rate shifts from positive to negative as the peak of longitudinal transport exceeds bar crests: under this condition sedimentation occurs at bar pools and bar topography is damped. Linear analyses also suggest that the prediction of marginal stability conditions under suspended load dominated conditions is very sensitive to the model adopted and strongly depends on the ability of the model to reproduce adequately convective effects.
Results of numerical simulations under fully non-linear conditions suggest that bar development with suspended load is similar to that observed under bed-load dominated conditions, provided the aspect ratio β is fairly close to the threshold value for bar formation. Under these conditions an equilibrium configuration is achieved, which mainly arises from the damping effect of higher harmonics on the growth of the fundamental alternate-bar mode, as found by Colombini et al. (1987) for dominant bed-load. The resulting bed topography is still characterised by the dominance of the first alternate mode, though the amplitude of higher harmonics is typically larger when suspended load is present: in particular, second order transverse modes (central bars modes) may attain an amplitude which is comparable to that of alternate bars. This is shown in figure 6.5 where the time development of the amplitude of the leading transverse modes of the Fourier representation of bed topography is reported: 11 denotes the alternate bar mode, while $02 + 22$ are second order transverse modes which represent, respectively, a transverse deformation of the bed, in the form of a central deposit which doesn't display any longitudinal variation, and a central bar mode with a longitudinal wavelength equal to half the length of the fundamental 11 mode.

Figure 6.5 allows for a comparison between the results obtained under bed-load dominated

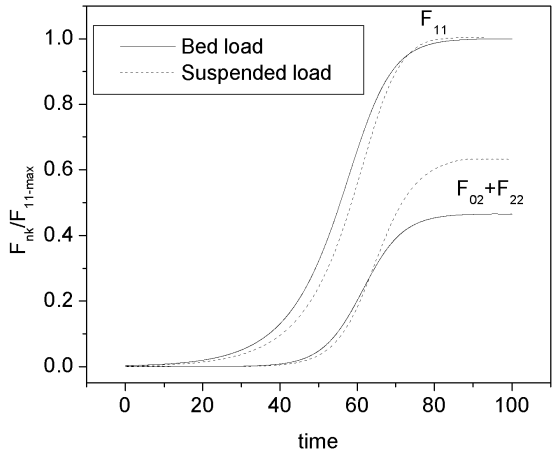

Figure 6.5: Comparison between the time development of the amplitude of the leading components of bar topography under bed-load dominated conditions $\theta_0 = 0.1$, $\beta = 20$, $D_s = 10^{-2}$, $R_p = 11000$ and with dominant suspended load $\theta_0 = 1$, $\beta = 15$, $D_s = 10^{-5}$, $R_p = 4$.

conditions and those with dominant suspended load: numerical simulations refer to different values of reference dimensionless parameters, though they are similar in terms of the distance of β from the critical conditions for bar formation. Also notice that both the amplitudes of the Fourier components and time are scaled in the figure using the amplitude and the growth rate of the fundamental 11 component, respectively. A large number of significant components characterises the spectrum of bed topography at equilibrium when suspended load is dominant, as shown in figure 6.6.

As β increases non-linear interactions, which are stronger with suspended load, lead to complex bed configurations; numerical results suggest that an equilibrium configuration is no longer achieved; furthermore, the superposition of transverse modes soon leads to local emergence of bar structures. Figure 6.7 suggests that for given value of particle Reynolds number the role of second order transverse modes increases for higher values of Shields stress, that is of the intensity of suspended load (the amplitudes of the Fourier components and the time are scaled as in figure 6.5). The values of the width ratio β_{em} at which local emergence of bar structure occurs in numerical computations are plotted in figure 6.8 versus Shields stress θ, for different values of particle Reynolds number R_p. Results are given in terms of the relative distance of the condition of bar emergence from the critical condition for bar formation. Notice that the role of suspended load increases as θ increases and R_p decreases. It appears that when suspended load is large the local emergence of bar structure, which may imply the formation of central islands and the transition to non-migrating complex bed-forms, may occur at relatively low values of width ratio.

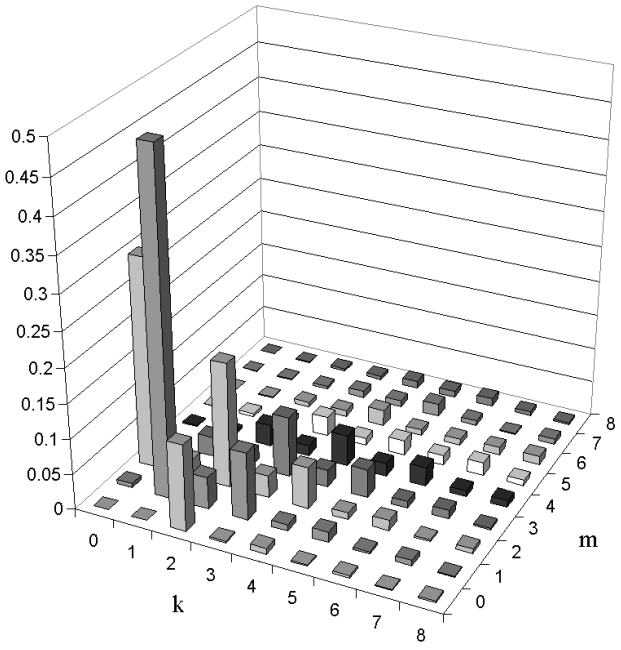

Figure 6.6: The Fourier spectrum of the equilibrium bar topography with dominant suspended load: k denotes longitudinal modes, m transverse modes $\theta_0 = 1.25$, $\beta = 12$, $D_s = 2 \cdot 10^{-5}$, $R_p = 10$.

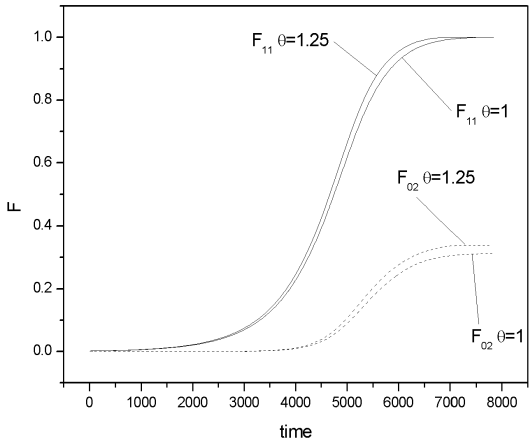

Figure 6.7: Time development of the amplitude of the leading components of the Fourier representation of bed topography for different values of Shields stress $\beta = 11$, $D_s = 2 \cdot 10^{-5}$, $R_p = 10$.

Equilibrium bed topographies obtained for values of the aspect ratio β falling below the critical values for bar emergence are given in figures 6.9-6.15 for different values of the dimensionless parameters. Figures 6.9-6.12 are obtained with the particle Reynolds number $R_p = 10$, which corresponds to a dimensional grain size of $0.2\,mm$. In this case the topography displays a diagonal arrangement of bar fronts like that typically observed in the case of gravel bed river bars. As the role of suspended load increases and becomes dominant bar pattern changes as shown in figures 6.13-6.15 where a value of $R_p = 4$ has been used, which corresponds to a grain size of $0.1\,mm$ (the reader is referred to figure 6.16 where the effect of R_p on the ratio of suspended to bed load is reported). In this case diagonal fronts are nearly absent and downstream slopes become gentler.

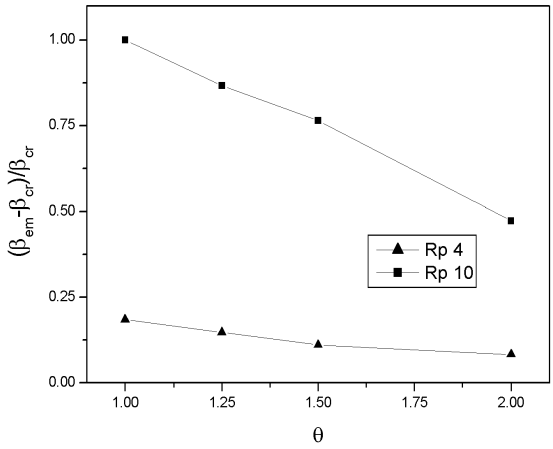

Figure 6.8: The computed values of width ratio β_{em} at which local emergence of bar structure is observed are plotted versus Shields stress for two different values of particle Reynolds number.

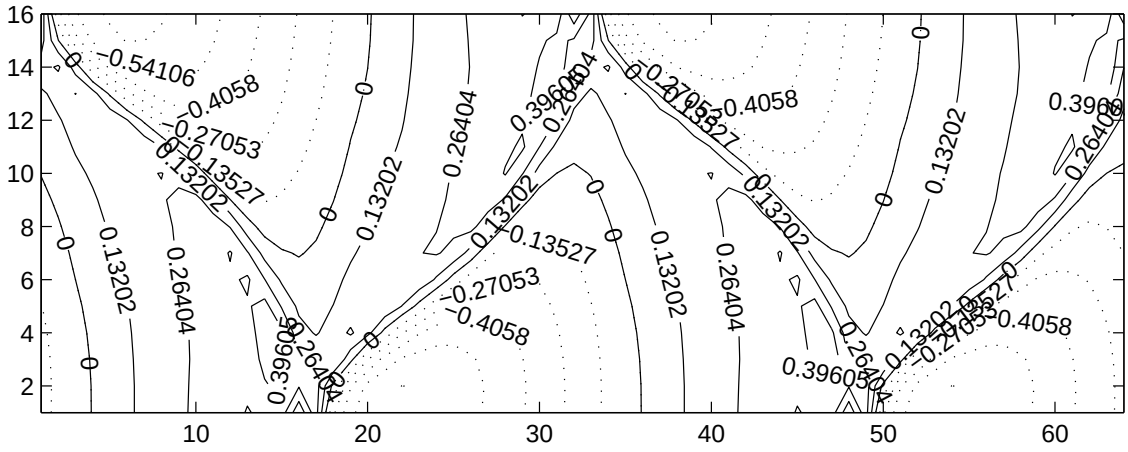

Figure 6.9: The equilibrium bed topography for $\theta_0 = 1.25$, $R_p = 10$, $\beta = 12$, $D_s = 2 \cdot 10^{-5}$.

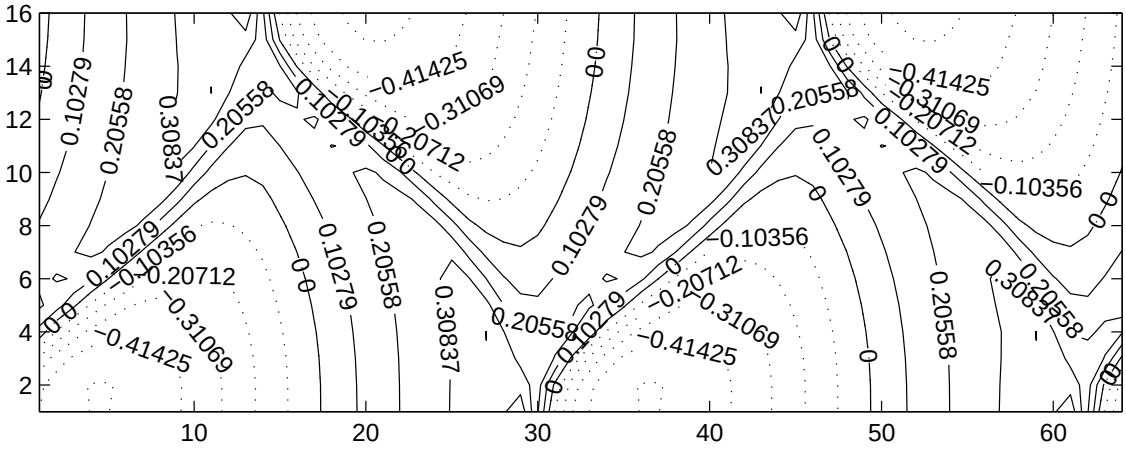

Figure 6.10: The equilibrium bed topography for $\theta_0 = 1.5$, $R_p = 10$, $\beta = 13$, $D_s = 2 \cdot 10^{-5}$.

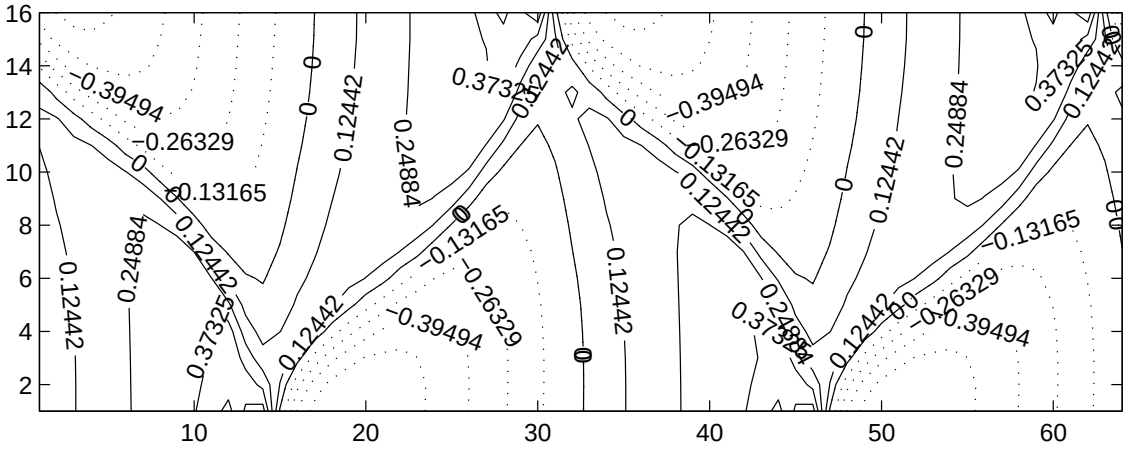

Figure 6.11: The equilibrium bed topography for $\theta_0 = 1$, $R_p = 10$, $\beta = 10$, $D_s = 10^{-5}$.

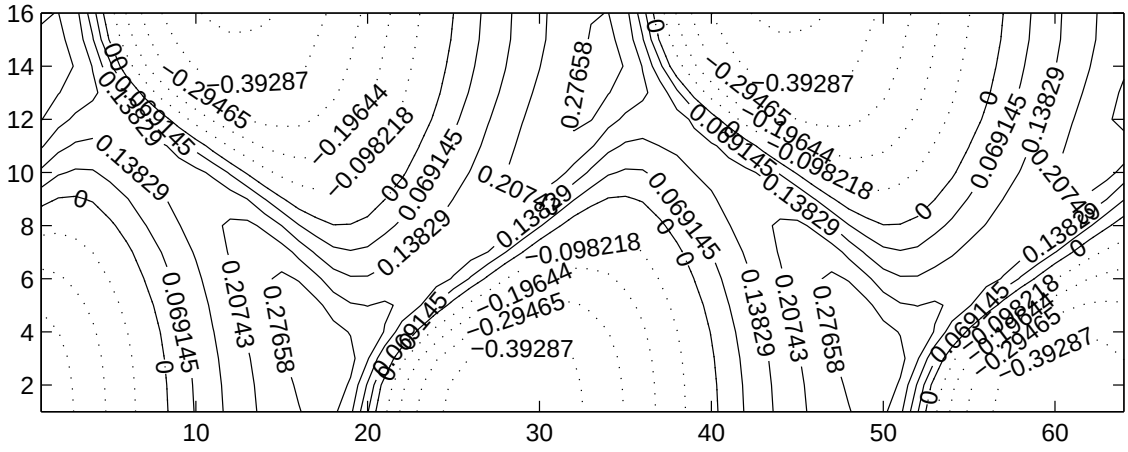

Figure 6.12: The equilibrium bed topography for $\theta_0 = 2$, $R_p = 10$, $\beta = 12$, $D_s = 2 \cdot 10^{-5}$.

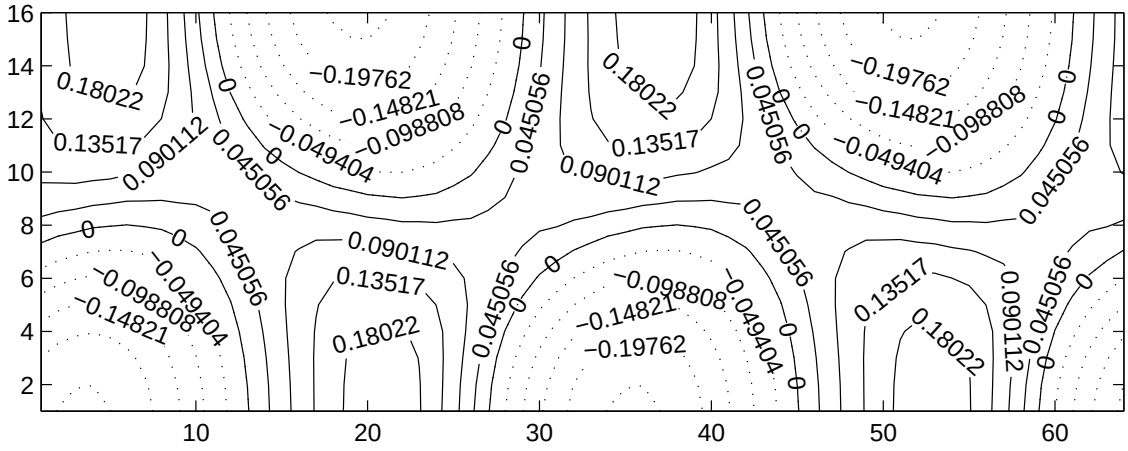

Figure 6.13: The equilibrium bed topography for $\theta_0 = 1.5$, $R_p = 4$, $\beta = 14$, $D_s = 10^{-5}$.

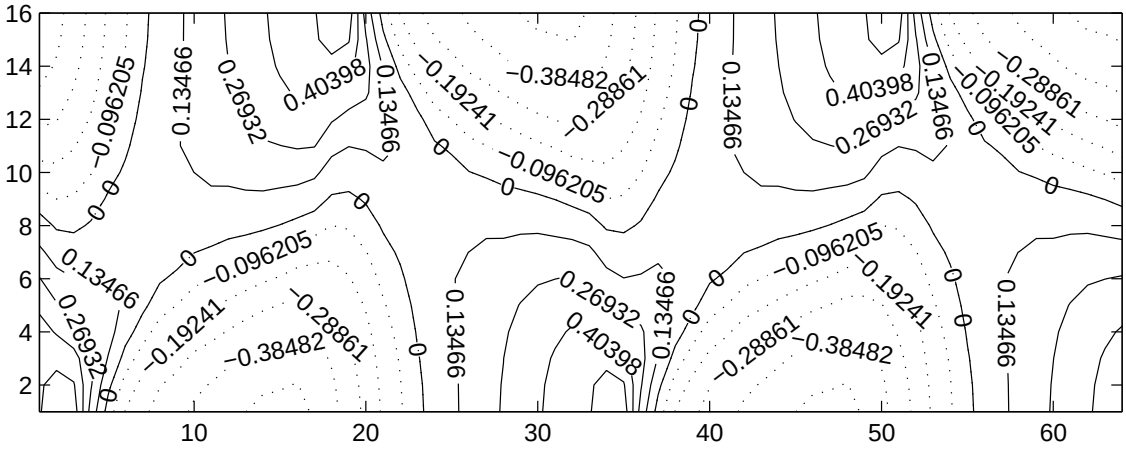

Figure 6.14: The equilibrium bed topography for $\theta_0 = 1$, $R_p = 4$, $\beta = 15$, $D_s = 10^{-5}$.

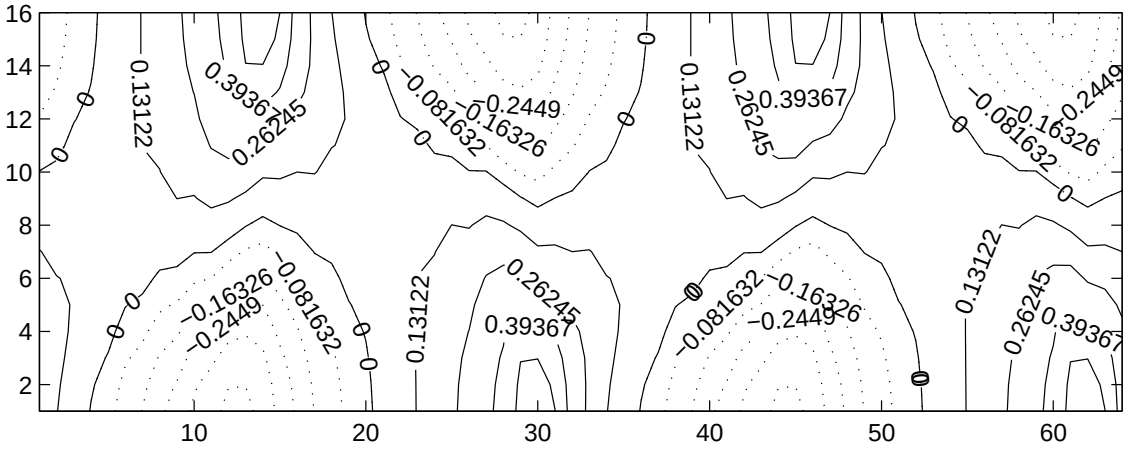

Figure 6.15: The equilibrium bed topography for $\theta_0 = 2$, $R_p = 4$, $\beta = 12$, $D_s = 10^{-5}$.

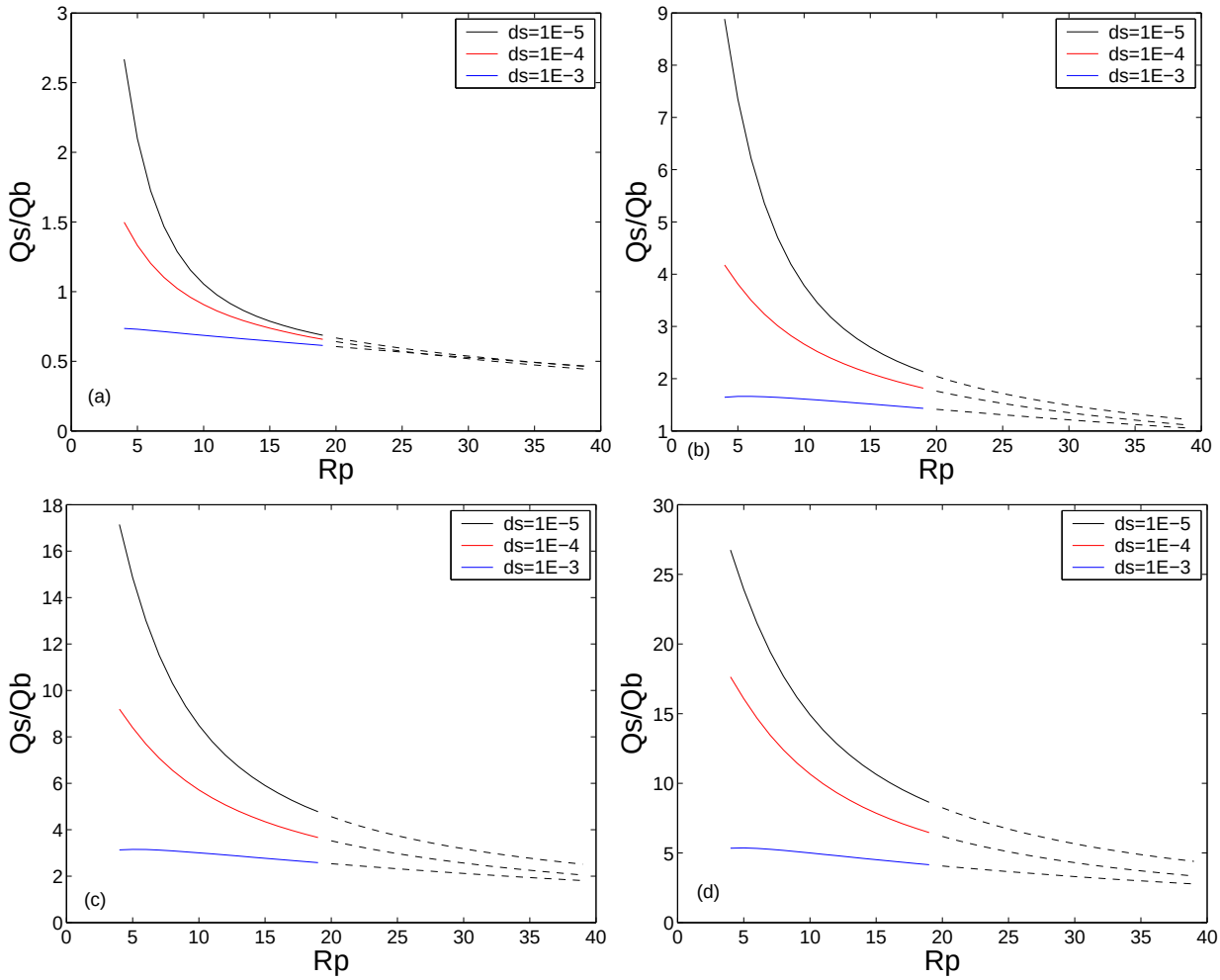

Figure 6.16: Ratio between the suspended load and the bed load, as a function of the sediment particle Reynolds number R_p, for different values of the Shields stress $\theta = 0.5$ (a), $\theta = 1$ (b), $\theta = 1.5$ (c), $\theta = 2$ (d). The computation is performed using the standard closure relationships of van Rijn (1984), which are not valid for the higher values of R_p.

6.3 The unsteady case

The application of the present numerical model to bar development in tidal channels requires the introduction of a time dependent basic flow. Within the context of a local analysis, in which a channel reach of the order of few channel widths is considered, the above flow can be assumed to be a sequence of locally uniform flows with a constant depth and a sinusoidal time oscillation of the mean shear stress. Following this approach, which has been also used in the analytical solution of Seminara and Tubino (2001), the interaction between the local-scale and the large scale behaviour is neglected. The basic state adopted herein may describe adequately the flow field in channels in which the tidal range is fairly low with respect to the mean flow depth, like the main channels of Venice lagoon ($D_0 > 10\,m$, tidal amplitude $a_0 < 0.5\,m$).

Results obtained in this case suggest that the tidal averaged celerity of bed forms vanishes, due to the imposed symmetry between the ebb and the flood phase. The bottom evolution is the result of the local unbalance between the sediment pick-up and the deposition flux near the bed. The process is related both to the effect of suspended load transport, which takes place on a time scale equal to

$$T_s = \frac{(1-p)\,D_0^*}{W_s^* S_0^*}, \tag{6.1}$$

and of bed load transport, whose time scale is

$$T_b = \frac{(1-p)\,B_0^* D_0^*}{\sqrt{g\Delta d_s^{*3}}}. \tag{6.2}$$

We may notice that even under suspended load dominated conditions, the effect of bed load cannot be neglected because it always affects substantially the behaviour of bed-forms.

Results of numerical simulations suggest that two main behaviours can be recognised, depending upon the relative values of the time scale of bed development and the tidal period. When the time scale of bed development is shorter than the tidal period, as it is typical of relatively coarse particles, the main transport mechanism is the bed load. In this case bed forms migrate slowly during the tidal period, but on the average their celerity vanishes, as shown in figure 6.17 where the bed topography corresponding to quarters of the tidal cycle is plotted.

In the second case, namely when the time scale of bed development is much longer than the tidal period, as it is typical of fine sediment tidal channels, suspended load is dominant, the bed elevation η is a slow time variable and bed forms don't migrate during the tidal cycle, display symmetrical shapes and mainly grow close to the peak values of the flood and ebb phases, as shown in figure 6.19. Notice that in this case residual effects are absent due to the imposed symmetry of the basic flow. Numerical results are in fairly good agreement with field observations in the Severn estuary (Harris and Collins, 1985), which suggest that larger bed-forms such as

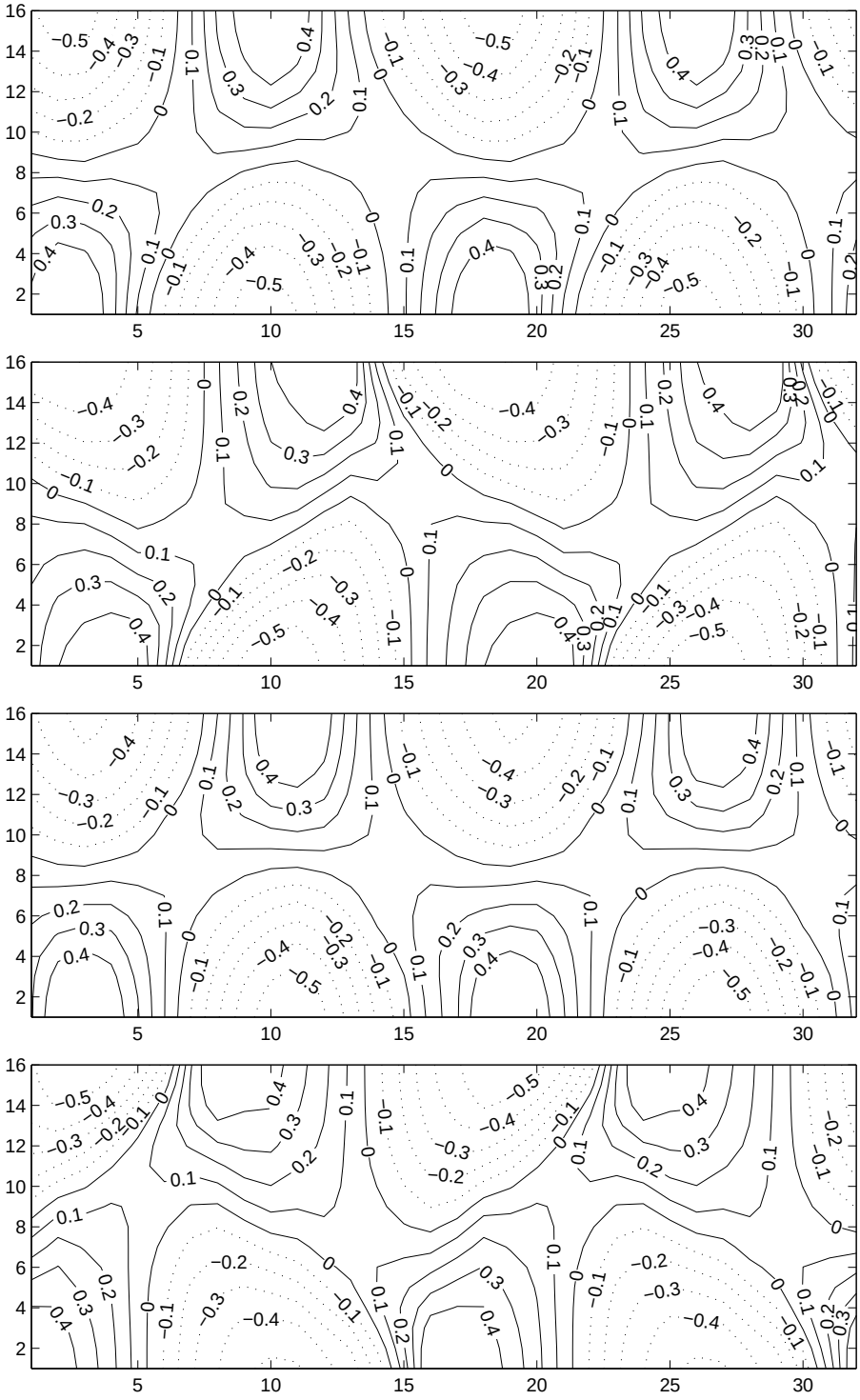

Figure 6.17: Time sequence of bed topography during the tidal cycle, under bed load dominated condition. $\theta_0 = 0.1$, $\beta = 13$, $R_p = 11000$, $D_s = 10^{-2}$

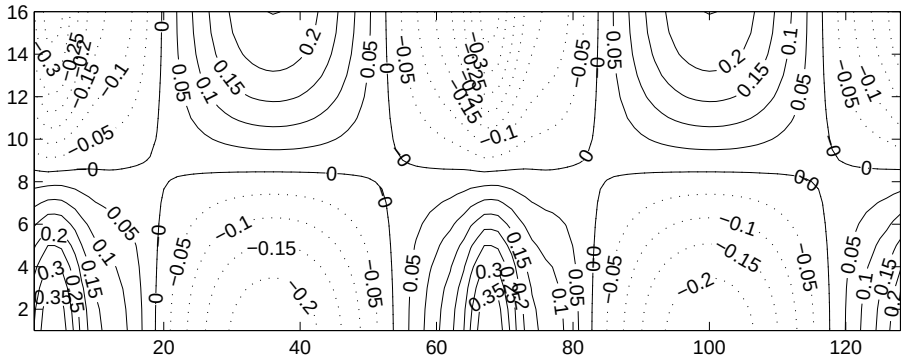

Figure 6.18: The bed topography under suspended load dominated condition. $\theta = 2$, $D_s = 10^{-5}$, $R_p = 4$, $\beta = 13$.

sand bars are stable even at spring-neap tidal frequency. Furthermore, long-term asymmetry of bedforms can only be produced and maintained when tidal currents are asymmetric, with a tidal phase dominating over the other (Harris and Collins, 1985).

Numerical results clearly suggest that the development of bed topography is related to the growth of the bed forms close to the peak values of flood and ebb phase. Hence, present results do not seem to support the hypothesis introduced in the analytical solution of Schuttelaars and de Swart (1999) where bed evolution is assumed to depend only on the net sediment transport averaged over a tidal cycle.

In figure 6.20 the time behaviour of the amplitude of different longitudinal bar modes is reported at the onset of bar development (notice that the longitudinal length decreases with the integer k). As shown in figure 6.19 mode amplification exhibits an oscillating behaviour, whose amplitude depends strongly on the longitudinal scale of the mode. In particular shorter wavelengths (green and blue solid lines in the figure), whose tidally averaged growth rate is smaller, may undergo an instantaneously faster growth which is then followed by a severe damping, while longer wavelengths (black and red solid lines in figure), which fall within the most unstable range, exhibit a more regular evolution.

The overall process of bar formation doesn't seem to differ much with respect to the fluvial case; also in this case the emergence of bar structure may occur for values of the aspect ratio β which are relatively close to the critical value β_c. The main distinctive feature of the tidal case is the vanishing value of tidal averaged celerity, at least under the forcing effect of a symmetrical tide considered herein. Non vanishing values of bar celerity could be associated with tidal asymmetries; however, these effects are not likely to produce large values of migration speed like those observed in gravel bed experiments in straight flumes.

The above result suggests that the interaction between free and forced responses may be dif-

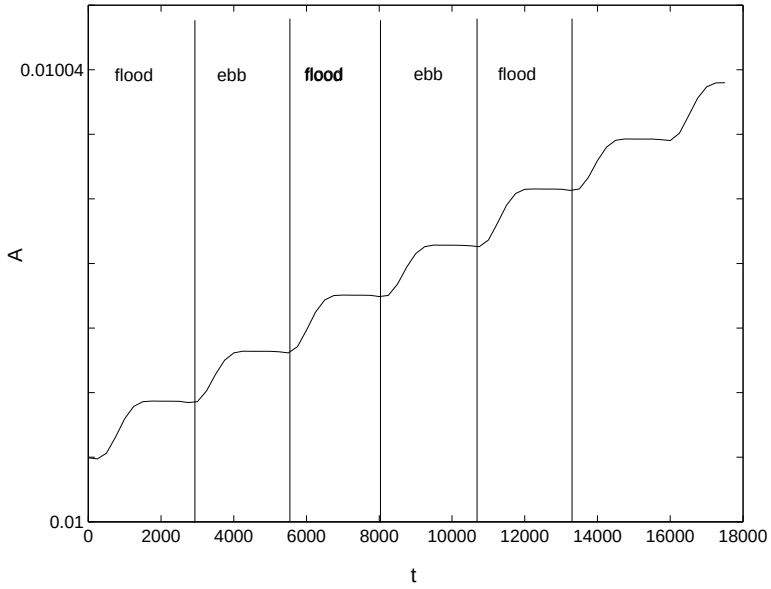

Figure 6.19: The time development of the Fourier component A_{11} of the bed profile for $\theta = 2$, $D_s = 10^{-5}$, $R_p = 4$, $\beta = 15$.

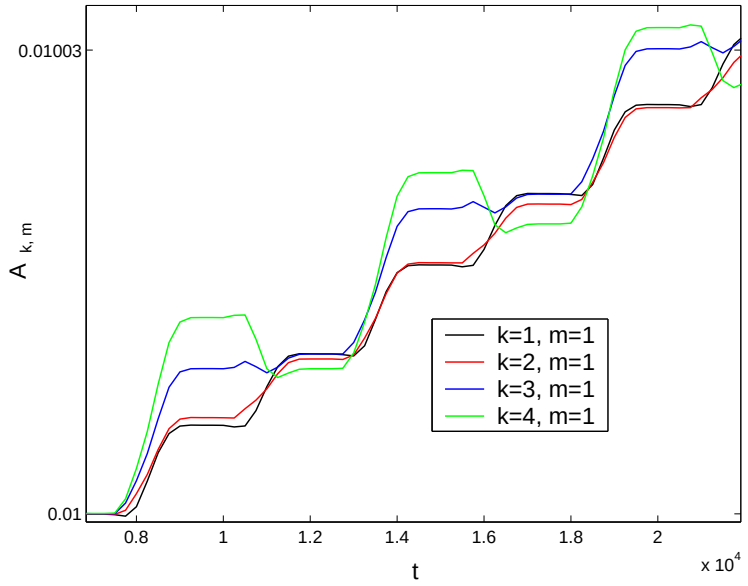

Figure 6.20: The time development of the Fourier components $A_{11}, A_{21}, A_{31}, A_{41}$ of the bed profile for $\theta = 2$, $D_s = 10^{-5}$, $R_p = 4$, $\beta = 13$.

ferent with respect to the fluvial case, where free bars migration in the downstream direction may inhibit local bank erosion. In the tidal case the presence of quasi-steady alternate bars may provide a mechanism to produce the local erosion of the bank, with the consequent deflection of the channel axis eventually leading to a meandering configuration.

7 Vertical concentration profiles in non-uniform flows

Estuarine and coastal suspended sediment dynamics is a complex phenomenon, whereby sediments undergo a sequence of processes such as erosion, deposition, advective and diffusive transport. Suspended sediment motion is inherently a three- dimensional process, though most of the estuarine and coastal models are two-dimensional: hence, they consider only the horizontal directions and imply the solution of the depth-integrated sediment transport equation (see for example Galappatti and Vreugdenhil, 1985). Two dimensional models are simpler and require much less computational effort with respect to a 3D formulation. However, within the context of a 2D approach, only the averaged (or depth integrated) sediment concentration is known; hence, the value of the concentration close to the bed, or the upward flux, which is required for the evaluation of the sediment erosion or deposition rate, must be related to the averaged concentration. When a 2D approach is used, the ratio between the mean concentration and the value at the bed is typically assumed to be equal to the corresponding ratio for an equilibrium concentration profile. Implicit in this procedure is the assumption that vertical concentration profiles can adjust instantaneously to changing flow conditions; therefore, the model can be safely applied only to situations in which the differences between the local concentration profile and the equilibrium profile, computed in terms of the local hydrodynamic conditions, are conveniently small.

The vertical concentration profiles in fine sediment systems, and hence the morphological predictions with suspended load, are very sensitive to the choice of the procedure and of the reference value of concentration used to set the bed boundary condition, as pointed out by van Rijn (1984). Under uniform conditions the vertical concentration profile can be represented through the well known Rousean distribution (5.34); on the other hand, changes in the boundary conditions can modify significantly such distribution, as in the case of the transition from one equilibrium state to another due to an abrupt change of the bed boundary condition, a problem which has been investigated by Hjelmfelt and Lenau (1970) among others (see figure 7.1). Deviation of the vertical profile from the local equilibrium profile, which is defined as the Rouse distribution corresponding to the local and instantaneous hydraulic conditions, can be fairly large under non-uniform condi-

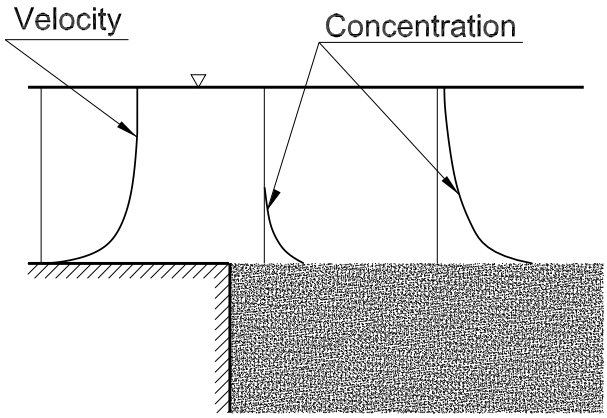

Figure 7.1: Suspension of sediments beyond an abrupt change of the bed boundary condition.

tions, since suspended load requires a relatively large adaptation length to respond to changing hydraulic conditions. The role of this adaptation process on bed stability and bedforms dynamics under suspended load dominated conditions has been highlighted in many contributions (see the original work of Engelund and Fredsoe, 1982) for small scale bedforms and the recent contributions of Tubino et al. (1999) and Seminara and Tubino (2001) for meso-scale bedforms. However, few analytical formulations are presently available to account for the effect of flow and concentration non-uniformities on the concentration profiles (see Armanini and Silvio, 1988, Galappatti and Vreugdenhil, 1985). Bolla Pittaluga and Seminara (2003a) have recently revisited the approximate solution proposed by Galappatti and Vreugdenhil (1985), which was aimed at deriving a suitable two-dimensional closure for sediment transport. Suspended sediment transport under non uniform conditions has been also analysed recently through three-dimensional numerical models, like that discussed in Chapter 5 or those proposed by Lin and Falconer (1996) and Wu et al. (2000). These models have been applied to relatively simple cases; in fact, their use is limited by the large computational time which is required for long term simulations, since the three dimensional formulation implies a quite large number of grid nodes, say $10 - 100$ times the number of grid nodes which are needed when a two dimensional model is applied to the same context. Hence, a three dimensional model can be hardly used to describe the long term morphodynamic behaviour of a river reach or an estuary, since it would require prohibitively long numerical simulations. For instance, we may note that a simulation, like those presented in Chapter 6 to investigate the development of bars in tidal channel under suspended load dominated condition, may require nearly one month of computational time on a Xeon 2 GHz processor. In the steady case numerical simulations are faster (nearly one day is required to achieve the equilibrium configuration) since a longer time step can be used.

The above limitation is the main reason why finding an analytical formulation for the vertical

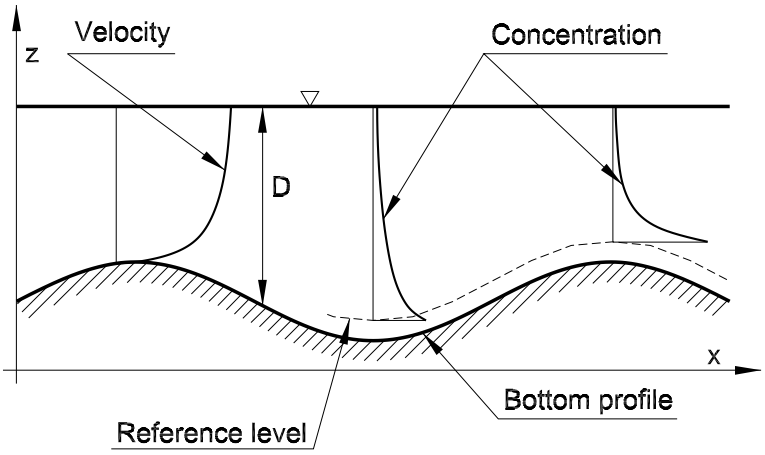

Figure 7.2: Vertical concentration and velocity profiles.

concentration profile, to be included within two-dimensional morphological models, would be highly desirable. However, in order to achieve a reasonable accuracy in the prediction of the local morphological response of fluvial and tidal systems, the analytical solution must represent adequately the typical delay of suspended load with respect to the local bottom shear stress.

In this chapter we pursue a comparison between the analytical asymptotic solution of Bolla Pittaluga and Seminara (2003a) and the results of the present numerical model. For the sake of simplicity, the comparison is performed with reference to a plane flow, that is the model is applied to two-dimensional $x-z$ context. As a first step, we restrict our analysis to the case of spatially non-uniform flows; we then consider a steady flow over a sinusoidal bottom profile, for different values of the amplitude and wavelength.

7.1 The analytical solution of Bolla Pittaluga and Seminara (2003a)

In this contribution the Authors consider a channel with a varying bottom level and subject to steady or unsteady boundary conditions. The problem is formulated in terms of the longitudinal and vertical coordinates, x^* and z^*, respectively (the asterisk as superscript denotes dimensional quantities). The lateral structure of the bed, as well as that of the flow, is taken to be horizontal; however, the same approach could be potentially extended to the case of three dimensional flows. The following scaling is used:

$$x = \frac{x^*}{L_0^*} \tag{7.1a}$$

$$(z,\eta,h,D) = \frac{(z^*,\eta^*,h^*,D^*)}{D_0^*} \tag{7.1b}$$

$$(u,w) = \frac{(u^*,w^*)}{U_0^*}, \tag{7.1c}$$

$$t = \frac{t^*}{T_0^*}, \tag{7.1d}$$

where u and w are the velocity components in the longitudinal and vertical direction, respectively, η is the bed level, h and D are the free surface elevation and flow depth, respectively. Furthermore L_0^*, D_0^* and U_0^* are suitable scales for the longitudinal coordinate, the flow depth and the flow velocity. Introducing the following dimensionless parameters

$$\alpha = \frac{D_0^*}{T_0^* U_0^* \sqrt{C_{f0}}}, \quad \omega = \frac{D_0^*}{L_0^* \sqrt{C_{f0}}}, \quad Z_0 = \frac{W_s^*}{\kappa \sqrt{C_{f0}} U_0^*}, \quad \lambda = \frac{L_0^*}{D_0^*}, \tag{7.2}$$

where κ is the Von Kàrmàn constant, C_{f0} is the reference friction coefficient and W_s^* the dimensional settling velocity of sediments, the momentum equation in longitudinal direction, flow continuity and the advection diffusion equation for the suspended sediment can be written in the following form for plane flow:

$$\alpha \frac{\partial u}{\partial t} + \omega \left(u \frac{\partial u}{\partial x} + \lambda w \frac{\partial u}{\partial z} \right) = -\frac{\omega}{F_0^2} \frac{\partial h}{\partial x} + \frac{\partial}{\partial z} \left(\nu_z \frac{\partial u}{\partial z}, \right) \tag{7.3}$$

$$\frac{\partial u}{\partial x} + \lambda \frac{\partial w}{\partial z} = 0, \tag{7.4}$$

$$\alpha \frac{\partial C}{\partial t} + \omega \left(\frac{\partial uC}{\partial x} + \lambda \frac{\partial wC}{\partial z} \right) - \kappa Z_0 \frac{\partial C}{\partial z} = \frac{\partial}{\partial z} \left(\Psi_T \frac{\partial C}{\partial z}. \right) \tag{7.5}$$

The boundary conditions associated with equations (7.3), (7.4) and (7.5) are those discussed in section 4.1: the no slip condition for the velocity at the bed, the dynamic condition of vanishing shear stress and the kinematic condition at the free surface, the condition of vanishing sediment flux at the free surface and the gradient boundary condition for sediment concentration at the bed.

Following the approach introduced by Bolla Pittaluga and Seminara (2003a), it is possible to provide analytical solutions of the vertical concentration profiles under the assumption of slowly varying conditions. In fact, as discussed by the Authors, the dimensionless parameters α and ω appearing in the differential equation (7.3) are fairly small when the flow and the concentration field display a slow variability both in time and in space, which implies that both T_0 and L_0 are fairly large. Such conditions are typically encountered in tidal flows and flood waves. A formal perturbation solution of the differential problem, made of equation (7.5) along with the boundary conditions, can be obtained by expanding the concentration C in powers of the small parameter δ

in the following form:

$$C = C_0 + \delta C_1 + O(\delta^2) \tag{7.6}$$

where

$$\delta = \frac{U_0^* D_0^*}{w_s^* L_0^*} = \frac{\omega}{\kappa Z} \tag{7.7}$$

and Z denotes the local Rouse number.

Substituting the latter expansion into the differential equation (7.5) and equating likewise powers of δ, a sequence of differential problems at the various orders of approximation in the small parameter δ is found.

At the leading order of approximation the solution (5.34) is found, which corresponds to the classical Rouse type concentration profile:

$$C_0 = C_e\left(\theta', D_s, R_p, a\right) f\left(\xi, Z, a\right) \tag{7.8}$$

written in term of the boundary fitted vertical coordinate $\xi = \frac{z-\eta}{D}$. The function $f\left(\xi, Z, a\right)$ depends only on the closure relationship employed for the eddy diffusivity Ψ_T; in particular, when the closure proposed by McTigue (1981) (4.9) is used, the function f takes the form (5.35). Equation (5.34) can also be expressed in terms of the depth averaged concentration $\overline{C}_0$ in the following form:

$$C_0 = \overline{C}_0(x,t)\phi_0(\xi, Z, a), \tag{7.9}$$

where

$$\phi_0(\xi, Z, a) = \frac{f(\xi, Z, a)}{I(Z, a)}, \tag{7.10a}$$

$$I(Z, a) = \frac{1}{(1-a)} \int_a^1 f(\xi, Z, a) d\xi. \tag{7.10b}$$

At the next order of approximation, the leading contribution of the spatial non-uniformity of the flow field on the vertical concentration profile is obtained. Recalling that:

$$\frac{\partial C_0}{\partial x} = \phi_0(\xi) \frac{\partial \overline{C}_0}{\partial x} + \overline{C}_0 \frac{\partial \phi_0}{\partial x}. \tag{7.11}$$

the solution for C_1 can then be written in the form:

$$C_1 = D\left(\frac{\partial \overline{C}_0}{\partial x} C_{11} + \overline{C}_0 C_{12},\right) \tag{7.12}$$

where the functions C_{1j} $(j = 1,2)$ are the solutions of the following boundary value problems:

$$\frac{1}{kZ_0D}\left[\frac{d}{d\xi}\left(\Psi_T\frac{dC_{1j}}{d\xi}\right)\right]+\frac{dC_{1j}}{d\xi}=p_j(\xi)\ , \tag{7.13}$$

$$\frac{\Psi_T}{kZ_0D}\frac{dC_{1j}}{d\xi}+C_{1j}=0 \qquad (\xi=1)\ , \tag{7.14}$$

$$\frac{dC_{1j}}{d\xi}=0 \qquad (\xi=a)\ , \tag{7.15}$$

where

$$p_1=u\,\phi_0\ , \qquad p_2=u\,\frac{\partial\phi_0}{\partial x}. \tag{7.16}$$

The slowly varying character of the flow field allows one to introduce a self similar logarithmic structure for the velocity u to compute the forcing terms p_1 and p_2 appearing in (7.16). It is worth noticing that in the original formulation of Bolla Pittaluga and Seminara (2003a) the term proportional to $\phi_{0,x}$ in equation (7.12) is neglected, though this approximation is not formally justified within the framework of the perturbation scheme adopted by the Authors. However, as pointed out before, the neglected effect doesn't seem to contribute significantly to the approximate solution.

7.2 Results

As a first step of present analysis a comparison is pursued between numerical and analytical solutions under steady flow conditions, for the case of an imposed bed profile which changes in the longitudinal directional according to the following sinusoidal form:

$$\eta^*=\eta_0^*\sin\left(2\pi\frac{x^*}{L_b^*}.\right) \tag{7.17}$$

Simulations are performed with values of the wavelength L_b^* ranging between $2500m$ and $10000m$ and values of the mean flow depth ranging between $5m$ and $15m$. Notice that in this case the length scale L_0^*, defined in (7.1a), is fixed and coincides with the wavelength L_b^*. In the numerical solution periodic boundary conditions are imposed for the flow field and for the concentration field, at the upstream and downstream ends of the longitudinal domain. The comparison between the results of the two models is performed according to the following procedure: the depth-integrated solution for the concentration is computed through the numerical model; then, the solution is supplemented to the asymptotic model for the evaluation of $\overline{C_0}_{,x}$, $\overline{C_0}$, D and $\phi_{0,x}$; finally, the analytical solution is determined.

A comparison between the results of the numerical and analytical solution at different cross

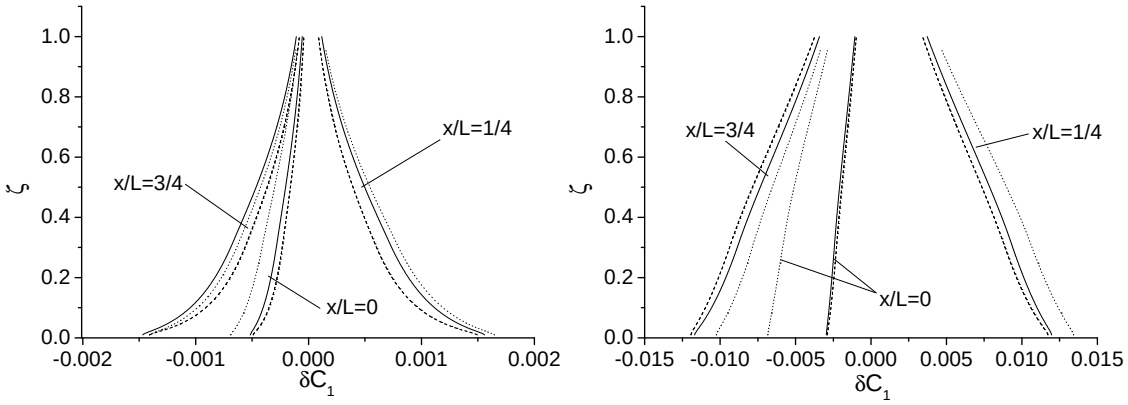

Figure 7.3: Vertical profiles of the perturbation δC_1 at different cross sections: $L_b^* = 10km$, $\eta_0^* = 0.5m$, $D_0^* = 5m$ and $R_p = 10$, $\delta = 0.023$ (left), $R_p = 4$, $\delta = 0.042$ (right). Dotted line: numerical solution; continuous line: analytical solution; dashed line: analytical solution assuming $\phi_{0,x} = 0$.

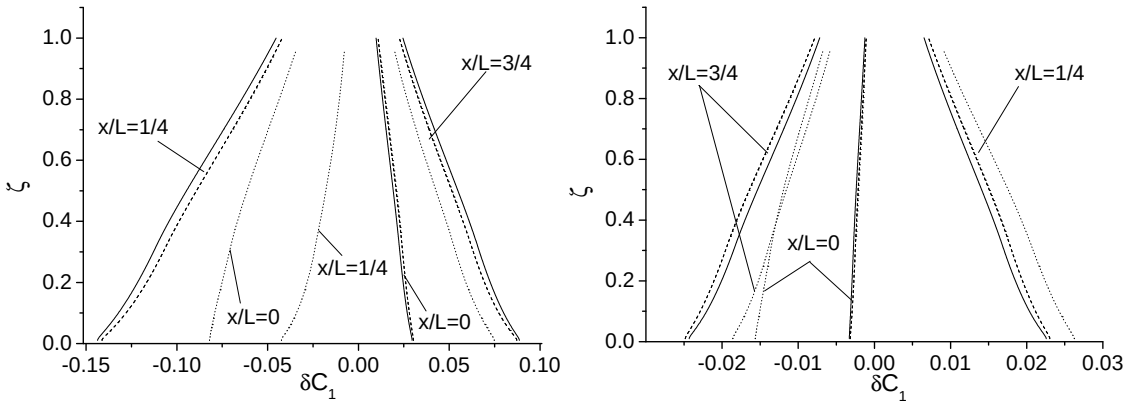

Figure 7.4: Vertical profiles of the perturbation δC_1 at different cross sections: $L_b^* = 2.5km$, $\eta_0^* = 1.5m$, $D_0^* = 10m$, $R_p = 4$, $\delta = 0.37$ (left); $L_b^* = 5km$, $\eta_0^* = 0.5m$, $D_0^* = 5m$, $R_p = 4$, $\delta = 0.085$ (right). Dotted line: numerical solution; solid line: analytical solution; dashed line: analytical solution assuming $\phi_{0,x} = 0$.

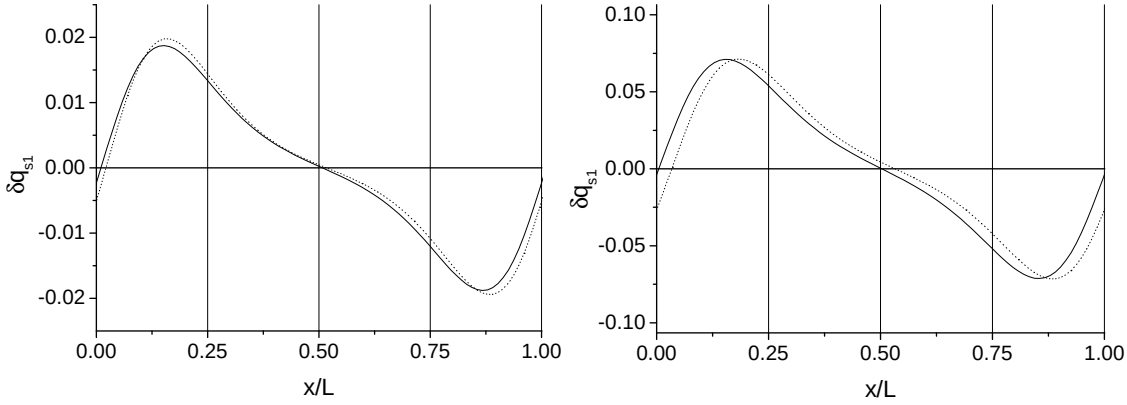

Figure 7.5: Longitudinal profiles of the perturbation δq_{s1}: $L_b^* = 10km$, $\eta_0^* = 0.5m$, $D_0^* = 5m$ $R_p = 10$, $\delta = 0.023$ (left), $R_p = 4$, $\delta = 0.042$ (right). Dotted line: numerical solution; continuous line: analytical solution.

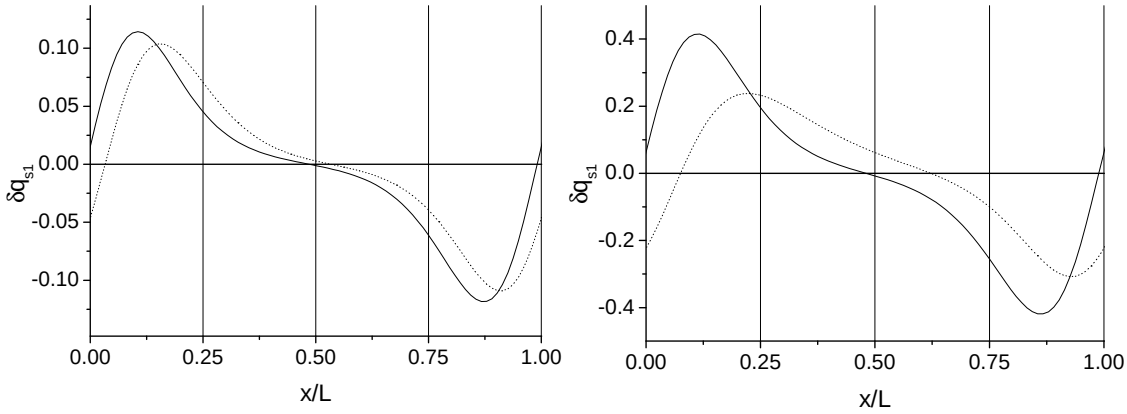

Figure 7.6: Longitudinal profiles of the perturbation δq_{s1}: $L_b^* = 5km$, $\eta_0^* = 1.5m$, $D_0^* = 10m$; $R_p = 10$, $\delta = 0.10$ (left), $R_p = 4$, $\delta = 0.19$ (right). Dotted line: numerical solution; continuous line: analytical solution.

sections in the longitudinal direction, is reported in figures 7.3 and 7.4, for different values of the parameter δ and of the amplitude η_0^* of the sinusoidal bed profile. It is worth noticing that the perturbation approach is able to reproduce at least qualitatively the vertical structure of the correction of the concentration profile, with respect to the equilibrium profile, and tends smoothly to the numerical solution as δ vanishes. However, the response of the analytical model, to the effect of variable flow conditions, seems somewhat exaggerated in that the analytical solution displays a much faster adaptation to the local conditions with respect to the numerical model.

A further comparison is made in terms of the deviation δq_{s1} of the suspended sediment transport from the value q_{s0}, which would be attained at equilibrium with the local hydrodynamic conditions. For the numerical model the value of δq_{s1} is directly computed by subtracting the

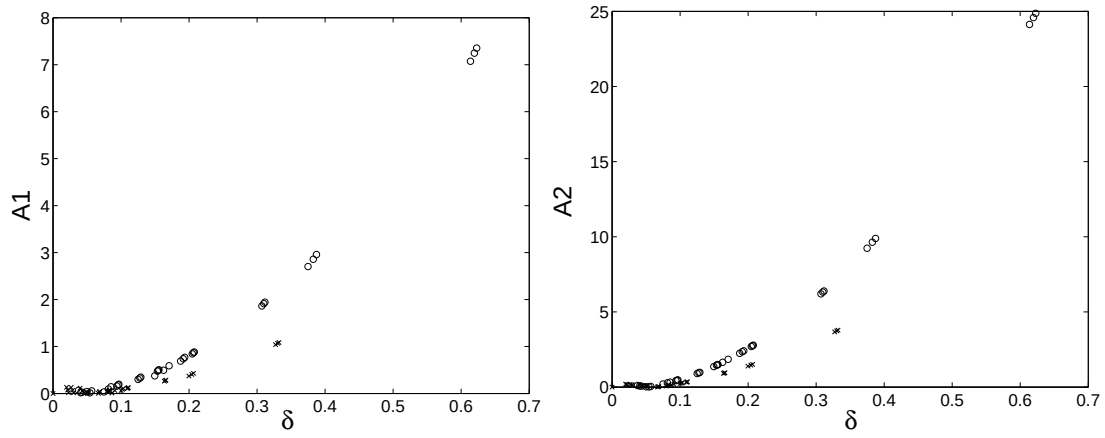

Figure 7.7: Difference between the numerically and the analytically evaluated amplitude of the first (left) and second (right) mode of the Fourier spectrum, as a function of δ. Dots $R_p = 4$ and crosses $R_p = 10$.

equilibrium solution from the numerical solution; for the approximate solution we can write:

$$q_{s1} = D \int_a^1 C_1 u \, \mathrm{d}\zeta \tag{7.18}$$

Analytical and numerical results are fairly close for small values of δ (see figure 7.2), while for larger values differences may become significant (figure 7.2).

In figures 7.2 and 7.2 is given a closer comparison between numerical and analytical solutions, in terms of the difference between numerically and analytically evaluated amplitude and phase lag of the leading components of Fourier analysis of q_{s1}. Results are plotted as functions of δ (note that the fundamental first mode has the same wavelength of the imposed bed profile L_b). It appears that the analytical model overestimates the amplitude of the perturbation of suspended load transport by an amount which increases with δ; however, for relatively small values of δ, say smaller than 0.1, the analytical model reproduces quite well the numerical solution. Furthermore, the phase lag Φ between the two solutions grows rapidly with δ.

One may argue that the differences between the two solutions could also be due to the assumption of a logarithmic structure for the velocity profile introduced in the analytical solution. However, according to the results of the numerical model, the deviations from the logarithmic velocity profile are negligible in the slowly varying context analysed herein.

The results of comparisons discussed above suggest the suitability of the analytical model of Bolla Pittaluga and Seminara (2003a) at least for relatively small values of δ. The definition of the range of applicability of the model is important in order to incorporate the procedure in a depth averaged model to evaluate the suspended sediment flux. For instance, rather than using a

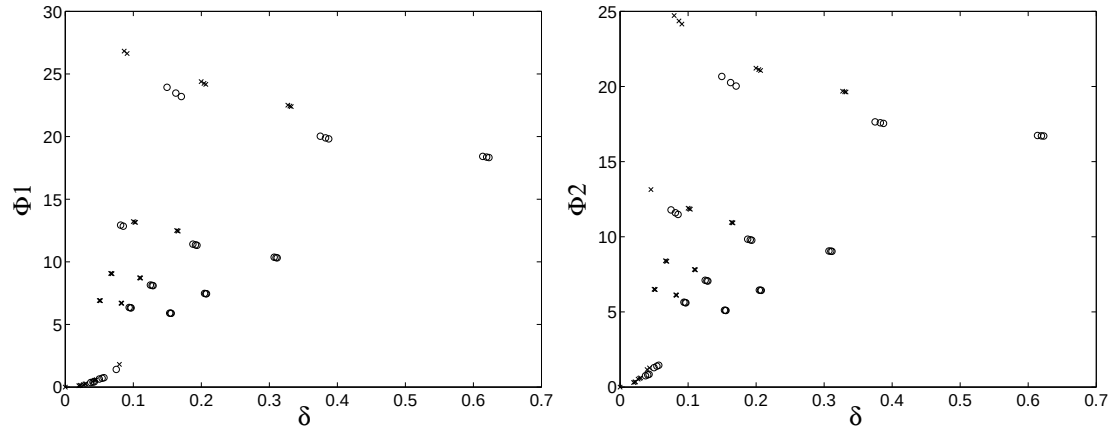

Figure 7.8: Difference between the numerically and the analytically evaluated phase lag of the first (left) and second (right) mode of the Fourier spectrum, as a function of δ. Dots $R_p = 4$ and crosses $R_p = 10$.

more complex three dimensional approach, the analytical model could be employed to investigate whether the presence of suspended load has any effect on the nature of bar instability. This challenging investigation has recently been renewed by Federici and Seminara (2003a) in the case of bed load only. In Federici and Seminara (2003b) the analysis have been extended to the case of suspended load; however, in order to have small values of δ, the analysis is made assuming a fairly large value of particle diameter, which implies a large W_s. According to the results reported in figure 6.16, suspended load is not dominant with such large values of R_p; furthermore, the standard closure relationships which are adopted to compute the suspended load (e.g., van Rijn (1984)) are not valid within this range.

It is worth noticing that when the wavelength is relatively short, the sediment is fine (as it is typical of suspension dominated environments) or the flow depth becomes large, the analytical model may introduce a fairly large approximation. We note also that the bed configuration can be influenced by several factors, like a meandering pattern or the presence of regulation works, which can introduce even smaller length-scales than those considered herein.

The case of unsteady flows, like those occurring in estuaries and tidal channels, could also be tackled with a similar analytical approach. However, the definition of the basic flow and the identification of the factors to take into account in the perturbation solution pose additional difficulties. Moreover, while the definition of the time scale T_0^* is straightforward, since it coincides with the tidal period, the definition of the length scale L_0^* is not obvious, since it depends on the hydrodynamic behaviour of the tidal channel, as discussed in Chapter 2. Notice, however, that according to Bolla Pittaluga and Seminara (2003b) the morphodynamics of tidal channels seems to be only slightly affected by non-equilibrium effects. The analysis of the range of applicability

of the analytical model in tidal flows is still a matter of investigation.

Bibliography

J. Allen. *Current Ripples: Their Relation to Pattern af Water and Sediment Motion*. North-Holland Publ. Co., Amsterdam, 1968.

J. Allen. *Sedimentary Structures - Their Characteristics and Phyical Basis*, volume 1. 593 pp. Developments in Sedimentology, Vol.30A. Elsevier, New York, 1982.

J. R. L. Allen and K. Pye. Preface. In *J. R. L. Allen and K. Pye, Saltmarshes: Morphodynamics, Conservation and Engineering ignificance*, pages vii–viii. Cambridge University Press, 1992.

A. Armanini and G. D. Silvio. A one-dimensional model for the transport of a sediment mixture in non-equilibrium confition. *Journal of Hydraulic Research*, 26:275–292, 1988.

J. Barwis. Sedimentology of some South Carolina tidal-creek point bars, and a comparison with their fluvial counterparts. In *A.D. Miller, Fluvial Sedimentology*, pages 129–160. Can. Soc. Petrol. Geol. Mem., 1978.

P. Blondeaux and G. Seminara. A unified bar-bend theory of river meanders. *J. Fluid Mech.*, 127: 449–470, 1985.

M. Bolla Pittaluga. *Long term morphodynamic equilibrium of tidal channels*. PhD thesis, University of Genoa, December 2002.

M. Bolla Pittaluga and G. Seminara. Depth integrated modelling of suspended sediment transport. *Water Resources Research*, 39(5):ESG 1, 2003a.

M. Bolla Pittaluga and G. Seminara. Long term morphodynamic equilibrium of tidal channels. the role of settling lag, overtides and sediment supply. *Water Resources Research*, submitted 2003b.

M. Bolla Pittaluga, N. Tambroni, C. Zucca, L. Solari, and G. Seminara. Long term morphodynamic equilibrium of tidal channels: preliminary laboratory observations. In *Proceedings of 2nd RCEM Symposium*, pages 423–432, Obihiro (Japan), 10-14 September 2001.

V. Casulli and E. Cattani. Stability, accuracy and efficiency of a semi-implicit method for three-dimensional shallow flow. *Computers and Mathematics with Applications*, 27(1):99–112, 1994.

V. Casulli and D. Greenspan. *Numerical Analysis for Appl. Mathematics, Science and Engineering*. Addison-Wesley, 1988.

H. Chang, D. B. Simons, and D. A. Woolhiser. Flume experiments on alternate bars formation. *J. Waterways, Harbours, Coastal Eng. Div. ASCE*, 97(1):155–165, 1971.

M. Colombini and M. Tubino. Finite-amplitude free bars: a fully nonlinear spectral solution. In *Sand Transport in Rivers, Estuaries and the Sea*, pages 163–169. R. Soulsby and R. Bettes eds. Balkema, 1991.

M. Colombini, G. Seminara, and M. Tubino. Finite-amplitude alternate bars. *J. Fluid Mech.*, 127: 213–232, 1987.

R. Dalrymple, R. Knight, and J. Lambiase. Bedforms and their hydraulics stability relationships in a tidal environment, Bay of Fundy, Canada. *Nature*, 275:100–104, 1978.

R. Dalrymple, R. Knight, B. Zaitlin, and G. Middleton. Dynamics and facies model of a macrotidal sand-bar complex, Cobequid Bay-Salmon River estuary (Bay of Fundy). *Sedimentology*, 37: 577–612, 1990.

R. W. Dalrymple and R. M. Rhodes. Estuarine dunes and bars. In *G.M.E. Perillo (ed.): Geomorphology and Sedimentology of Estuaries, Development in Sedimentology, 53*, pages 359–422. Elsevier Science, Amsterdam, 1995.

H. J. de Vriend, J. Dronkers, M. J. F. Stive, A. V. Dongeren, and Z. B. Wang. Coastal inlets and tidal basins (partly in dutch). Technical report, TU Delft, January 2000.

R. B. Dean. *Aero Rep.*, volume 74-11. Imperial College, London, 1974.

J. Dronkers. *Tidal Computations in Rivers and Coastal Waters*. North-Holland, New York, 1964.

F. Engelund and J. Fredsoe. Sediment ripples and dunes. *Ann. Rev. Fluid Mech*, 14:13–37, 1982.

B. Federici and G. Seminara. On the convective nature of bar instability. *J. Fluid Mech.*, 99(1): 99, 2003a.

B. Federici and G. Seminara. On the convective nature of bar instability: the effect of suspended load. In *Proceedings of 3rd RCEM Symposium*, pages 136–147. Barcelona (Spain), 1-3 September 2003b.

J. Fredsoe. Meandering and braiding of rivers. *J. Fluid Mech.*, 74:609–624, 1978.

C. T. Friedrichs and D. G. Aubrey. Tidal propagation in strongly convergent channels. *J. Geophys. Res.*, 99:3321–3336, 1994.

C. T. Friedrichs, B. D. Armbrust, and H. E. de Swart. Hydrodynamics and equilibrium sediment dynamics of shallow, funnel-shaped tidal estuaries. In *Physics of Estuaries and Coastal Seas, Balkema, Rotterdam*, pages 315–327. Dronkers and Scheffers (eds.), 1998.

Y. Fujita. Bar and channel formation in braided streams. In *River Meandering*, pages 417–46. S. Ikeda and G. Parker eds. AGU Water Res. Monograph, 1989.

Y. Fujita and Y. Muramoto. Studies on the process of development of alternate bars. Technical report, D. P. R. I. Bull., Kyoto Univ., Part3, No. 314, 55-86 1985.

R. Galappatti and C. B. Vreugdenhil. A depth-integrated model for suspended sediment transport. *J. Hydr. Eng., ASCE*, 23(4):359–377, 1985.

M. Garcia and Y. Niño. Dynamics of sediment bars in straight and meandering channels: experiments on the resonance phenomenon. *J. of Hydraulic Res.*, 31(6):739–761, 1993.

P. Garcia-Navarro, F. Alcrudo, and J. Saviron. 1D open-channels flow simulation using TVD-MacCormak scheme. *J. Hydr. Eng. ASCE*, 118(10):1359–1372, 1992.

G. Green. On the motion of waves in a variable canal of small depth width. *Trans. Cambridge Philos. Soc.*, 6(457-), 1837.

P. Harris and M. Collins. Bedform distribution and sediment tranport paths in the Bristol Channel and Severn Estuary. *U.K. Mar. Geol.*, 62:153–166, 1985.

P. T. Harris, E. K. Baker, A. R. Cole, and S. A. Short. A preliminary study of sedimentation in the tidally dominated Fly River Delta, Gulf of Papua. *Cont. Shelf Res.*, 13:44–472, 1993.

A. Hibma, H. J. de Vriend, and M. J. F. Stive. Channel and shoal formation in estuaries. In *Proceedings of 2nd RCEM Symposium*, pages 463–471. Obihiro (Japan), 10-14 September 2001.

A. Hibma, H. Schuttelaars, and H. de Vriend. Initial formation and evolution of channels-shoals patterns in estuaries. In *Proceedings of 3rd RCEM Symposium*, pages 749–760. Barcelona (Spain), 1-3 September 2003.

A. T. Hjelmfelt and C. W. Lenau. Non-equilibrium transport of suspended sediment. *J. Hydr. Div., ASCE*, 96(HY7):1567–1586, 1970.

S. Ikeda. Prediction of alternate bar wavelength and height. Technical report, Rep. Dept. Found. Eng. and Const. Eng., Saitama Univ., Vol. 12, 23-45 1982a.

S. Ikeda. Lateral bedload transport on side slopes. *J. Hydraulic Div., ASCE,* 108(99):1369–1373, 1982b.

S. Ikeda and T. Nishimura. Bed topography in bends of sand-silt rivers. *J. Hydraulic Div. ASCE,* 108(11):1397–1411, 1985.

S. Ikeda, G. Parker, and K. Sawai. Bend theory of river meanders. Part 1. Linear development. *J. Fluid Mech.*, 112(363-3), 1981.

M. Jaeggi. Formation and effects of alternate bars. *J. Hydraulic Div. ASCE,* 111(11):1103–1122, 1984.

D. A. Jay. Green's law revisited: Tidal long-wave propagation in channels with strong topography. *J. Geophys. Res.*, 96(C11):20585–20598, November 15 1991.

R. Kinoshita. Investigation of channel deformation in Ishikari River. Technical report, Rep. Bureau of Resources, Dept. Science and Technology, Japan, 1961.

R. Kinoshita and H. Miwa. River channel formation which prevents downstream translation of transverse bars. *Shinshabo (in japanese)*, 94(1):12–17, 1974.

R. Knight. Linear sand bar development and tidal current flow in Cobequid Bay, Bay of Fundy, Nova Scotia. In *The Coastline of Canada. Geol. Surv. Can. Pap.*, pages 80–10: 123–152. S.B. McCan, 1980.

A. Kovacs and G. Parker. A new vectorial bedload formulation and its application to the time evolution of straight river channels. *Journal of Fluid Mechanics*, 127:153–183, 1994.

S. Lanzoni. Experiments on bar formation in a straight flume. 1. Uniform sediment. *Water Resources Research*, 36(11):3337–3349, November 2000.

S. Lanzoni and G. Seminara. Long term evolution and morphodynamic equilibrium of tidal channels. *J. Geophys. Res.*, 107:1–13, 2002.

S. Lanzoni and G. Seminara. On tide propagation in convergent estuaries. *J. Geophys. Res.*, 103 (C13):30793–30812, 15 December 1998.

R. L. Leveque. High resolution conservative algorithms for advection in incompressible flow. *J. of Num. Analysis*, 33(1):627–665, 1996.

B. Lin and R. A. Falconer. Numerical modelling of three-dimensional suspended sediment for estuarine and coastal waters. *J. of Hydraulic Res.*, 34(4):435–456, 1996.

H. Lorenz. Het in rekening brengen vanden weerstand bij schommelende vloeistofbewegingen. *De ingenieur*, page 695, 1922.

R. MacCormack. The effect of viscosity in hypervelocity impact cratering. *AIAA Paper*, pages 69–384, 1969.

D. F. McTigue. Mixture theory for suspended sediment transport. *J. Hydr. Div. ASCE*, 107(HY6): 659–673, 1981.

J. Murray and A. Hawkins. Sediment transport in the Severn Estuary during the past 8000-9000 years. *J. Geol. Soc. London*, 132:385–398, 1977.

C. Nordin. *Statistical properties of dunes profiles*. U.S.G.S. Prof.Pap. 562-F, 1971.

G. Parker. Self-formed straight rivers with equilibrium banks and mobile bed. Part 1. The sand-silt river. *J. Fluid Mech.*, 89(1):109–125, 1978.

G. M. E. Perillo. *Geomorphology and Sedimentology of Estuaries*, volume 53. Developments in Sedimentology, Elsevier, Amsterdam, 1995.

R. A. Pielke. *Mesoscale meteorological modelling*. Accademic press: San Diego, Calif, 1994.

D. Prandle. Tides in estuaries and embayments. In *Tidal hydrodynamics. John Wiley & Sons*, pages 125–151. B.B. Parker, 1991.

H. E. Reineck. Tidal flats. In *Recognition of Ancient Sedimentary Environments. SEPM Spec. Pub.*, pages 16: 146–159. J. K. Rigby and W. K. Hamblin, 1972.

R. Repetto and M. Tubino. Transition from migrating alternate bars to steady central bars in channels with variable width. In *Proceedings of 1st RCEM Symposium*, pages 605–614. Genoa (Italy), 6-10 September 1999.

A. Robinson. Ebb-flood channel systems in sandy bays and estuaries. *Geography*, 45:183–199, 1960.

D. Rubin and R. Hunter. Bedform alignment in directionally varying flows. *Science*, 237:276–278, 1987.

D. Rubin and H. Ikeda. Flume experiments on the alignment of transverse, oblique, and longitudinal dunes in directionally varying flows. *Sedimentology*, 37:673–684, 1990.

D. Rubin and D. McCulloch. Single and superimposed bedforms: a syntesis of San Francisco Bay and flume observations. *Sediment. Geol.*, 26:207–231, 1980.

R. Schielen, A. Doelman, and H. E. de Swart. On the nonlinear dynamics of free bars in straight channels. *J. Fluid Mech.*, 252(1):325–356, 1993.

H. M. Schuttelaars and H. E. de Swart. Multiple morphodynamic equilibria in tidal embayments. *J. Geophys. Res.*, 105:24105–24118, 2000.

H. M. Schuttelaars and H. E. de Swart. Initial formation of channels and shoals in a short tidal embayment. *J. Fluid Mech.*, 127:15–42, 1999.

G. Seminara. *Stability and morphodynamics*, volume 33. Meccanica, Kluviert Academic Publishers, 1998.

G. Seminara and M. Tubino. Sand bars in tidal channels. Part 1. Free bars. *J. Fluid Mech.*, 440: 49–74, 2001.

G. Seminara, S. Lanzoni, M. Bolla Pittaluga, and L. Solari. Estuarine patterns: An introduction to their morphology and mechanics. In *Geomorphological Fluid Mechanics*, pages 99–99. N.J. Balmforth and A.Provenzale, Lecture notes in Phisics, Springer Verlag, Berlin, 2001a.

G. Seminara, G. Zolezzi, M. Tubino, and D. Zardi. Downstream and upstream influence in river menadering. Part 2-Planimetric development. *J. Fluid Mech.*, 438:213–230, 2001b.

Y. Shimizu and T. Itakura. Calculation of bed variation in alluvial channel. *J. Hydraul. Eng.*, 115 (3):367–384, 1989.

L. Solari, G. Seminara, S. Lanzoni, M. Marani, and A. Rinaldo. Sand bars in tidal channels. part 2. tidal meanders. *J. Fluid. Mech.*, 451:203–238, 2002.

J. Southard and L. Boguchwal. Bed configurations in steady unidirectional water flows. Part 2. Synthesis of flume data. *J. Sediment. Petrol.*, 60:658–679, 1990.

N. Struiksma and A. Crosato. Analysis of a 2-D bed topography model for rivers. In *River Meandering*, pages 153–180. S. Ikeda and G. Parker eds. AGU Water Res. Monograph, 1989.

A. M. Talmon, N. Struiksma, and M. C. L. M. van Mierlo. Laboratory measurements of the direction of sediment transport on transverse alluvial-bed slopes. *J. of Hydraulic Res.*, 33(4): 495–517, 1995.

M. Toffolon. *Hydrodynamic and morphodynamics of tidal ystems*. PhD thesis, University of Trento, December 2002.

M. Tubino and G. Seminara. Free-forced interactions in developing meanders and suppression of free bars. *J. of Fluid Mech.*, 127:131–159, 1990.

M. Tubino, R. Repetto, and G. Zolezzi. Free bars in rivers. *J. Hydraulic Res.*, 37(6):759–776, 1999.

J. van Den Berg. Bedform migration and bed-load transport in some rivers and tidal environments. *Sedimentology*, 34:681–698, 1987.

L. C. Van Rijn. Mathematical models for sediment concentration profiles in steady flow. *Euromech*, 192(1):49–68, 1985.

L. C. van Rijn. Sediment Transport. Part II: Suspended Load Transport. *Journal of Hydraulic Engineering, ASCE*, 110(11):1613–1641, November 1984.

Y. Watanabe and M. Tubino. *Influence of Bed Load and Suspended Load on Alternate Bar*, volume 36. Proceedings of Hydraulics Engineering, JSCE, 1992.

P. J. Whiting and W. E. Dietrich. Experimental constraints on bar migration through bends: Implications fo meander wavelength selection. *Water Resources Research*, 29(4):1091–1102, 1993.

L. Wright, J. Coleman, and B. Thom. Processes of channel development in a high-tide-range environment: Cambridge Gulf-Ord River delta, Western Autralia. *J. Geol.*, 81:15–41, 1973.

L. Write. River Deltas. In *R.A. Davis, Jr., Coastal Sedimentary Environments(2nd ed.)*, pages 1–76. Springer-Verlag, New York, 1985.

W. Wu, W. Rodi, and T. Wenka. 3D numerical modeling of flow and sediment transport in open channels. *J. Hydraulc Eng., ASCE*, 126(1):4–15, 2000.

M. Yalin. Geometrical properties od sand waves. In *Proceedings of Am. Soc. Civil Eng.*, pages 90: 105–119, 1964.

M. Yalin. *Mechanics of Sediment Transport, 2nd edtion*. Pergamon Press, Toronto, 1977.

M. Yalin. On the formation mechanism of dunes and ripples. In *Euromech Colloq. Proc.*, page 261, 1987.